Universidade de Aveiro Departamento de Física
2009

Pedro Hugo Ferreira Natal da Luz

Desenvolvimento de detectores de neutrões baseados em microestruturas MHSP

Development of neutron and X-ray imaging detectors based on MHSP

Universidade de Aveiro Departamento de Física
2009

Pedro Hugo Ferreira Natal da Luz

Desenvolvimento de detectores de neutrões baseados em MHSP

Development of neutron and X-ray imaging detectors based on MHSP

Dissertação apresentada à Universidade de Aveiro para cumprimento dos requisitos necessários à obtenção do grau de Doutor em Física, realizada sob a orientação científica do Prof. Doutor João Filipe Calapez Albuquerque Veloso, Professor do Departamento de Física da Universidade de Aveiro e co-orientação do Prof. Doutor Joaquim Marques Ferreira dos Santos, Professor Associado com Agregação do Departamento de Física da Universidade de Coimbra.

Apoio financeiro do POCTI no âmbito do III Quadro Comunitário de Apoio.

Apoio financeiro da FCT (Bolsa de Doutoramento SFRH/BD/16342/2004) e do FSE no âmbito do III Quadro Comunitário de Apoio.

Dedico este trabalho ao meu amigo André Moutinho.
Passámos horas a falar sobre ciência.

o júri

presidente

Doutor Paulo Jorge dos Santos Gonçalves Ferreira
Reitoria da Universidade de Aveiro

Doutora Maria da Conceição Abreu e Silva
Professora Catedrática da Faculdade de Ciências e Tecnologia da Universidade do Algarve

Doutor Joaquim Marques Ferreira dos Santos
Professor Associado com Agregação da Faculdade de Ciências e Tecnologia da Universidade Coimbra

Doutor Armando José Trindade das Neves
Professor Associado da Universidade de Aveiro

Doutor Luís Filipe dos Santos Garcia Peralta
Professor Auxiliar com Agregação da Faculdade de Ciências da Universidade de Lisboa

Doutor João Filipe Calapez de Albuquerque Veloso
Professora Auxiliar da Universidade de Aveiro (Orientador)

agradecimentos

No final de quatro anos de investigação em torno das MHSPs, é tempo de reconhecer todos aqueles que de algum modo contribuíram para o sucesso do meu Doutoramento.

Gostaria de agradecer em primeiro lugar aos meus orientadores Prof. Dr. João Veloso e Prof. Dr. Joaquim Santos pelo franco auxílio e aconselhamento, sempre que foi necessário.

Aos meus colegas nos laboratórios, em Aveiro e em Coimbra. É um privilégio trabalhar com pessoas sempre prontas a ajudar e com quem se pode partilhar muito mais do que um local de trabalho.

À minha família (pais, irmão, cunhada e sobrinho) por acreditarem sempre em mim, por vezes até mais que eu!

À Vanessa pelo respeito, pelo afecto e por suportar os piores e os melhores humores.

O agradecimento mais especial vai para os que partilham comigo a minha outra paixão: a música. Mesmo quando os meus pensamentos estão algures entre detectores e tubos de raios X, e mesmo quando tive que faltar a ensaios para trabalhar, eles contaram comigo. Obrigado Sílvia, Gonçalo, Alex, Cardina, Luísa, Celso, Murta, Damasceno, Jú, Luís Pedro e a toda a gente do GEFAC! Sem vós não teria sido tão divertido!

palavras-chave

Detectores gasosos baseados em microestruturas, Micro-Hole & Strip Plate, Gas Electron Multiplier, imagiologia de raios X e de neutrões.

resumo

A Micro-Hole & Strip Plate (MHSP) é uma microestrutura desenvolvida recentemente em instituições universitárias portuguesas. Neste trabalho, o seu desempenho como detector para imagiologia é explorado, tendo como objectivo a imagiologia não só de neutrões, mas também de raios X.
A aplicação do método da divisão resistiva de carga é aplicada a uma MHSP especialmente desenhada para sensibilidade em posição. Várias abordagens em termos da electrónica de aquisição de sinal são testadas, sem perder de vista a relação desempenho-preço.
Resoluções espaciais abaixo de 1 mm foram obtidas com a MHSP a operar em xénon e tetrafluorometano, com um sistema de detecção a um preço modesto quando comparado com as alternativas, e apropriado para inúmeras aplicações em imagiologia de neutrões e de raios X.

keywords

Micropattern gaseous detectors, Micro-Hole & Strip Plate, Gas Electron Multiplier, X-ray and neutron imaging.

abstract

The Micro-Hole & Strip Plate (MHSP) is a Micropattern Gaseous Detector developed recently in Portuguese institutions. In this work, its performance as a imaging detector is characterised, aiming neutron imaging, but also with results in X-ray imaging.

The application of the method of resistive charge division is used in a MHSP specially designed for position sensitivity. Several different electronic approaches for signal collection are tested, always taking into account the performance-price ratio.

Position resolutions below 1 mm were achieved with the MHSP operating in xenon and in tetrafluoromethane, in a very cost effective detector setup, suitable for many applications in neutron and X-ray imaging.

Publicações no âmbito desta Tese de Doutoramento

Jornais internacionais com arbitragem científica

H. Natal da Luz, A. L. Gouvêa, J. A. Mir, J. M. F. dos Santos, and J. F. C. A. Veloso, "The 2D-Micro Hole & Strip Plate in CF_4 atmosphere aiming neutron imaging," *J. Inst.*, vol. P1, no. 4, 2009.

H. Natal da Luz, A. S. Conceicao, J. F. C. A. Veloso, J. M. F. dos Santos, A. C. S. S. M. Bento, J. A. Mir, and L. F. R. Ferreira, "Gem operation in high-pressure in CF_4: Studies of charge and scintillation properties," *IEEE Trans. Nucl. Sci.*, vol. 56, no. 3, pp. 1564–1567, 2009.

H. Natal da Luz, C. A. B. Oliveira, C. D. R. Azevedo, J. A. Mir, R. de Oliveira, J. M. F. dos Santos, and J. F. C. A. Veloso, "Single photon counting x-ray imaging system using a Micro Hole and Strip Plate," *IEEE Trans. Nucl. Sci.*, vol. 55, no. 4, pp. 2341–2345, 2008.

H. Natal da Luz, J. F. C. A. Veloso, J. M. F. dos Santos, and J. A. Mir, "A simple x-ray position detection system based on a MHSP," *Nucl. Instr. Meth. A*, vol. 580, pp. 1083–1086, 2007.

H. Natal da Luz, J. F. C. A. Veloso, J. M. F. dos Santos, and J. A. Mir, "MHSP operation in CF_4," *Nucl. Instr. Meth. A*, vol. 580, pp. 286–288, 2007.

H. Natal da Luz, J. F. C. A. Veloso, N. F. C. Mendes, J. M. F. dos Santos, and J. Mir, "MHSP with position detection capability," *Nucl. Instr. Meth. A*, vol. 573, pp. 191–194, 2007.

Outras publicações

H. Natal da Luz, A. S. Conceicao, J. F. C. A. Veloso, J. M. F. dos Santos, A. C. S. S. M. Bento, J. A. Mir, and L. F. R. Ferreira, "Gem operation in high-pressure in CF_4: Studies of charge and scintillation properties," in *IEEE Nuclear Science Symposium Conference Record (CD-ROM)*, (Dresden, Germany), 2008.

H. Natal da Luz, "X-ray imaging at the price of a coffee," *JiAPS - The Journal of the International Association of Physics Students*, 2009, in press.

H. Natal da Luz, C. A. B. Oliveira, C. D. R. Azevedo, J. A. Mir, J. M. F. dos Santos, and J. F. C. A. Veloso, "Single photon counting x-ray imaging system using a Micro Hole and Strip Plate," in *IEEE Nuclear Science Symposium Conference Record (CD-ROM)*, (Honolulu, USA), 2007.

H. Natal da Luz, J. M. F. dos Santos, and J. F. C. A. Veloso, "The Micro-Hole and Strip Plate as an imaging detector," in *WMISI — Workshop on Medical Instrumentation Signal and Imaging*, (Aveiro, Portugal), 2007.

H. Natal da Luz, J. F. C. A. Veloso, J. M. F. dos Santos, and J. A. Mir, "The MHSP as a simple x-ray imaging detector," in *XV Conferência Nacional de Física (Física 2006)*, (Aveiro, Portugal), 2006.

Contents

Introduction

Micropattern Gaseous Detectors (MPGD) have undergone an impressive development over the past few years. The new techniques of circuit board printing, which allow etching much finer structures in polymeric substrata have played an important role on this development. The Micro-Hole & Strip Plate (MHSP) has made its first steps in the Atomic and Nuclear Instrumentation Group in the Physics Department of the University of Coimbra (GIAN) and, later on, in the Radiation Detection and Medical Imaging Group in the Physics Department of the University of Aveiro (DRIM). It has conquered its place among the other MPGD due to its high performance in terms of reliability, gain in charge and high rate capability. The fact that it combines two different MPGD patterns within the same substrate (a Gas Electron Multiplier—GEM—and a Microstrip Plate—MSP), with two charge multiplication stages, makes it a very simple and cost effective device.

MPGD have an intrinsic imaging capability and virtually all of them have been tested as central component of position sensitive detectors in many geometries and using many methods, such as readout pads, together with delay or resistive lines, or high density electronics. The MHSP had never been used as an imaging device itself, without the use of extra components such as GEMs or readout pads. Taking into account its better performance in some aspects (the high gain in charge is one of them), a study of its capability was due, in order to accomplish one more step in its characterisation and consolidation as a state of the art MPGD.

The experiments described in this work were made aiming neutron detection. The aim was the development of a thermal neutron beam monitor for the ISIS[1] spallation source in the Rutherford Appleton Laboratory. Such a monitor is required to have a spatial resolution of 1 mm. For this, a special gas mixture of helium-3 and tetrafluoromethane must be used at suitable partial pressures as filling gas, to stop the products of the nuclear reaction needed to detect the neutrons.

Imaging neutron detectors have other applications, such as neutron diffraction in crystals and the detection of light elements such as hydrogen. Thermal neutron imaging detectors have been tested to detect plastic explosives in land mines under the ground, proving that nuclear science can be of extreme importance in humanitarian missions.

Because a neutron source is not readily available in the lab, the primary electron

[1]This facility was named after the Egyptian goddess who brought the dead back to life. The name was chosen because this neutron source used many components from previous accelerators in the United Kingdom.

clouds were made using X-rays. The use of a simple radioactive source or an X-ray tube is much more practical, providing also a better control of the conditions of the experiments. This thesis is divided in 5 chapters.

Chapter 1 is a short background review and has the aim of providing the reader not familiar with this field of research with enough information to understand the experiments done along the work. A brief summary of the most important interactions of radiation with matter is given in the first section, crucial for a correct understanding of the processes involved in particle detection. The following sections are a historical review of the long research work carried out from the invention of the Geiger-Müller detector to the Micro-Hole & Strip Plate. This review is completed with some examples of other works contributing to the development of gaseous proportional detectors.

In chapter 2, the preliminary studies with the standard MHSP (without position sensitivity) are made. Its performance in xenon is discussed. Xenon has been used for several years in the labs where this work has been carried out. The behaviour of this noble gas is well known and the results obtained could easily be compared with the abundant previous works done using other detectors. Furthermore, the tests with X-rays can also serve to test the performance of the MHSP as an X-ray imaging detector. The second section works as the hypothesis of this work, explaining the principle of imaging with the MHSP, using resistive charge division. Its subsection tests the feasibility of the principle. The third section describes some basic principles to take into account in imaging and the limitations in the spatial resolution. In the fourth section, the first tests, using 1D position detection are done. The discussion focuses aspects such as the importance of making the 1D tests and the choice of analog or digital signal processing electronics.

The first real 2D images are shown in chapter 3. A 2D detector was built and tested with xenon as the filling gas. The integral nonlinearity and the position resolution are determined and the important aspect of energy discrimination is also focused. The discussion analyses the effects of the signal-to-noise ratio and the proton range in the position resolution, as well as the influence of the nonuniformity of the resistive strips in the final image.

Chapter 4 shows the performance of the MHSP as an imaging device in tetrafluoromethane (CF_4). X-rays are still used to form the electron primary cloud, but CF_4 is a gas used in neutron detectors to stop the protons and the tritons generated in the nuclear reaction between thermal neutrons and helium-3. The first section analyses the performance of the standard MHSP in terms of gain and energy resolution and the second section shows 2D images with spatial resolution determination and its energy dependence. In the third section, a single-GEM was used in CF_4 to compare its performance with the MHSP. The discussion takes this comparison into account and focuses the aspect of the photoelectron range influencing the position resolution when using X-rays.

In the conclusion, the main achievements of this work are described and some of the many possible applications are enumerated. The future work to be done in the sequence of this work is also mentioned.

Chapter 1

Gaseous detectors for ionising radiation

Ionising radiation, as the name suggests, generates *ion/electron pairs* (from here on simply named as *ion pairs*) upon interaction with the material where it penetrates. The generation of ions is directly connected with the generation of free electrons in the absorbing material. Without going much deep into how the electrons are generated in the material—this issue will be addressed in the next section—the number of free electrons in the material, after an ionising particle has been absorbed is proportional to the particle's kinetic energy up to some statistical fluctuations. This fact is independent of the particle. The bunch of electrons generated due to the influence of one single particle, independently of the number of interactions, is called the *primary electron cloud* throughout this work. Primary electrons are, therefore, all the electrons generated solely by the energy deposited by the particle in the system[1].

If nothing further happens, the primary electrons recombine with the ions and the system reestablishes equilibrium. However, if electric fields are applied, the electrons and the ions drift in opposite directions along the electric field lines. The drift velocity is defined as the velocity vector averaged over all the particles. In the absence of an electric field, the velocity vector of each particle has a random direction. Therefore, the average or drift velocity is zero. The drift velocity of ions and electrons depends on their mobility in the medium and on their mean free path. For higher pressures, there are more particles on their way and the mean free path is shorter leading to a lower drift velocity due to a higher number of collisions. Since ions are heavy particles, their drift velocity is very low. After being generated, under the influence of an electric field, they drift towards the cathode. The drift velocity of ions is so low that for high radiation rates, the generation of ions in a given region may be higher than the drain of ions and space charge effects occur, distorting the electric field. Electrons are lighter and

[1] In some contexts, namely in X-ray detection, the primary electron is the electron removed from the atom by photoelectric effect and all the others are the secondary electrons. In this work, the electron removed from the atom is called the *photoelectron* and all the electrons produced due to the interaction of one particle (X-ray or other) are called the *primary electrons*. This will be reminded along the text whenever there may be ambiguity.

have a much higher mobility than ions. They can be very much accelerated between collisions, but their direction changes in every interaction. Their path is very sinuous. The drift velocity does not increase indefinitely with the electric field, but saturates at some point. If the electric field is increased, only the acceleration of electrons between collisions increases, but not the drift velocity.

At some point, the ionisation threshold is reached. The electric field becomes so high that the electrons, within their mean free path length, acquire high enough kinetic energy to remove electrons from the material. The electrons removed, also subject to the same electric field, are once again accelerated and remove further electrons, building a charge avalanche—the Townsend avalanche.

In gaseous detectors, except for highly energetic particles, the number of primary electrons is not enough to overcome the noise of the electronic acquisition systems, therefore, they must be multiplied, forming the Townsend avalanche. The ratio between the number of primary electrons and the number of electrons collected at the output of the detector is the *gain in charge* also known as the *multiplication factor*. The gain in charge increases with the electric field.

In proportional counters, the charge collected is kept proportional to the energy of the incident particle. This suggests that for a certain energy, the primary electron cloud has always the same number of electrons. However, there are statistical fluctuations in the ionisation process in the gas. The ionisation process follows a Poisson statistical model, which means that the variance σ^2 is equal to the average number of primary electrons $\overline{N}$ up to a factor F—the Fano factor—which takes into account the fact that not all the interactions are independent:

$$\sigma^2 = F \cdot \overline{N}.$$

Because of this, the histogram of the energy distribution of an ideal mono-energetic beam of particles is not a delta function, but a Gaussian probability distribution around a mean value, with a full width at half maximum (FWHM) correspondent to the best possible *energy resolution* of the detector. The energy resolution is usually worse than this limit, because the contribution of all the sources of fluctuation (for example, the electronic noise) must be considered.

The time a detector needs to generate the charge pulse is also an important factor. If two particles enter the detector in a very short time, the ability of the detector to distinguish the two primary clouds as different events is determined by the time of each charge pulse. The time of one pulse is directly related to the time it takes for all the electrons of the Townsend avalanche to be collected as well as all the positive ions formed in the process. Due to the small velocity of ions, the length they must travel before they are collected has a great influence in the pulse rise time. If the time interval between the arrival of the first electron and the last ion is around 1 µs, a counting rate of 1 MHz is possible.

1.1 Interaction of radiation with matter

The first aspect to be taken into account when designing an ionising radiation detector is the kind of particles to detect. In this work, the concept of neutron imaging is exploited. However, the tests were made using X-rays. Taking into account all the particles involved in both X-ray and neutron detection, the understanding of how photons, electrons, heavy charged particles or neutrons interact with matter is crucial. The interaction of radiation with matter is a complex subject and cannot be fully addressed in this thesis. This section is not intended to be a profound description of all the interactions, but to provide the reader with the very basics about the most important effects taken into account when developing the detector prototypes described along this work.

1.1.1 X-rays

X-rays were first characterised in 1895, by Wilhelm Röntgen [1]. Their main interaction with matter are through the photoelectric effect, first understood by Einstein [2]. When an X-ray photon hits an electron in a shell of an atom, its energy is totally transferred to the electron as it is removed. One part of the photon energy is used to remove the electron from the shell and the remainder is converted into kinetic energy. The energy of the electron is given by

$$E_{\mathrm{e}} = \mathrm{h}\nu - E_{\mathrm{b}}, \tag{1.1}$$

where $\mathrm{h}\nu$ is the energy of the photon and E_{b} the binding energy of the shell from where the electron was removed. Only electrons with binding energy smaller than the photon energy can be removed, with highest probability for the most tightly bound shells. This means that X-rays interact mostly with electrons in the inner atomic shells.

After an electron has been removed, the positive ion returns to the fundamental state by filling the gap left by the removed electron with an electron from an outer shell. This transition is done either by emission of a fluorescent X-ray with energy equal to the difference between the two shells, or by non-radiative processes, mainly the emission of an Auger or Coster-Kronig electron with an energy equal to the difference between the energy of the electronic transition and the ionisation energy of the shell from where the electron was ejected. For the energies used in this work (typically under 30 keV), when using xenon as the absorbing gas, mostly electrons from the L-shell are removed. The L-shell fluorescence yield for xenon is 0.10 ± 0.01 [3], which means that around 90% of the atom relaxation results from non-radiative transitions.

Figure 1.1 shows the photoelectric absorption cross section for X-rays in xenon and tetrafluoromethane (CF_4), the gases used in this work. For both gases, the photoelectric absorption cross section has a behaviour proportional to $E^{-3.5}$, but for xenon, there are peaks of absorption at energies near the K- and L- absorption edges ($E_{\mathrm{K}} = 34.6\,\mathrm{keV}$, $E_{\mathrm{L}_1} = 5.45\,\mathrm{keV}$, $E_{\mathrm{L}_2} = 5.10\,\mathrm{keV}$ and $E_{\mathrm{L}_3} = 4.78\,\mathrm{keV}$). The K-shell energies of carbon and fluorine are in the order of hundreds of eV and do not play an important role at the energy range of this work. Their K-edge is below the range of the graph.

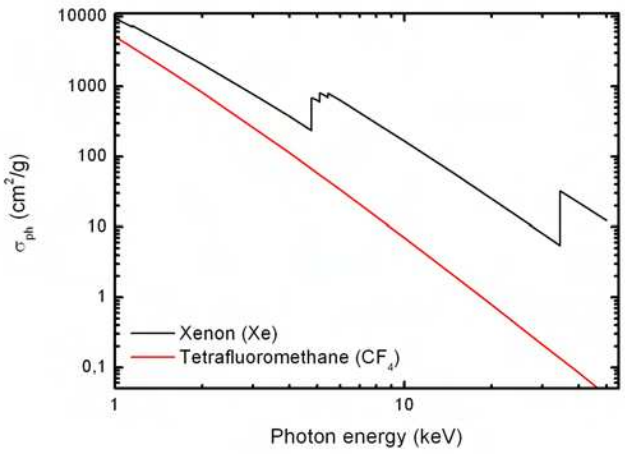

Figure 1.1: The photoelectric absorption cross sections for xenon and tetrafluoromethane as a function of the X-ray energy interacting with the gas.

At energies above a few hundred keV, Compton scattering starts to dominate the interactions. This effect happens when a photon transfers only part of its energy to a free electron (electrons in outer shells can be considered free, because their energy is much lower than the energy of the photon). The direction and the energy of the photon change, according to the amount of energy transferred to the recoil electron. Spectra of high energy X-rays or γ-rays, usually have a broad continuous distribution due to Compton scattering.

Above 1.02 MeV, the photon energy exceeds the double of the rest mass of one electron. From this point on, the production of an electron positron pair is possible. The effects of Compton scattering and pair production become important only for energies much above those used in this work. Below 30 keV these effects are negligible.

If the thickness of the material where the X-rays penetrate is not enough to absorb all the photons, then a fraction of the incident radiation is transmitted. For a given energy, this fraction is a function of the probability per unit path length that the photon is removed from the initial beam:

$$\frac{I}{I_0} = e^{-\mu t}, \tag{1.2}$$

where I and I_0 are the transmitted and incident X-ray intensities, μ is the linear attenuation coefficient of the material and t is its thickness. For a given material, the transmitted X-ray intensity drops exponentially with the thickness. Figure 1.2 shows the transmission of X-rays by 1 metre of air, and by a 25 µm Mylar™ window aluminised with a 1 µm thick layer, as a function of the energy. The product of both curves is also shown, corresponding to a common experimental situation, where the X-ray source is placed at a distance of 1 m from the detector. The aluminium K-edge

at 1.6 keV is noticed in the transmission curve. The curve of air, also shows the slope at the argon K-edge at 3.2 keV.

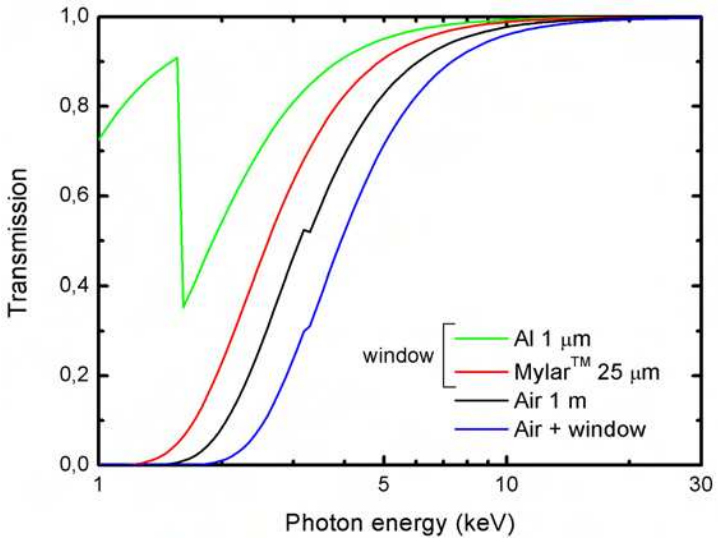

Figure 1.2: The transmission of X-rays as a function of their energy through 1 m of Air, a 25 µm thick aluminised Mylar™ window and both.

1.1.2 Electrons

Monoenergetic electrons, such as the photoelectrons ejected from a monoatomic gas due to a monoenergetic X-ray beam, lose their energy through several Coulomb interactions and radiative processes. Hans Bethe developed a theory which allows calculating the collision stopping power of particles in matter [4] above 100 keV[2]. The *stopping power*, referred also as the *specific energy loss*, is the differential energy lost in an infinitesimal path length:

$$S(E) = -\frac{dE}{dx}. \tag{1.3}$$

With electrons, the radiative processes of energy loss consist of *bremsstrahlung* radiation and occur whenever a charged particle accelerates. From the formulæ of the collisional and radiative stopping powers, it is possible to conclude that the relationship between both contributions is a function of the electron energy and the atomic number of the medium [5]:

$$\frac{(dE/dx)_{\mathrm{r}}}{(dE/dx)_{\mathrm{c}}} \approx \frac{EZ}{700} \tag{1.4}$$

where the indices r and c denote the radiative and collision stopping powers and the energy is in MeV. At the energy range (1–30 keV) and with the gases used in this work

[2]This is not the range used in this work, but the description in this subsection is believed to help understanding the ptocesses undergone by the photoelectrons until the primary cloud is generated

(Xe and CF_4), the right term of the equation is always much smaller than 1, meaning that the radiative effects can be neglected.

Since electrons are light particles, whenever they undergo a Coulomb interaction, their direction changes. Their path until all the kinetic energy is absorbed is not a straight line, but a sinuous trajectory. For low energies, an empyrical method can be used to estimate the maximum range of the electrons in a material. If equation 1.3, is rewritten to isolate the term dx:

$$dx = -\frac{dE}{S(E)}, \tag{1.5}$$

and the behaviour of the stopping power $S(E)$ is known, the path length is determined by integrating the inverse of the stopping power from the initial kinetic energy until it stops:

$$x = \int_0^E \frac{dE}{S(E)}. \tag{1.6}$$

The knowledge of the electron range is helpful to estimate the best position resolution of a gas in X-ray imaging, because the range of the photoelectron influences the position resolution at high energies. This effect is described in section 2.3.2.

1.1.3 Ions

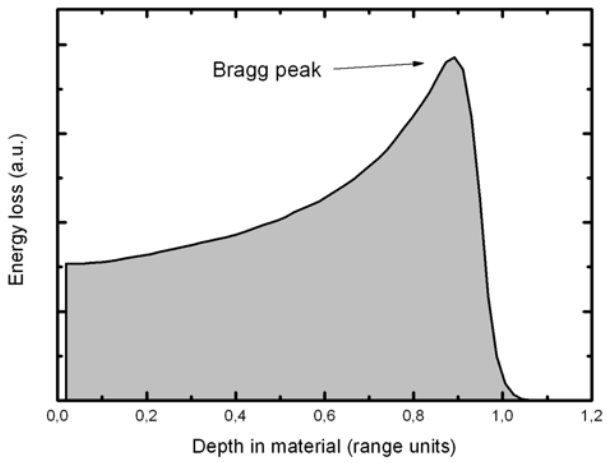

Figure 1.3: A typical curve of the energy lost by a proton in a material. There is not much energy loss at the beginning of the path, but as the proton penetrates the medium, the energy loss increases and, at some time, it starts capturing electrons from the material. This corresponds to the Bragg peak. After that, it loses all its energy within a short range.

Ions are much heavier than electrons. Those generated by ionising radiation have a very low kinetic energy. Due to their very low mobility even under high electric fields,

they move very slowly when compared to electrons. The time they take to drift under the influence of electric fields is very long.

With energetic ions generated by nuclear reactions or supplied from accelerators the case is different. When they penetrate a medium, they also undergo Coulomb interactions with the orbital electrons within the absorber atoms. Interactions with the nuclei can also occur but, in that case, the energy loss is negligible. The energy loss of ions as a function of the depth of penetration has the typical shape shown in fig. 1.3.

At the beginning of the track, the energy loss is smaller, but it increases as the ion loses its energy and penetrates the material. At some point, the energy of the ion becomes low enough and it captures electrons from the atoms of the material, reaching a maximum of energy deposition. After reaching this maximum—called the *Bragg peak*—it loses almost all its energy within a very short distance. For heavy ions, the Bragg peak becomes more pronounced and most of the energy deposition occurs near the end of their path. Because of their low energy deposition along their path and sudden stop at the end, they are used in cancer therapy and other medical applications, representing minimal radiation damage of healthy tissue, and maximal interaction in the diseased region.

1.1.4 Neutrons

According to their kinetic energy, neutrons can be thermal, epithermal, slow or fast. In this work, the development of a thermal neutron imaging detector is proposed, which means that only neutrons with a very low kinetic energy ($E \approx 0.025\,\mathrm{eV}$) and respective detectors will be focused here.

The generation of neutrons can be done through many different nuclear reactions [5, 6]. Stable isotopes with relatively loosely bound neutrons (binding energy of the order of 1 MeV) are very prone to react with α-particles or other ions, producing neutrons, among the reaction products. One example is the reaction

$$^{9}\mathrm{Be} + {}^{4}\alpha \longrightarrow {}^{1}\mathrm{n} + {}^{12}\mathrm{C},$$

which led to the discovery of the neutron. If a long-lived α-emitter (for example ^{226}Ra) is mixed with beryllium-9, neutrons can be produced at a constant rate. The energy of the emitted neutron depends on the energy of the α-particle and on the Q-value of the nuclear reaction (5.7 MeV in the case of ^{9}Be). If excited nuclei are among the products of the reaction, there is also emission of γ-rays, when the nucleus relaxes.

Many other particles besides α-particles can be used to trigger a nuclear reaction, including the production of *photoneutrons* with γ-rays. In the ISIS spallation source at the Rutherford Appleton Laboratory (RAL), negative hydrogen (H^-) ions are accelerated in two stages before their electrons are removed and the bare protons are introduced in a synchrotron ring for the third and last acceleration stage. This charge transfer allows a much higher proton current inside the ring, making the ISIS the most powerful neutron source in the world. The final energy of the protons is 800 MeV, in pulses of 4 µC every $^{1}/_{50}$ s. The protons at 85 % of the velocity of light hit a tungsten

target ejecting neutrons from its nuclei. 15 to 20 neutrons per proton are generated [7], with an energy distribution around 1 MeV, with a tail towards the high energies. The fast neutrons must then be *moderated* to energies of the order of meV. This is done using low atomic number materials such as hydrogen, methane and water.

When fast neutrons penetrate the material, their energy loss (moderation), is done through interactions with the nuclei from the media. Since the nuclei are a very small fraction of the volume of a material, neutrons can travel quite long distances until they interact. However, in each interaction they can lose a great part of their energy. In each elastic collision, part of the neutron energy is transferred to the nucleus. Inelastic collisions also occur when the recoil nucleus becomes excited, leading to the emission of γ-radiation upon relaxation. In this case, the loss of energy of the neutron is even higher than with elastic collisions.

The fraction of the energy transferred to the absorber nuclei becomes higher as the size of the nucleus approaches the size of the neutron. In one single collision with a hydrogen nucleus, the neutron can lose almost all its energy. The sensitivity of neutrons to the presence of hydrogen atoms is a reason why neutrons are used to detect the presence of organic materials.

As neutrons get slower, the transfer of energy to the nuclei of the medium becomes less important and other type of interactions start to occur. For *thermal neutrons*, neutron induced nuclear reactions are the main interactions.

Since the products of neutron-induced nuclear reactions are heavy charged particles, the problem is converted into an interaction of ions with the gas, as described previously. The ions interact with the electrons in the gaseous medium, removing them from the atoms. These electrons are then multiplied and collected as pulses, which carry information of the Q-value of the nuclear reaction and, if a 2D-MHSP is used, the approximate position of the nuclear reaction.

Lithium-6, boron-10 and helium-3 are among the most popular elements used in neutron detection. Their cross section for neutron induced nuclear reactions is proportional to $1/E$ [5] up to 1 keV neutron kinetic energy.

While lithium-6 must be embedded in solid crystals, being excluded from the topic of gaseous neutron detectors, boron-10 is used within the molecule of BF_3. The neutron capture cross section of ^{10}B is one order of magnitude higher than that of ^{6}Li. The nuclear reaction gives origin to one ^{7}Li nucleus and one α-particle, with two different Q-values corresponding to the ground or excited state of the ^{7}Li nucleus:

$$^{10}\mathrm{B} + {}^{1}\mathrm{n} \longrightarrow \begin{cases} {}^{7}\mathrm{Li} + {}^{4}\alpha & 2.79\,\mathrm{MeV} \\ {}^{7}\mathrm{Li}^{*} + {}^{4}\alpha & 2.31\,\mathrm{MeV} \end{cases}$$

In the last case, there is still the emission of gamma-radiation. The spectrum is composed of the two peaks corresponding to the Q-value of the reaction, together with some low energy distribution due to the electronic noise and gamma-radiation and, eventually, the wall effect continua caused by incomplete tracks of the reaction products hitting the walls of the detector.

The gas helium-3 is an isotope with a cross section even higher than lithium or boron. Its reaction has a single branch of products, with a well defined peak at 764 keV.

A helium-3 nuclei, upon neutron capture, is converted into a proton with a kinetic energy of 573 keV, and a 191 keV triton according to the nuclear reaction

$$^{3}\mathrm{He} + {}^{1}\mathrm{n} \longrightarrow {}^{1}\mathrm{p} + {}^{3}\mathrm{H} + 764\,\mathrm{keV}.$$

Although the Q-value of the $\mathrm{n}\left({}^{3}\mathrm{He}, \mathrm{T}\right)\mathrm{p}$ reaction is lower than for $\mathrm{n}\left({}^{10}\mathrm{B}, {}^{7}\mathrm{Li}\right)\alpha$, the range of the reaction products is higher, because they are lighter. Nevertheless, for imaging purposes, the range of the products must be reduced by increasing the gas pressure inside the detector. This reduces the mean free path of the electrons, reducing the multiplication factor of the gas. The decrease of the multiplication factor with the pressure is much more pronounced in BF_3 than in ^{3}He, which drastically limits the signal-to-noise ratio of BF_3 at high pressures. Furthermore, as will be described in chapter 4, using ^{3}He, the problem of the high range of the reaction products is solved adding a heavier gas with a low gamma-efficiency, to absorb the heavy charged particles within a short range.

1.2 Historical milestones

Before the introduction of Micropattern Gaseous Detectors (MPGD), a long research work has been carried out over many decades to develop gaseous radiation detectors. The types of detector shortly described in this section are only a small fraction of all the work developed. Here, they are organised to reflect major steps in terms of radiation detection itself, energy resolution, use of scintillation light to enhance energy resolution and position resolution. Following this very brief historical review, it is simple to understand how the development MPGDs was the logical step in gaseous detectors.

In gaseous detectors, an electric field between the cathode and the anode electrodes is used to separate the ion pairs generated by the ionising radiation. When an ion pair is formed, in the absence of an electric field, the free electron and the positive ion recombine and equilibrium is reestablished. However, if an electric field is applied, the electrons drift away from the positive ions and the probability of recombination decreases. Some electrons are able to reach the anode and generate a charge pulse. As the electric field increases, the amount of electrons able to reach the anode increases.

Above some value, every free electron reaches the anode. Within this range, the increase of the electric field does not increase the number of electrons. This plateau is called the ion saturation and corresponds to the electric field range used in ionisation chambers. Even if the amount of electrons reaching the anode does not increase with the electric field, the velocity reached by the electrons between each collision keeps increasing, leading to shorter pulses.

At some point, the electric field accelerates the electrons enough to acquire a kinetic energy between collisions capable of removing other electrons from the atoms of the gaseous medium. Now, the increase of the electric field, also increases the number of

ions each electron is able to create. The new free electrons removed from the medium are also accelerated and further remove other electrons, forming the already mentioned Townsend avalanche. The fractional increase in the number of electrons per path length is given by

$$\frac{1}{n}\frac{dn}{dx} = \alpha, \tag{1.7}$$

known as the Townsend equation, where α is the first Townsend coefficient. Its solution shows that, in an avalanche, the increase of electrons is exponential. The first Townsend coefficient is zero below the ionisation threshold but grows with the electric field above that threshold. This is the proportional region, because the total number of electrons in the avalanche is proportional to the number of primary electrons.

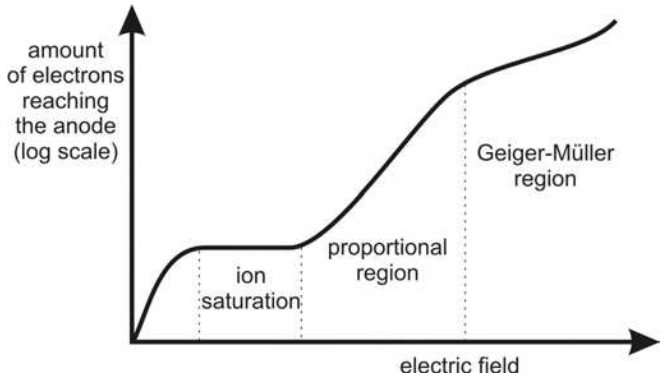

Figure 1.4: The different regions of operation of gaseous detectors.

Further increasing of the electric field, increases the gain in charge. At some point—we will skip the region of limited proportionality, where there are so many positive ions that there are space charge effects which distort the electric field—the number of ion-pairs ceases to be proportional to the primary electrons and the Geiger-Müller region is reached. In this region one single interaction makes the whole volume ionised and the pulses have all the same amplitude, independently of the primary charge produced by the interaction of the radiation.

Figure 1.4 shows the different regions of operation described above. The next subsections describe examples of detectors working in the last two regions, but with a special emphasis on the proportional region.

1.2.1 The Geiger-Müller counter

The most basic gaseous radiation detector is a simple sealed cylindrical tube working as a cathode, filled with gas (usually a noble gas mixed with an organic gas forming a Penning mixture), with a thin anode wire at its centre. The Geiger-Müller counter was introduced in 1928 [8]. In this device, the ion pairs generated by an ionising particle are subject to a very high electric field. The accelerated electrons are able to further ionise atoms and molecules from the medium within their free path length and to excite some molecules, which, upon relaxation emit UV-photons. These photons

are absorbed elsewhere inside the detector, removing electrons from the outer shells of atoms, creating more free electrons. The process of ionisation and excitation with UV-light emission escalates and in less than one microsecond, the whole tube gets ionised and a large charge pulse can be collected from the anode wire. The pulse amplitude does not depend on the number of primary electrons. Since all the pulses have the same amplitude, this detector does not have energy resolution and serves as an event counter. It is very commonly used as a radiation monitoring device for safety and security purposes, due to its portability, sturdiness and insensitivity to external factors such as interference or electronic noise.

1.2.2 The Gas Proportional Counter

If the same geometry of the Gieger-Müller counter is used, but the operation voltage is reduced to bring the electric field to the proportional region, the pulse height is proportional to the charge of the primary electron cloud. Since the size of the cloud is also proportional to the energy of the ionising radiation, the charge pulse carries information of the energy of the incident particle. Using a pulse height analyser, an energy distribution of the incident radiation can be plotted, revealing the energy of the particles hitting the detector.

The electric field inside a grounded tube with a thin wire passing at its axis, as a function of the distance r to the axis is given by:

$$\mathcal{E}(r) = \frac{V}{r \ln(b/a)}, \tag{1.8}$$

where a and b are the anode wire and cathode tube radii, respectively and V is the voltage applied to the wire.

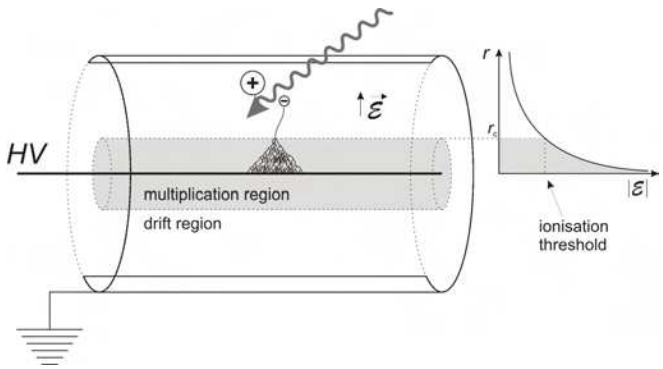

Figure 1.5: The Gas Proportional Counter. The electric field inside the detector volume varies according to equation 1.8 (graphic on the right). The detector is divided in a drift region where the radiation is absorbed and in a multiplication region, where the electric field is above the ionisation threshold.

Figure 1.5 shows how the Gas Proportional Couter works and how the electric field changes inside the detector. The detector volume is naturally divided into two different

coaxial regions. The outer region, which goes from the detector walls to a couple hundred µm from the anode wire is called the drift region. Here, the incident particles are absorbed and the electric field is just high enough to avoid the recombination of the ion pairs, making the electrons drift towards the vicinity of the anode wire. As the electrons approach the wire, the electric field increases and, at some critical distance r_c, the ionisation threshold is reached and charge multiplication starts. The electrons enter the multiplication region.

When the voltage in the anode wire is increased, the gain in charge of the detector increases, because the first Townsend coefficient also increases. The gain in charge M can be related to the Townsend coefficient by [5]:

$$\ln M \quad = \quad \int_a^{r_c} \alpha(r) dr \quad = \quad \int_a^{r_c} \alpha(\mathcal{E}) \frac{dr}{d\mathcal{E}} d\mathcal{E}, \tag{1.9}$$

taking into account that α is a function of the gas and the electric field.

From this, Diethorn [9] derived an expression for the variation of the gain as a function of the biasing voltage, taking into account the cylindrical geometry of the Gas Proportional Counter:

$$\ln M = \frac{V}{\ln\left(b/a\right)} \cdot \frac{\ln 2}{\Delta \mathrm{V}} \left(\ln \frac{V}{pa \ln\left(b/a\right)} - \ln \mathrm{K} \right) \tag{1.10}$$

where p is the gas pressure, ΔV is the potential increase felt by one electron between two ionising collisions and K is the minimum value of the *reduced electric field* $\mathcal{E}/p$ for which ionisation occurs. ΔV and K are constant and a property of each gas.

The radius of a proportional counter is typically of the order of 1–2 cm and the anode wire is around 25 µm thick or less. The biasing voltage is around 1000 V for a 1 cm radius and the gain in charge is typically 10^4 in xenon. The energy resolution is around 14 % for 5.9 keV. The pulses are a few microseconds long, due to the distance between the anode and the cathode, which eventually limits the high rate capability.

1.2.3 The Gas Proportional Scintillation Counter

The Gas Proportional Scintillation Counter (GPSC) [10] is one of the great achievements of the Physics Department of the University of Coimbra and has been developed over many years in the Atomic and Nuclear Instrumentation Group (GIAN).

If the primary electrons accelerated by an electric field do not have a kinetic energy high enough to ionise the atoms of the medium when they collide, they can bring them to excited states by inelastic collisions. Upon deexcitation, ultra-violet light is emitted isotropically. Since each electron can generate many scintillation photons, the amount of light produced can be very high. This light can be detected with a standard *photomultiplier tube* (PMT), which outputs a signal proportional to the intensity of the light hitting its photocathode. The proportionality of the pulse height with the energy of the incident radiation is maintained over the whole process of detection. In the detector itself there is no charge multiplication. This is done inside the PMT.

The standard GPSC is composed of a *drift/absorption region* limited by the grounded detector window on one side and a polarised grid a few centimetres away, generating a uniform drift electric field. Parallel to the first grid, downstream, there is a second grid at a higher potential, creating another uniform, more intense electric field, accelerating the electrons enough to excite the atoms or molecules of the medium, but not ionise them. This is the *scintillation region*. The light readout is made with a PMT, coupled to the scintillation region.

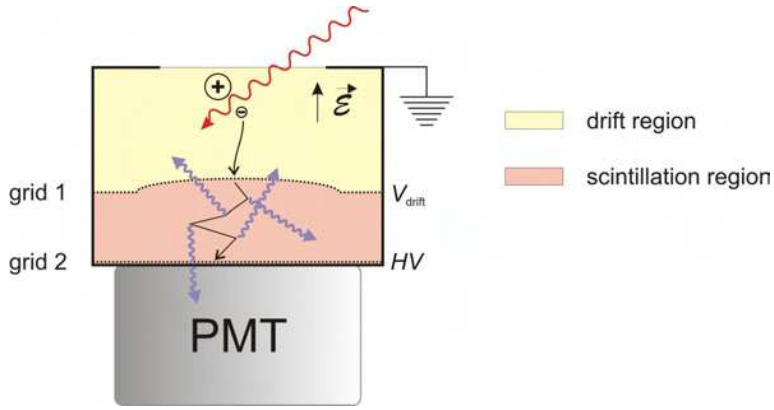

Figure 1.6: The Gas Proportional Scintillation Couter with an ellipsoidal grid and a photomultiplier tube as the photosensor.

The latest GPSCs introduced some subtleties in their design. The first grid was flat, leading to the loss of light intensity at the borders of the optical sensor due to the smaller solid angle. The problem was hindered by substituting it by an ellipsoidal grid [11]. This allowed to build gaseous counters with a larger detection area, while keeping a good energy resolution. This is the major advantage of these detectors. Due to the high intensity of secondary UV-light, the statistical quality of each event is much higher, with less fluctuations. With the GPSC, typical energy resolutions of 8 % for 5.9 keV are easily achieved [12].

1.2.4 The Multiwire Proportional Chamber

In 1968, Nobel Prize laureate Charles Charpak introduced the Multiwire Proportional Chamber (MWPC) [13]. It consists of an array of proportional counters in a plane of parallel wires, separated by typically 1 mm. The cathode of the MWPC is composed of two parallel plates placed at both sides of the anode plane. With this setup it is possible to have sensitive areas of the order of square meters. The energy resolution is the same achieved with standard cylindrical proportional counters, since each anode wire works as an independent proportional counter. The primary charge is distributed over a few wires in the vicinity of the interaction point. The charge avalanche is also induced in the cathode planes.

The cathode planes can be composed of parallel strips, each one connected to an amplification and shaping electronic chain. This allows to determine the position where

the interaction took place. If the strips of one plane are oriented perpendicular to the strips of the other plane, the x- and y-coordinates of interaction are obtained making the MWPC the first 2D-imaging detector based on a proportional counter. Figure 1.7 shows the basic setup of the MWPC used for imaging.

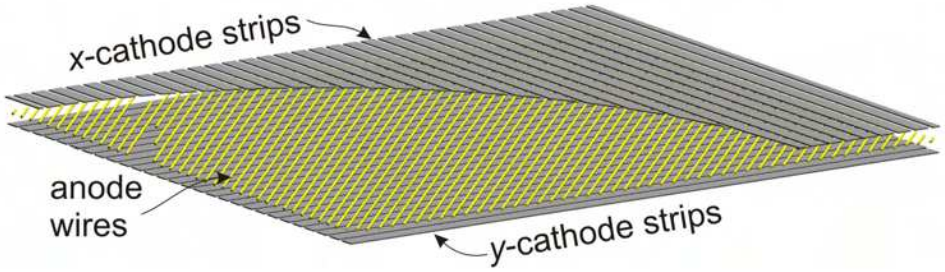

Figure 1.7: The Multiwire Proportional Chamber adapted for imaging. The cathode planes are divided in strips and the charge induced in the strips can be used to determine the x- and y-coordinates of the interaction point.

To avoid the use of many amplification channels, the cathode strips can also be interconnected through resistive or delay lines. The centroid of the charge avalanche is determined through centre of mass algorithms and it is possible to achieve a position resolution much below the distance between the anode wires [14–16]. In a recent work, position resolution of 700 µm (FWHM) was achieved in both directions for a $80 \times 80\,\mathrm{mm}^2$ area with delay lines [17]. The time of the pulses is of the order of a few hundreds of ns, related to the drift distance of the positive ions between the anodes and the cathodes, allowing to detect at considerable counting rates.

1.3 Micropattern Gaseous Detectors

As research in physics developed, the demands on the performance of radiation detectors increased substantially. The MWPC was an impressive breakthrough, but its construction is not trivial. This kind of chamber needs some maintenance and is not sturdy enough to allow building a portable detector. The need of robust detectors capable of operating at high counting rates, at the same time providing good energy resolutions together with imaging capability posed new challenges and a new approach was needed. High counting rates require very short pulses, which immediately suggests small distances between anodes and cathodes. However, for imaging capability, the largest area possible is needed. The new technologies on precision circuit board printing techniques opened the door for Micropattern Gas Detectors (MPGD). Very dense patterns could be printed in some substrate over large areas giving origin to a new generation of gaseous detectors.

Reference [18] describes a model in line with Diethorn's work (eq. 1.10), based in a generic charge gain expression, for avalanche gas detectors. The expression is dependent on the threshold energy for ionisation W (the outer-most atomic electron binding energy) and on the electron mean free path λ in the medium as parameters:

$$\ln M = \frac{V}{A} \exp\left(-\frac{AB}{V}\right), \tag{1.11}$$

with

$$A = W \ln\left(\frac{b}{a}\right), \qquad B = \frac{a}{\lambda},$$

for cylindrical geometries. V is the voltage difference between the cathode, at a distance b from the anode with a thickness $a/2$. This equation can be used to fit any gaseous avalanche counter, however, to accurately determine W and λ, small corrections must be made (for example in the voltage V), for non-cylindrical geometries. These corrections are more important for three- or four-terminal devices, i.e., those where biasing voltages must be applied not only in cathodes and anodes, but also in a third or fourth electrode, such as a radiation window or grids.

1.3.1 The Microstrip Gas Detector

There is no doubt that the MWPC, as a very simple concept, has brought the design of gaseous detectors one large step further. The idea of a repeating pattern covering a large area was definitely to be exploited. The next step was done by Anton Oed [19], by printing the anodes as strips in a planar insulating substrate and the cathode strips in the same plane, between the anode strips. This planar structure, consisting of a single plate (the Microstrip Plate—MSP), allowed having many proportional counters in the same substrate. The new high resolution techniques of photolithography, allowed to print a pattern with a pitch of around 200 µm, with anode and cathode width of 10- and 100 µm, respectively, at a distance below 100 µm, reducing very much the voltage needed to achieve the necessary electric field for charge multiplication. At the beginning, the substrate was a commercial mask plate with a chromium layer where the pattern was etched. A schematic view of a small region of a MSP is shown in fig. 1.8.

The MS pattern can be repeated indefinitely and areas of the order of 100 cm^2 are used nowadays as a standard. This detector geometry has other advantages. If it is evaporated with some fotosensitive material, such as caesium iodide (CsI), it can serve as a photosensor, multiplying the electrons generated by the photocathode. This has been tested in a Gas Proportional Scintillation Counter, replacing the PMT, resulting in a much smaller and sturdier final detector, with little limitations in what concerns increasing its size [20, 21].

To exploit the intrinsic 2D capability of the MSP, for one of the coordinates, the anode strips can be made independent, using readout electronics for each anode strip or group of strips, or interconnected by resistive or delay lines. In these last two possibilities, the position of interaction is determined by the difference in amplitudes

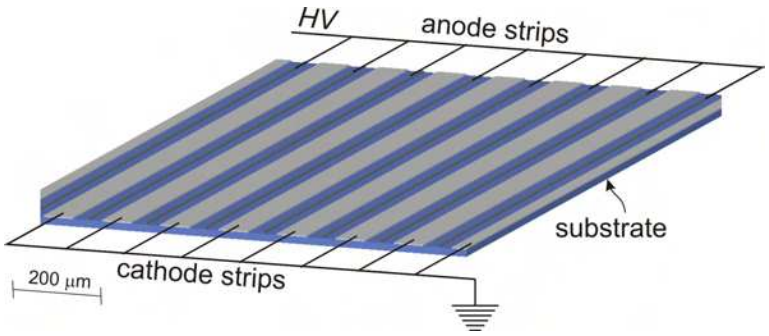

Figure 1.8: In the Microstrip Plate the anode wires are replaced by printed anode thin strips and the cathode strips are printed between the anodes. With a a pitch of 200 µm, the anodes are 5 times closer than in the MWPC.

or time of arrival of the signals at each end of a line. The second coordinate can be determined by etching strips on the opposite side of the substrate, perpendicular to the anode strips, to collect the charge induced through the dielectric substrate. References [22, 23] are examples of works applying this principle with X-rays and neutrons, with position resolutions of 0.6 mm (FWHM) and 1.3 mm (FWHM), respectively.

The Micro Strip Gaseous Detector achieved gains of the order of 10^3. The positive ions generated in the avalanche tend to remain on the surface of the insulating substrate and influence the electric field at high radiation rates due to space charge effects. To achieve higher gains, higher voltages must be used and, due to the small distance between the anode and the cathode strips, the probability of discharge increases. The sensitivity of this device to electrical discharges is a drawback. In fact, the energy released in one spark is usually enough to cause permanent damage, resulting in short circuit between the electrodes. Further development made the electron-conductive Schott S8900 glass as standard material for the substrate, to avoid the upcharging effects [24].

1.3.2 The Micromesh Gaseous Structure

The Micromesh Gaseous Structure (Micromegas) was introduced in 1996 [25] as an alternative to the MSP, minimising the time spent collecting the positive ions and, at the same time, providing a very high gain in charge and a very high tolerance to electrical discharges. It is a very asymetric two-stage parallel-plate avalanche chamber. A 3 µm thick metallic micromesh of $25 \times 25\,\mu m^2$ squares with 8 µm wide edges is placed over a striped printed circuit board (PCB), at a distance of 50–100 µm. It separates a conversion region, with a depth of a few mm, from the thin charge amplification gap, between the mesh and the PCB, working as the anode plane. It is possible to achieve very high electric fields in the amplification gap due to its short depth. The electrons are collected in the strips etched on the PCB and the positive ions are quickly collected on the micromesh.

This detector can also be manufactured with a large sensitive area and used for

2D-imaging. Reference [26] used a clever setup of resistive Ni-Cr strips to determine the position of interaction along the strips through resistive charge division, achieving position resolutions under 0.5 mm for a sensitive area of $13 \times 6\,\mathrm{cm}^2$.

1.3.3 The Gas Electron Multiplier

The Gas Electron Multiplier (GEM) was first presented as "a new concept for electron amplification" [27], intended to overcome the problem of gain loss due to high counting rates in Microstrip Plate detectors. It is as simple as a thin Kapton™ foil (typically 50 µm thick), copper-clad (5 µm) on both sides and etched with a matrix of channels. The channels are the vertices of hexagons with typically 140 µm long edges. If a voltage difference between both copper layers is applied, the electric field inside the holes is very high and the electrons passing through the holes are multiplied. The layout of the GEM is shown in fig. 1.9, where the biconical shape of the holes can be seen. This shape avoids sparking between the two electrodes across the holes.

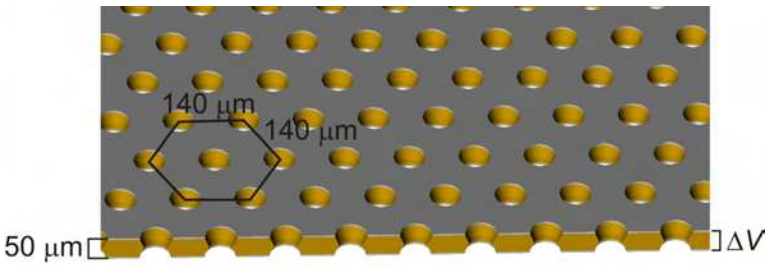

Figure 1.9: The Gas Electron Multiplier is composed of a 50 µm thick Kapton™ foil (yellow) copper-clad on both sides (grey), perforated with biconical holes in a hexagonal matrix. By applying a suitable drift field and voltage difference between both sides of the GEM, the primary electrons are focused towards the holes and multiplied, emerging on the other side in a much larger number.

Since the electric field lines pass through the holes, there is an effect of focusing the drifting electrons, which means that the GEM is completely transparent to electrons, when suitable voltages are applied. The GEM has been subject to thorough research due to its potentiality and in the mean time, it is seen as a detector itself, rather than a charge preamplification device.

Since there is transmission of charge, it is also possible to cascade several GEMs. A triple-GEM detector achieves gains above 10^4 in pure xenon [28], and 10^5 in Xe/CO_2 mixtures [29]. It was also successfully used as a photosensor [30, 31], achieving very promising results in studies of ion back-flow in gases.

The pulses of a GEM are a few ns long, as expected due to its small dimensions. For 2D-imaging, the charge transmitted by the GEM can be collected with readout pads, CCDs, or other position sensitive charge readouts [32–34].

Recently, there have been some promising further developments in GEMs. One of them is the thick-GEM (THGEM) [35]. It is similar to a GEM, but with a much

coarser pattern. The substrate material is a simple Cu-plated G10 or FR4 printed circuit board with a thickness around 1 mm, where holes of 1 mm diameter are drilled. The edges of the hexagons are of the order of millimetres (up to 5 mm). This structure requires voltages between 1000– and 2000 V to operate, but it is very robust and resistant to sparks, achieving higher gains than the single-GEM. Submillimetric position resolutions have been achieved with the THGEM and a 2D-readout pad [36].

Other interesting setup based on the GEM is the Micro-Induction Gap Amplifying Structure (GEM-MIGAS) detector [37, 38], which works as a hybrid, combining the working principles of the GEM and the MicroMegas. A GEM was placed at a distance of 50 µm from a micromesh, generating a very intense field between the GEM's bottom electrode and the mesh, in addition to the field inside the holes. This gives origin to two amplification stages, improving the charge gain when compared to the MicroMegas or the GEM alone, allowing to operate at lower voltages, increasing the detector's stability.

1.3.4 The Micro-Hole & Strip Plate

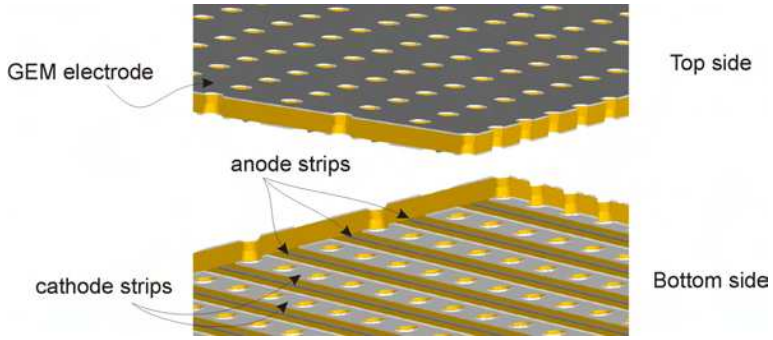

Figure 1.10: The MHSP is a thin Kapton™ foil, copper-clad on both sides. On one side (top) the GEM pattern is etched and on the opposite side (bottom) the holes emerge from the cathode strips of a Microstrip pattern.

Along the last sections it has been noticed that MPGDs tend to improve their performance when they are cascaded in more than one amplification stage. In fact, solutions such as GEM-MSP, or triple-GEM, or even the GEM-MIGAS, use as main arguments the fact that cascaded elements provide higher gains at stable operation. It should be remembered how these devices are sensitive to electrical breakdown, often resulting in the loss of the detecting structure after a spark.

In this sequence, the Micro-Hole & Strip Plate (MHSP) [39,40] was developed in the Physics Department of the University of Coimbra, as a hybrid micropattern detector exploiting the characteristics of a GEM, followed by a MSP within the same substrate (fig. 1.10). It consists of a 50 µm thick Kapton™ foil, copper-clad on both sides. A GEM pattern is etched on one side, and a MSP pattern on the opposite side, with the holes emerging in the cathode strips. Figure 1.11, shows the working principle of the MHSP, with the two electron multiplication stages.

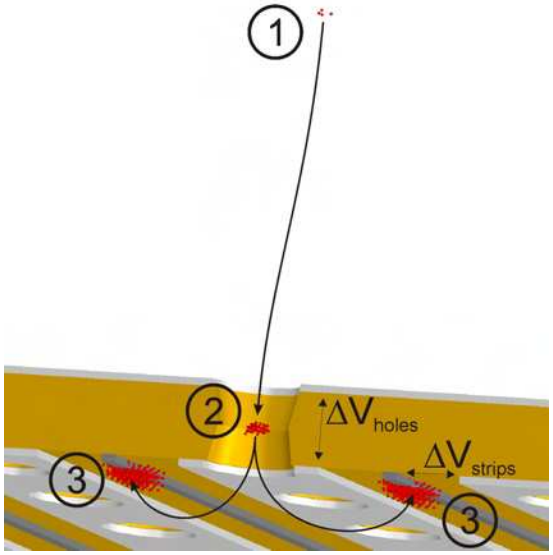

Figure 1.11: A small region of a detector based in the MHSP, focused in what happens in the vicinity of one of the holes. The electrons are represented by the small red spheres. 1. The primary electron cloud, after the X-ray photon has been absorbed, drifts towards the holes. 2. Inside the holes, since the electric field is very high, they are strongly accelerated, gaining enough energy between collisions to ionise more atoms from the gas, giving origin to a Townsend avalanche. 3. When the electrons leave the holes, they are once again subject to a high electric field in the vicinity of the strips at higher potential, where a second avalanche occurs and the number of electrons is again multiplied.

The primary electrons drift towards the MHSP, due to the electric field generated by the potential difference between the detector window and the GEM electrode of the MHSP. As in the GEM, because the electrodes on the opposite side of the holes are polarised with a suitable voltage difference, the electric field lines penetrate the holes, focusing the electrons. Inside the holes, the first avalanche occurs. When the electrons emerge on the Microstrip side through the cathode strips, they are again accelerated, this time towards the anode strips, where they undergo a second multiplication.

The process of manufacturing the MHSP is similar to the GEM, with only the extra step of etching the MS-pattern, aligned with the holes. The MHSP has achieved charge gains higher than with a single-GEM [41], and similar energy resolutions. It is capable of working at very high counting rates. At 5×10^5 Hz/mm^2 and a charge gain of 10^4 in pure xenon it had a gain reduction of only 5 % [42]. It has also been tested at the end of a GEM cascade [43]. With a CsI photocathode evaporated on its surface, it has also been used as a photosensor [44], which developed to a new concept, the Photon Assisted Cascaded Electron Multiplier (PACEM). It used a MHSP to generate scintillation light, to be detected by another MHSP-photosensor [45]. The ion back-flow was reduced by collecting the positive ions in a mesh between both MHSPs. The

imaging capability has also been tested with a GEM/MHSP cascade, using a Wedge and Strip readout pad [46].

Chapter 2

The Micro-Hole & Strip Plate as an imaging device

One of the conclusions of the last chapter is that the break through of micropattern detectors has its success also related to their intrinsic position detection capability, due to their capability to have a sensitive region with a large area. With small changes in their design, it is possible to accurately determine the position of the interaction. There are many approaches for electronic readout of the position and pulse height analysis. From the very beginning of the MSGC, in 1988, Oed presented results of the imaging behaviour of this detector, using delay lines connecting each of the MS anodes for one of the dimensions and each of the backside-readout strips for the other dimension [19]. The time difference between the arrival of both signals to the edge of each delay line carried information about the position where the electron avalanche was formed. The use of delay lines for position determination is very popular and was broadly used for applications not requiring operation at high rates (for example [34]). Delay lines are however difficult to implement in such small structures, due to the small distance ($\sim$100 µm) between each strip. The possibility of using different electronic boards for the delay lines increase the complexity of both the electronics and the manufacturing of the detector.

The use of high density electronics has also been broadly investigated, with very good results in terms of position resolution. In fact, this should be the optimal solution, since each detector element can work independently from the others and the electronic noise does not propagate along the whole structure [47, 48]. These systems are also very fast, providing very good position resolution at high counting rates.

The separate readout devices are also very popular and have provided very interesting results. The example of Wedge and Strip (W&S) [49], a simple pad consisting of three electrodes with their size designed as a function of the spatial coordinate, has been tried with a combination of GEM/MHSP [46]. Other readout pads were developed and tested [33, 50], including CCDs for optical readout of He/CF_4 scintillation [51].

There are many possible setups of readout pads to be used with MPGDs. These pads collect the charge (directly or induced) in different layers of readout strips. The

strips can be interconnected by delay lines, with a resistor and a coil between each strip, or by resistive lines. Reference [47] describes some different readout pad geometries tested with GEMs.

The method of resistive charge division has the most advantages for the purpose of this work. A resistive strip is relatively simple to apply by photolithography. Its resistance is proportional to its length:

$$R = \frac{l}{wt}\rho, \tag{2.1}$$

where l is the length of the strip, w and t are the width and the thickness, respectively, and ρ is the resistivity of the material. If the length and the width of the strip are equal, it means that the resistive material is a square and the resistance is defined only by the thickness of the resistive layer. That is the so called *sheet resistance* and its units are $\Omega/\square$ (Ohms per square). To determine the total resistance of some strip, its sheet resistance must be multiplied by the length in units of width.

In the method of resistive charge division, the resistive strip is placed along one of the spatial dimensions. The charge pulses, on their way to the electronic chain are divided according to the resistance of the strip and their difference in height carries information of the position of the charge avalanche. This has been tried in many works [22, 26, 52–54], using many geometries. The major difference in this work is that the charge amplification and collection are within the same Kapton™ substrate, maintaining the compact philosophy of the MHSP, avoiding the use of extra readout pads. The charge amplification and position determination are all on a 50 µm Kapton™ foil.

2.1 The standard MHSP

The standard MHSPs used in this work are the result of several years of research and development. They consist of a 50 µm Kapton™ foil with 5 µm copper layers on both sides. The holes have inner and outer diameters of 50- and 60 µm, with the centres at a distance of 140 µm. On the MS-side, the anode strips have a width of 20 µm and the cathode strips are 100 µm thick. The pattern has a pitch of 200 µm. The total active area was $28 \times 28\,\mathrm{mm}^2$, which means that each MHSP had 140 anode/cathode strip pairs.

Figures 2.1(a) and (b) show the standard MHSP as described, where the hole dimensions, the strip widths and the layer thicknesses are shown. The MHSP was stretched over a Macor™ frame, working as a spacer, fixed to a stainless steel vacuum tight vessel, which served as the detector body. For the MHSP biasing, the electrical insulation and vacuum tightness was made by gluing stainless-steel connectors to Macor™ cylinders, which were then glued to the detector body with low vapour-pressure epoxy[1]. The different parts of the stainless steel detector body were coupled using

[1] Tra-Con Tra-Bond™ 2116 Low Vapour Pressure Epoxy Staking Compound

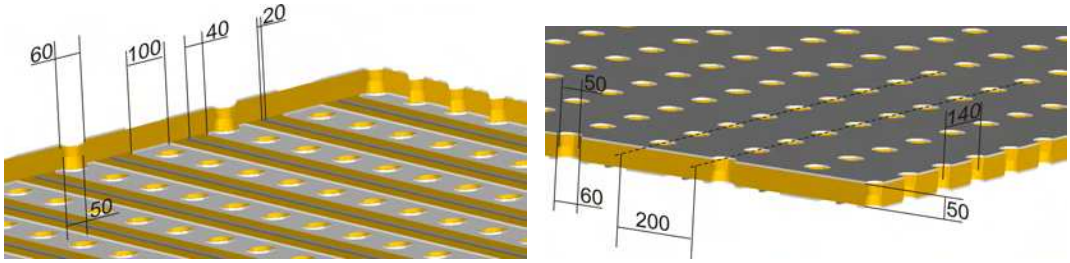

(a) (b)

Figure 2.1: The standard MHSP. All the measurements are in µm.(a) Bottom view. (b) Top view.

Viton™ O-rings for vacuum tightness. The low vapour pressure materials used in the manufacturing of the detector guaranteed the purity of the filling gas for a longer time.

The gas was purified every 24 hours, simply by collecting it to a special vessel at the temperature of liquid nitrogen, freezing it down. As the temperature slowly rose, the impurities, at a much lower partial pressure and with a much lower boiling point than the gas, were pumped out. When the gas reached its boiling temperature it was directed to the detector vessel until the desired pressure was reached. Organic impurities such as water and carbon dioxide have boiling temperatures much higher than those of the gas and remained in the solid state, not entering the detector.

The detector used for the experiments described in this section is shown in fig. 2.2. The detector window served also as the drift cathode. It was made of 25 µm aluminised Mylar™ foil, supported by a 3 mm thick stainless steel plate perforated with a 5×5 array of 2 mm diameter holes, with a pitch of 6 mm. The holes worked as colimators. The drift region was set to a depth of 5 mm. The distance between the MS-side of the MHSP and the grounded detector body underneath was 3 mm. The charge signals were collected directly from the anode strips of the MHSP.

2.1.1 Performance in pure Xenon

The performance of the standard MHSP has been studied operating this detector in xenon atmosphere [55]. The MHSP was biased first with a constant voltage across the holes and gradually increasing the voltage between the anode and cathode strips; then, the voltage between strips was kept constant while the voltage across the holes was increased. When the biasing voltages were too high revealing the eminence micro-discharges, the measurements were stopped. For all these conditions the charge gain and the energy resolution was measured and plotted as seen in figs. 2.3(a) and (b). The charge gain was calculated using a calibrated 2 pF capacitor and a BNC™ precision pulse generator to determine the gain due to the electronic amplification and shaping chain. For this, the w-value of xenon was taken into account ($w_{\mathrm{Xe}} = 22.1\,\mathrm{eV}$ at 5.9 keV [56]). The drift electric field was set to $\mathcal{E}_{\mathrm{drift}} = 120\,{}^{V}/_{cm}$.

A charge gain of 1.6×10^4 was achieved at stable operation, with energy resolutions

of $13,5\,\%$ for the 5.9 keV K_α line of a ^{55}Fe radioactive source and 7.8 % for the 22.1 keV K_α line from ^{109}Cd. The standard MHSP allowed total biasing voltages near 800 V. The pulse height distributions obtained for a charge gain of that order of magnitude are shown in fig. 2.4(a) and (b) for ^{55}Fe and ^{109}Cd radioactive sources, respectively. The signals are completely separated from the noise tail, which was below 30 eV in (a). This shows that the MHSP has a SNR high enough to provide soft X-ray detection.

The stability of the detector over time was also tested. The MHSP was biased with a drift field of $100\,\mathrm{V/cm}$ and the voltages across the holes and between the strips were 410- and 240 V, respectively. The ^{55}Fe source was placed as close as possible to the detector window, providing a counting rate of $44\,\mathrm{kHz/cm^2}$. 120 consecutive acquisitions of 10 seconds each were made (over 20 minutes). After this, the irradiation was suspended, but the MHSP was kept biased. The procedure was repeated three more times, as shown in fig. 2.5(a). It shows the signal amplitude and energy resolution obtained as a function of the time elapsed from the beginning of each set of 20 minutes. The time of the day at which each test started is shown in the graph and the x-axis shows the elapsed time in seconds. The charge gain at the beginning of each set was higher and during the first 5 minutes dropped around 4 %, to a constant value. This behaviour is consistent over the four sets of measurements and is related to an up-charging of the MHSP. The positive ions on the surface of the MHSP's substrate do not move away fast enough, shielding the electric fields applied to the MHSP. This reduces slightly the gain. The energy resolution is poorer due to the high rate, but constant over time, and the charge gain remains constant after equilibrium has been achieved.

After these measurements, the detector was kept irradiated at a lower rate ($10\,\mathrm{kHz/cm^2}$) during two more hours before the beginning of the data acquisition of fig. 2.5(b), which lasted 20 minutes. The charge gain was stable over the measurements, decreasing

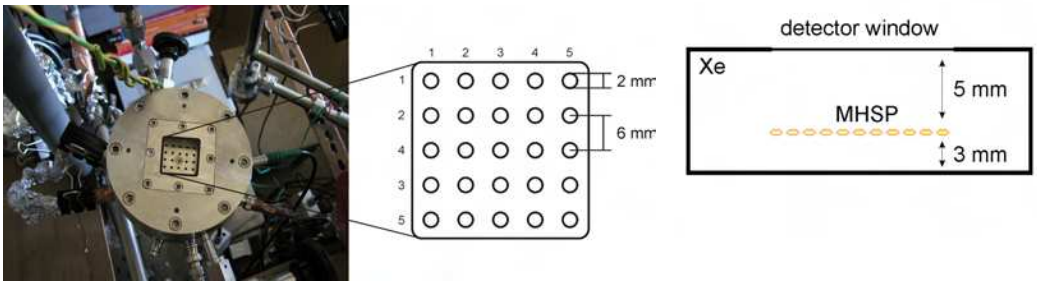

(a) (b)

Figure 2.2: The detector used to characterise the standard MHSP. (a) The window consists of a 5×5 array of 2 mm collimators with a pitch of 6 mm. (b) Diagram of the detector layout. The drift region was 5 mm deep and the MHSP was placed at 3 mm from the grounded detector body.

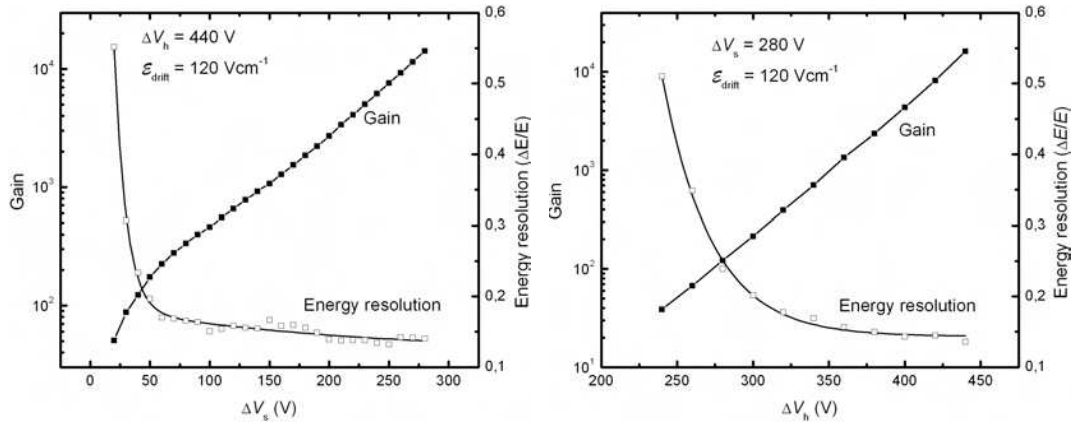

(a) (b)

Figure 2.3: MHSP gain and energy resolution for 5.9 keV X-rays as a function of: (a) ΔV_s, for $\Delta V_h = 440$ V; (b) ΔV_h, for $\Delta V_s = 280$ V. Operation in pure xenon at 1 atm.

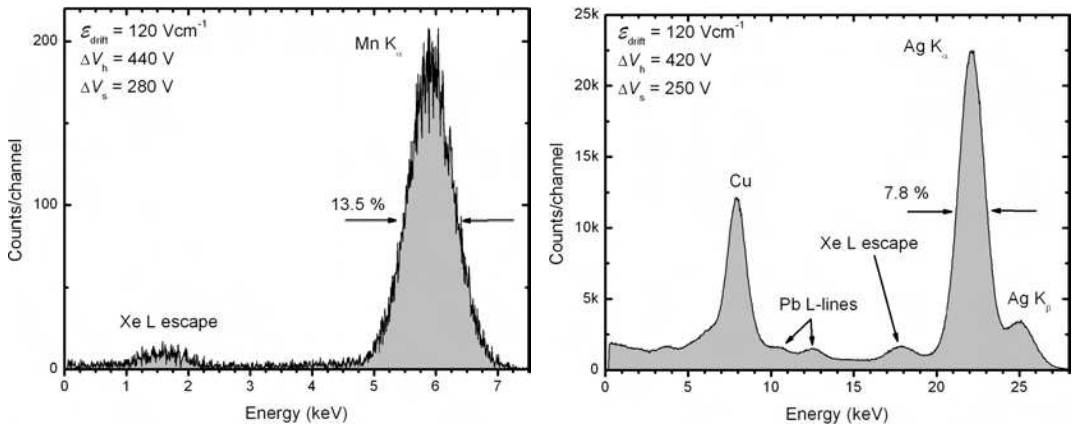

(a) (b)

Figure 2.4: Typical pulse-height distributions for 5.9 keV X-rays from a ^{55}Fe radioactive source (a) and 22.1 keV from ^{109}Cd X-rays (b) obtained with the MHSP, operating in pure xenon at 1 atm at charge gains of the order of 10^4 and 5×10^3, respectively.

0.004 channels per second. This is not due to the MHSP, but to the degradation of the gas purity originated by the out-gassing of the detector materials. The resolution improved due to an effective removal of the positive ions from the surface of the Kapton™ foil and kept a constant value around 13.9 %, with a high scattering because the spectra, with only 10 s acquisition time, had a low statistical quality.

The gain uniformity of a typical standard MHSP over 25 different spots was studied, making use of the 5×5 colimator matrix applied to the detector window. Figure 2.6

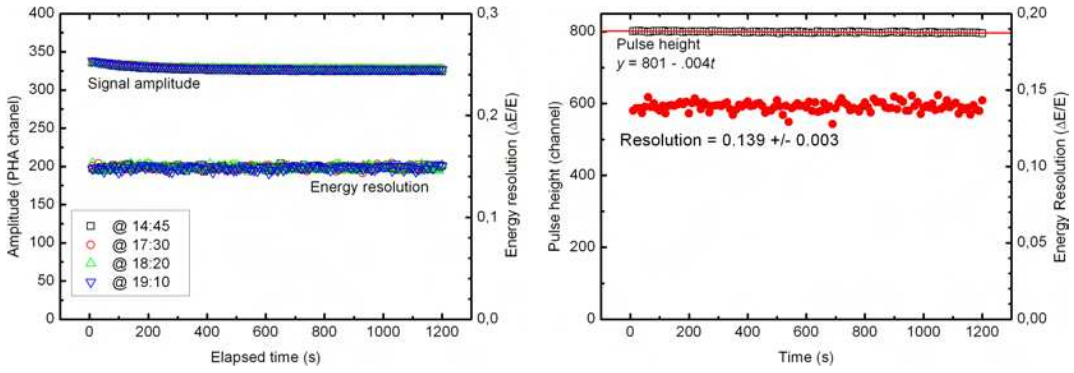

(a) (b)

Figure 2.5: (a) Four sets of 120 consecutive measurements of 10 s at a counting rate of 44 $^{kHz}/_{cm^2}$. The detector takes some minutes to reach equilibrium due to up-charging effects, but then the charge gain stabilises over a long time. (b) After several hours of irradiation, the main peak drifted 0.004 channels per second due to the out-gassing of the detector materials and not due to MHSP instability. The energy resolution improves when compared to the high rate cases and does not change over the 20 minutes of acquisition.

shows the gain distribution over the holes in the window. It is obvious from the contour projection at the bottom of the graph that the MHSP was not aligned with the detector window. In fact, there was a mistake when closing the detector and the MHSP was rotated accidentally by 45° with respect to the window. Nevertheless, it was noticed that the gain was uniform over the whole area of the MHSP, within a standard deviation of 5 %, taking into account only the 21 points where the MHSP was hit by the X-rays. This nonuniformity is mainly related to small differences in the diameter of the holes in the MHSP. The nonuniformity due to anode strips with different widths seems negligible, since there is no trend of gain changing along one specific direction, as it would be expected if the anode strips were thinner in some region of the MHSP.

The amplitude ratio between the signals collected from the anode strips and from the top electrode is shown in fig. 2.7(a). The signals read from the GEM-electrode of the MHSP are inverted and have an amplitude of typically 35 % of those from the anode strips. Figure 2.7(b) shows that the signals collected from the GEM-electrode occur at the same time as those collected from the anode strips. This confirms that the signals at the top are not originated by the back-flow of positive ions. They are induced by the charge on the anode strips across the Kapton™ substrate. The MHSP acts as a capacitor, with the Kapton™ working as the dielectric material.

Finally, the pulse rise time was measured as a function of the resistance "felt" by the charge signal. For this, different resistors were introduced between the MHSP and the charge pre-amplifier. As shown in fig. 2.8, the pulse rise time increases considerably with the resistance. This fact must be taken into account when selecting the values

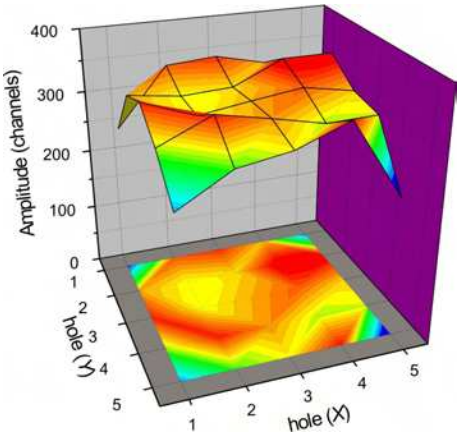

Figure 2.6: The pulse amplitude distribution over the whole area of the MHSP. The MHSP is rotated 45° relative to the detector window. The standard deviation of the amplitude distribution is less than 5 %.

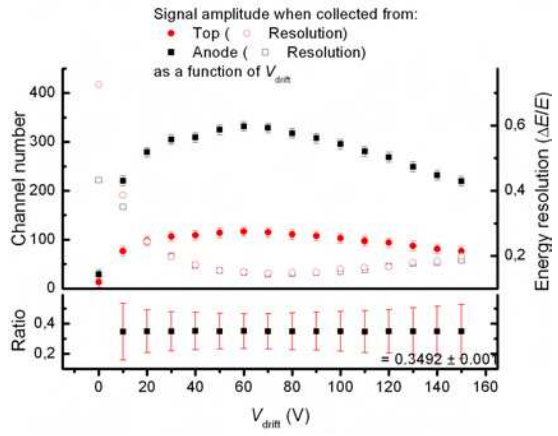

(a)

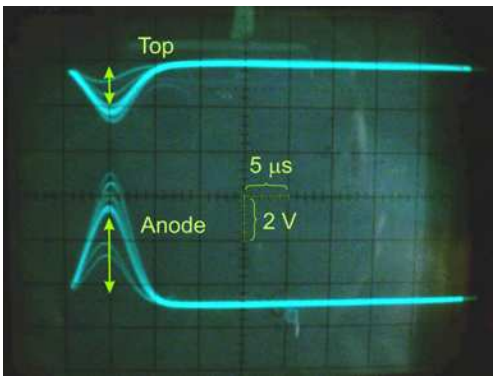

(b)

Figure 2.7: (a) When the charge signals are measured from the GEM-electrode of the MHSP, their amplitude is 35 % of the amplitude of the signals directly read from the anode strips. (b) The signals read from the top electrode have a lower amplitude, but the shape and the time of occurrence are similar, confirming that they are induced by the signals at the anode due, to the capacitance of the MHSP.

for the resistive strips to apply, for position sensitivity. The rise time of the pulses collected from the GEM electrode is higher due to the capacitance of the MHSP.

2.2 The principle of imaging with the MHSP

As mentioned in the last chapter, the MHSP has an intrinsic 2D-imaging capability. Some simple changes in the structure layout allow this device to provide position information of each X-ray photon detected. In fact, if all the anode strips are made independent on one side, one of the position coordinates can be determined by deter-

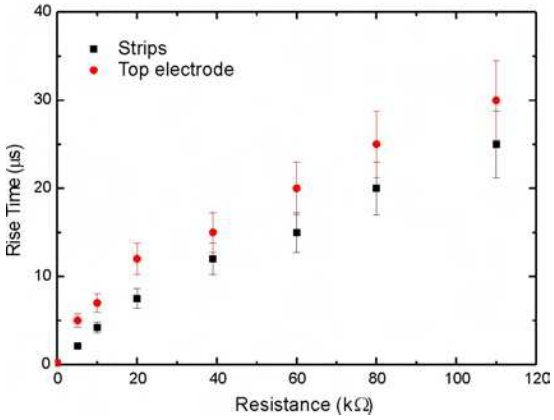

Figure 2.8: The pulse rise time as a function of the resistance placed between the MHSP and the charge pre-amplifier. The rise time increases with the resistance.

mining the centroid of the charge distributed over a few anode strips. On the other hand, if the opposite side is segmented in independent strips, perpendicular to the anode strips, the other position coordinate can be obtained.

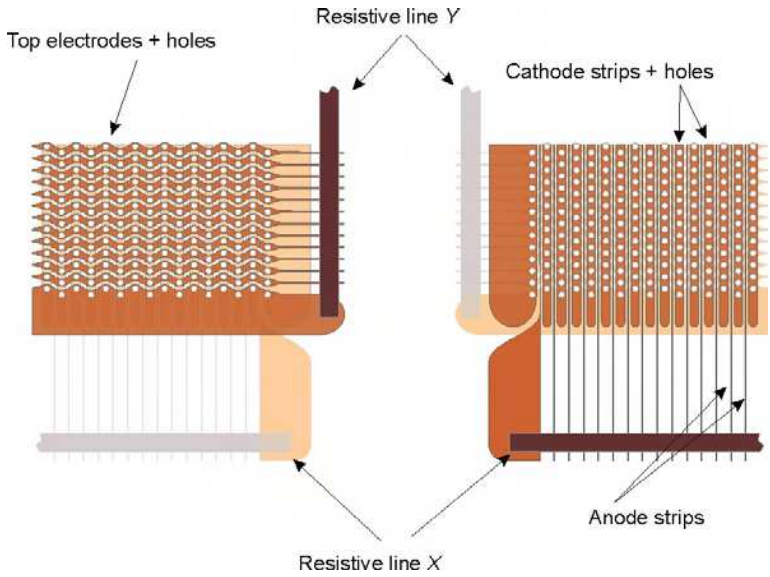

Figure 2.9: The concept of 2D-MHSP. (*left*) The GEM-electrode is segmented in independent strips with a *zigzag* shape to involve the holes. These strips are then interconnected with a resistive strip. (*right*) On the MS-side, the anode strips are made independent and are also interconnected with another resistive strip, to provide the second position coordinate.

The left side of fig. 2.9 shows how the top side of the MHSP must be segmented in strips. The *zigzag*-shape is needed to create the electric field around the holes, while

keeping the strips perpendicular to the strips on the opposite side (right). A resistive strip is applied interconnecting all the strips. By flipping vertically, the right side of the figure is obtained, showing the MS-side of the MHSP, with independent anode strips, also interconnected by a resistive strip, perpendicular to that on the top (*zigzag*) side.

By collecting the signals from both ends of each resistive strip, it is possible to determine the centroid of the primary electron cloud and plot a 2D-histogram corresponding to the image, using the following equation:

$$x = l\frac{X_{\mathrm{L}} - X_{\mathrm{R}}}{X_{\mathrm{L}} + X_{\mathrm{R}}} \tag{2.2}$$

x: coordinate of interaction
l: length of the resistive strip
X_{L}: signal amplitude from one of the edges of the resistive strip
X_{R}: signal amplitude from the other edge of the resistive strip

For the y-coordinate the formula is the same. All this can be done using only 4 amplification and shaping channels, as illustrated in fig. 2.10

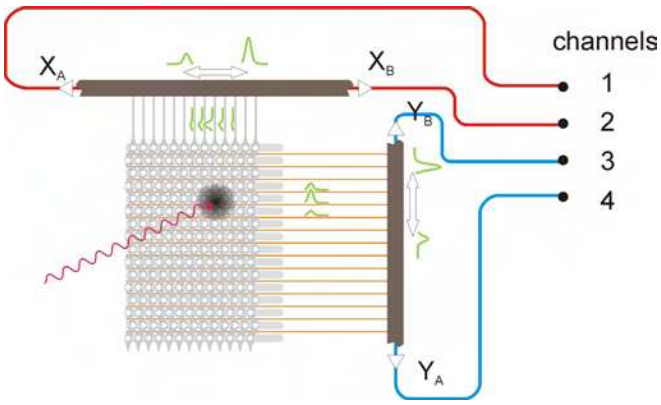

Figure 2.10: The use of resistive strips allows imaging, using only four electronic channels.

A coincidence circuit collecting signals can provide a vector for each event (x, y, E), where x and y are the coordinates of the charge centroid and E the X-ray energy. Ideally, each pixel in the final image contains a full energy spectrum and, conversely, each region of an energy spectrum can be associated to a image of X-ray photons within that energy region. This makes the 2D-MHSP a quantum particle detector, since it retains the information of each particle entering the detector.

2.2.1 Proof of principle

With the principle of resistive charge division for the imaging-MHSP in mind, some studies were made, prior to the manufacturing of the final device, in order to test if

it actually works, what problems can be found and what are the best values for the resistive strip.

The resistive strips were reproduced using resistor chains. By introducing charge signals in different points of the resistor chain, it was possible to divide them and measure the charge at both ends. Figure 2.11 shows the experimental setup for these measurements. The higher resistances were used for a coarse selection of one region in a hypothetical resistive strip and the smaller resistances ($r \approx R/200$) provided a finer selection. To reproduce the measurements across different coarse regions, five possible combinations of resistors were available. Within each of these combinations, a finer selection of resistors allowed reproducing individual anode strips. This was done using a *sub-chain* of six resistances with the value r. The regions are in the vicinity of 0.17, 0.25, 0.50, 0.75 and 0.83 of the total active length of the *virtual MHSP*.

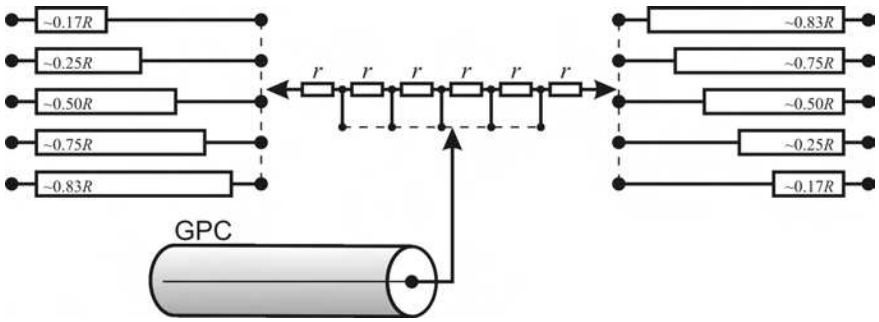

Figure 2.11: The gas proportional counter and the resistor chain. For given R it is possible to simulate five different coarse regions of the MHSP. Changing r allows to simulate single anode strips within one region.

Pulse height analysis was made using the charge signals from a standard gas proportional counter (GPC). The two expected peaks were obtained, and their amplitudes were related to each other through equation 2.2 (l was arbitrarily set to unit, for simplicity). The expected values of the position were simply proportional to the fraction of the total resistance "felt" by the GPC, thus calculated through equation 2.3.

$$x \propto \frac{R_{\mathrm{L}}}{R} \tag{2.3}$$

x: expected value for the position
R_{L}: resistance until the input point
R: total resistance of the chain

This resistor circuit is a good analogy to the case where an actual resistive strip is used. In fact, with resistive lines, the use of resistance units is equivalent to length. Therefore, the method of resistive charge division is nothing but measuring resistances.

Several resistor chains were used with values of R ranging from 10.5 kΩ to 148.7 kΩ. The charge pulses were obtained by irradiating a proportional counter from Metorex™ (type 2460Ar), filled with argon at a pressure of 6 bar, with an ^{55}Fe source. For

the measurements, two Canberra 2006 charge preamplifiers, and two Tenelec™ TC243 shaping amplifiers (2 µs shaping time) have been used[2]. The energy resolution obtained for the GPC was 14.6 % for the K_α lines of the ^{55}Fe source (5.9 keV), a little worse than the 13.5 % obtained using the charge preamplifier recommended by the manufacturer (Metorex™ MCPS 2194).

The fine gain of the shaping amplifiers was adjusted in order that the two peaks corresponding to the middle of the resistor chain had the same amplitude. Figure 2.12(a) is a plot of the measured values as a function of the expected. As the difference between both sides of the chain increases (the borders), slight distortions start to occur. These distortions are more evident as the total resistance increases, and start to be critical above 40 kΩ. In fig. 2.12(b), the sum of the amplitudes at both ends of each resistor chain, for the different values of total resistance is plotted as a function of the position in the resistor chain.

It is easy to conclude from this data that for higher resistances, there will be some distortion of the final image at the edges. The result is a compression of the distances near the edges of the image, resembling a pincushion distortion in optical lenses with aberrations.

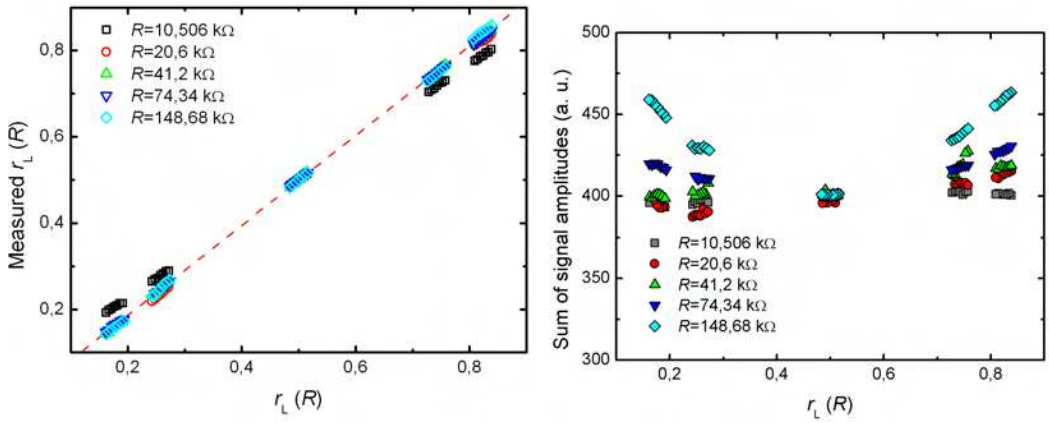

(a) (b)

Figure 2.12: (a) A plot of the measured resistance as a function of the actual resistance between the GPC output and one of the charge preamplifiers. The red line serves to guide the eye. (b) The sum of the amplitudes on both sides of the resistor chain as a function of the point within the chain. This enhances the distortions for points away from the centre. The data is plotted in units of the total resistance R.

[2]The Canberra™ 2006 charge preamplifier and the Tenelec™ TC243 shaping amplifier are used as a standard in our labs. Therefore, if not otherwise stated, when the electronic components are mentioned it is assumed that these are the models used.

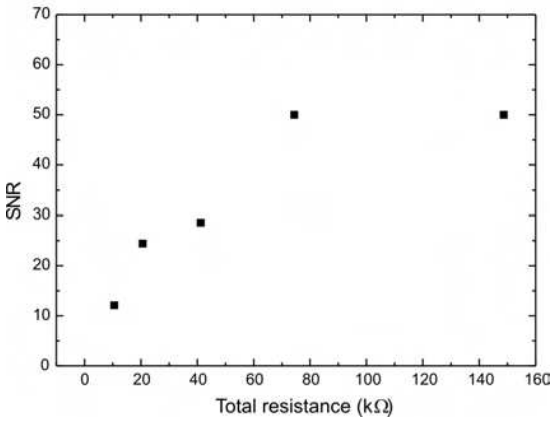

Figure 2.13: The signal-to-noise ratio as a function of the total resistance of the resistor chain. It is shown that the SNR tends to increase with the total resistance, saturating above 80 kΩ.

2.3 Image quality—limitations and concepts

The graphic from fig. 2.13 shows how the signal-to-noise ratio (SNR) varies according to the value of the total resistance of the resistor chain. The value taken for the noise amplitude was its FWHM, considering the centroid at channel zero in the pulse height analyser. The SNR increases and seems to saturate above a certain resistance. This suggests that it is desirable to have a high total resistance for higher SNR, hence position resolution.

The drawback is that for higher resistances the rise time of the signal increases as shown in fig. 2.8 on page 32. The high frequency part of the signal is attenuated for high resistances, which means that it becomes much slower, reducing the high rate capability of the imaging system. This acquires higher importance for positions far away from the central point, because the difference of resistances will be higher, meaning that the signal covering a higher distance/resistance is slower than its pair. This means that a longer time is needed to collect both signals. At least for the first studies, it might be a good idea to have signals as fast as possible, to avoid difficulties of processing all the four signals corresponding to an event.

Another aspect to be taken into account is that the experimental measurements show that distortion also increases for higher resistance. Even with the perspective of off-line image corrections, the high distortions of the image at the borders might considerably affect the usefulness of an image.

The attempt to increase the signal-to-noise ratio simply by increasing the resistance is not wise. A compromise has to be found, choosing a resistance low enough to provide good counting rates while high enough to keep a good SNR, and a careful study on this matter is important. Keeping this limitation in mind, it is also important to analyse other limitations to the position resolution, such as the range of the photoelectrons generated when acquiring X-ray images. Useful concepts for characterisation of the

image quality are also shortly described at the end of this section.

2.3.1 The signal-to-noise ratio

Reference [26] makes a theoretical exposition of how the position resolution improves as the total resistance and signal-to-noise ratio increase. This simple model can help to estimate the position resolution possible to obtain as a function of the signal-to-noise ratio, with the method of resistive charge division. Taking into account the input impedance Z of the preamplifiers at each end of a resistive strip, assuming they are equivalent, the ratio between the charge arriving at each end (Q_{L} and Q_{R}) is the inverse of the ratio between the resistances crossed by each charge pulse:

$$\frac{Q_{\mathrm{L}}}{Q_{\mathrm{R}}} = \frac{(l/2 - x)\,\rho/A + Z}{(l/2 + x)\,\rho/A + Z} \tag{2.4}$$

where x is the distance from the original pulse to the centre of the resistive strip with length l, cross sectional area A and resistivity ρ. The position can then be given by:

$$x = \frac{l}{2}\left(1 + \frac{2Z}{R}\right)\left(\frac{Q_{\mathrm{R}} - Q_{\mathrm{L}}}{Q_{\mathrm{R}} + Q_{\mathrm{L}}}\right) \tag{2.5}$$

This equation corresponds to equation 2.2, now taking into account the input impedance of the preamplifiers. The position resolution can be seen as the standard deviation of the position. To evaluate how it is influenced by the noise of the system, a simple error propagation study can be made:

$$(\sigma_x)^2 = \left(\frac{\partial x}{\partial Q_{\mathrm{R}}}\sigma_{Q_{\mathrm{R}}}\right)^2 + \left(\frac{\partial x}{\partial Q_{\mathrm{L}}}\sigma_{Q_{\mathrm{L}}}\right)^2$$

It is assumed that the equivalent noise charges are equal and independent, $\sigma_Q = \sigma_{Q_{\mathrm{R}}} = \sigma_{Q_{\mathrm{L}}}$, which gives:

$$\sigma_x = l\left(1 + \frac{2Z}{R}\right)\frac{\sqrt{Q_{\mathrm{R}}^2 + Q_{\mathrm{L}}^2}}{(Q_{\mathrm{R}} + Q_{\mathrm{L}})^2}\,\sigma_Q \tag{2.6}$$

For signals at the centre of the resistive strip, $Q_{\mathrm{R}} = Q_{\mathrm{L}} = Q$ is the signal and σ_Q is the noise, therefore, equation 2.6 can be rewritten as

$$\sigma_x = \frac{l}{2\sqrt{2}}\left(1 + \frac{2Z}{R}\right)\frac{N}{S} \tag{2.7}$$

confirming that the position resolution improves for higher resistance and for higher signal-to-noise ratio.

2.3.2 Photoelectron range

When an X-ray with an energy of the order of those used in this work (in the range of 3–30 keV) hits a xenon atom, a photoelectron is removed from a shell with a binding energy lower than the photon energy and the energy difference is converted to kinetic energy of the photoelectron. Since, in the specific case of xenon, mostly electrons from the L-shell are removed (L-shell binding energies $E_{L_1} = 5.5\,\text{keV}$, $E_{L_2} = 5.1\,\text{keV}$ and $E_{L_3} = 4.8\,\text{keV}$), the kinetic energy of the photoelectron is $E_{phe} = E_x - E_L$, where E_{phe} and E_x are the energies of the photoelectron and the X-ray, respectively.

The atom is left in an excited state because there is an empty place left by the photoelectron. The atom returns to the fundamental state when an electron from an outer shell occupies this place and the excess of energy is released either by emitting a fluorescence X-ray or—more probably for the L-shell—by emitting an Auger electron. In any case, the energy of the fluorescence X-ray or the Auger electron is given by $E_L - E_M \approx 3.6\,\text{keV}$, where the indices denote the L- and M-shells. The range of both the photoelectron and the Auger electron in xenon introduce an uncertainty in the position where the interaction occurred and determine the best position resolution achievable with this gas. References [15, 16] describe a study of the best resolution achievable in xenon, methane and ethane. It was noticed that, at the pressure of 1 bar, the best resolution achievable in xenon is around 60 µm, for incident X-ray photons with an energy of 8 keV. Figure 2.14 shows the results obtained in the references for the position resolution obtained for xenon as a function of the incident X-ray energy.

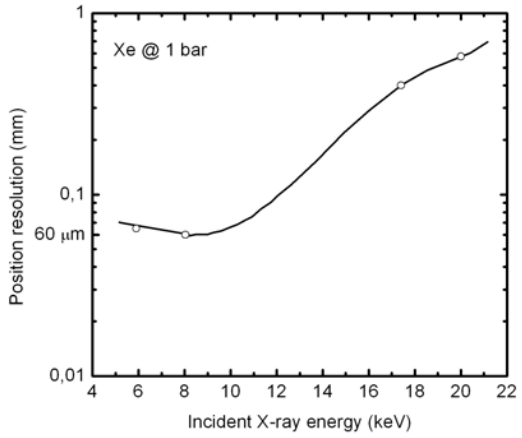

Figure 2.14: The best resolution achieved in xenon at 1 bar as a function of the incident X-ray energy. Data from [16]. The minimum around 60 µm occurs when the photoelectrons have the same energy of the Auger electrons.

For X-ray energies below 8 keV, the Auger electron has a higher fraction of the energy and the position resolution improves slowly as the energy increases. When the distribution of energy between the two electrons becomes even, the position resolution reaches a minimum value of 65 µm. For higher energies it increases rapidly and, when the energy of the photoelectron is much higher than the energy of the Auger electron,

the curve approaches a power function, suggesting a behaviour similar to that of organic gases. The position resolution is better than the range of the electrons because the energy loss is higher at the beginning of the electron track [57]. The position resolution gets worse as the X-ray energy increases, but when it becomes higher than the K-edge, the energy of the photoelectron is again low enough to provide good position resolution [58].

In CF_4, the energy of the X-ray is transferred almost totally to the photoelectron. The binding energy of the K-electrons of fluorine and carbon are 0.69- and 0.28 keV, respectively, which means that the photoelectrons are much more energetic than those generated by interactions with xenon. This has a consequence of a much higher range leading to a poorer position resolution with X-rays. The photoelectron range, as in hydrocarbon gases, is expected to be proportional to $E^{1.75}$ (E is the X-ray energy). However, to infer about the position resolution when using this gas, the comparison with hydrocarbon gases is insufficient. For these gases, the ionisation is approximately constant over the whole electron path, which means that the position resolution is approximately equal to the electron range in the gas. In CF_4, a heavier molecule, with much more electrons than methane or ethane, it is expected that more energy is absorbed at the beginning of the electron track, meaning that the centroid of the primary electron cloud is closer to the interaction point. This issue will be addressed in chapter 4, based on experimental data.

2.3.3 Some concepts on imaging

At this point it is important to make a short review of the concepts involved in what concerns image characterisation such as position resolution, uniformity, dynamic range, among others. The quality of an imaging system must be quantified, in order to compare different systems and to evaluate their performance. Terms such as position resolution are vague and very often attached to other concepts, which make them relative. This subsection is intended to be a short summary providing further understanding of the motivation of the measurements done. It is not supposed to be a profound analysis of this matter, since there is abundant literature on it [59–61]. The position resolution does not determine the minimum size of the objects that can be visualised in an image. In reality, what determines if objects can be distinguished or not is much more complex and is related to the contrast of the image and distortion, besides their size.

Dynamic range

Images are colour or grey scale intensity maps. In an intensity map, the *dynamic range* corresponds to the number of intensity levels composing it. The number of shades of grey or colours that the human eye can distinguish is limited, but if some image has a high *dynamic range*, it is possible to manipulate the distribution of the shades of grey or colours to make it possible to distinguish features among objects with low contrast, disregarding less interesting features. In imaging systems it is important to

have the highest possible *dynamic range*. In most of the times, this has the cost of a high radiation dose, which implies some kind of compromise.

Point spread function

In real world imaging systems it is impossible to obtain perfect, infinitely sharp images. When two infinitely small holes in an opaque medium are illuminated, their image is a 2D intensity distribution of the photons which passed through the holes and hit the imaging system. In the ideal case, the profile of the intensity map would correspond to two delta functions. However, this is not the case, since the delta functions have rounded corners, due to the *point spread function* (PSF) of the imaging system. The width of the intensity profile is an indicator of the position resolution. In fact, if the two points are gradually brought together, the two PSFs will start to overlap and, at some distance, the two points will become indistinguishable. This distance is usually used to quantify the position resolution of the system.

Line spread function

The PSF has, however the inconvenience of being impossible to represent in the real world, since there is no such thing as a dimensionless hole. The approximation of small holes is usually impractical, since the counting rate becomes very low for small irradiated areas. Because of this, lines are usually preferred to points. The image of a thin slit is composed of all the PSFs along its direction. If the several PSFs are integrated along this direction, the *line spread function* (LSF) is obtained. If the imaging system is uniform and isotropic, the LSF should be a convolution of a delta function corresponding to the rectangular slit, with a Gaussian curve corresponding to the PSF. As the width of the slit decreases, the Gaussian shape in the convolution becomes more pronounced. The width of the image decreases until it reaches the width of the PSF. This value is also often used as the position resolution for the coordinate perpendicular to the slit's direction. It is possible to deconvolute the Gaussian curve for slits with finite width. Reference [62] has a very interesting discussion on this, deriving an empirical equation to determine the position resolution using a slit. Basically, if the slit has a width of the order of the resolution of the system, then, its resolution is given by

$$\sigma_x = w_\mathrm{o} \times \sqrt[3]{\left(\frac{w_\mathrm{i}}{w_\mathrm{o}}\right)^3 - 1} \tag{2.8}$$

where w_i is the width of the image and w_o is the width of the slit (object). For cases where the objects are so small that the image results in a distribution much larger than the object, the position resolution is approximately the width of the image ($\lim_{w_\mathrm{i}\to\infty} \sigma_x = w_\mathrm{i}$, valid for $w_\mathrm{i} \gtrsim 3w_\mathrm{o}$).

Edge spread function

Other alternative to imaging a slit for determining the spatial resolution, is imaging a sharp edge and obtain the *edge spread function* (ESF), integrating its profile along its direction, in the same way the LSF was obtained. The intensity distribution for an ideally resolved edge should be a step function, with zero intensity where the detector window is covered, and maximum intensity in the illuminated area. Once again, due to the finite spatial resolution, the step becomes smoothed, and this can be used to determine the spatial resolution of the imaging system. By differentiating the ESF, the PSF is obtained, and its width is the spatial resolution of the imaging system.

Modulation transfer function

The response of the imaging system is, however, not complete by finding its LSF for a given thin slit or ESF for an edge. For example, if two slits of different widths are imaged, the intensity obtained for the thinner slit is lower than for the wider. This is again related to the PSF, and means that smaller objects have lower contrast than larger objects.

It is important, therefore to define another concept which gives a quantitative description of the system's response as a function of the size of objects or—even better—as a function of the spatial frequencies involved. The spatial frequencies are defined in line pairs per millimetre—$^{\mathrm{lp}}/_{\mathrm{mm}}$. One way to quantify the contrast (*modulation*) is to chose two different regions within an image with known spatial frequencies ν, and relate their intensities:

$$C(\nu) = \frac{I' - I}{I'}. \tag{2.9}$$

An example of an object containing only one spatial frequency can be imagined as a sequence of equally spaced slits, with a pitch of two times their width. One of the *lines* is the slit and the other is the opaque material and each of these pairs is a period. When different sets of slits with different spatial frequencies are imaged, the contrast of the slit profiles decreases with increasing spatial frequency. If this contrast is plotted as a function of the spatial frequency, the *modulation transfer function* (MTF) is obtained. This function describes how the imaging system behaves in the spatial frequency domain. It describes how the image contrast varies with the size of the objects imaged. For that reason, the MTF is also called *contrast transfer function* (CTF) and can be directly measured with special masks composed of sets of slits with different widths; or calculated through the *fourier transform* (FT) of the LSF. The full width at half maximum (FWHM) of the LSF of a thin slit could roughly be approximated to the number of line pairs per millimetre at 3 % of the maximum amplitude of the MTF, along this work.

Integral nonlinearity

After the imaging system is characterised in terms of spatial resolution and contrast response with spatial frequency, it is also important to know how the image distorts the

object. In the ideal case, the distances in the image are proportional to the distances in the object. However, in real systems, the proportionality constant is not the same throughout the area of the image. This is mostly due to nonuniformities in the detector manufacturing. Nonuniformities are a source of errors while estimating the size of features in the image. To measure this non-ideal characteristic, some mask with known dimensions is imaged—for example, an equally distanced series of slits or pinholes—and the position of each pinhole in the image is plotted as a function of the real position in the object. The distribution of the measured position as a function of the real position is close to a straight line. By fitting the linear distribution obtained, the average of the distance between each point and the straight line is the *integral nonlinearity* (INL) of the imaging system.

Finally, in any X-ray imaging system, a pulse height analysis has to be done, using ADCs. This means that somewhere in the electronic chain the signal is digitised. Whenever an analog amplitude is converted to a digital (discrete) quantity, according to the number of bits of the ADC, the amplitude of the signal is approximated to the nearest bit. This implies that a range of amplitudes smaller than the ADC's resolution, has the same value after digitised. Therefore, since the position is calculated using the pulse height, some positions will be too close and will fall within the same pixel. The *differential nonlinearity* (DNL) of the imaging system gives the minimum distance for two points to fall in the same pixel. The DNL will not be treated into detail in this work because the 'worst case scenario' ADC had 1024 channels, which corresponds to a pixel size of $25\,\mu m^2$ in a $25 \times 25\,mm^2$ field of view. This is much less than the resolution expected to obtain in the preliminary studies carried out in this work. At the end, 32 k-channel ADCs were used, allowing pixel size down to less than $1\,\mu m^2$. The position resolution was not limited by the resolution of the ADCs used.

2.4 1D-imaging—analog *versus* digital

In the imaging-MHSPs produced for this work, the dimensions of the holes and strips as well as the thickness of the substrate and copper layers were maintained. The difference was, as described in section 2.2, the interconnection of the anode strips through a resistive strip, and the new strips pattern with a *zigzag* shape in the GEM side, also interconnected by a resistive strip.

Figure 2.15 is a picture of both sides of a typical MHSP, where the resistive strips and the *zigzags* on the GEM side are clearly visible. The pictures were taken in such an orientation that the resistive strips appear horizontal at the bottom, however it should be reminded that they are perpendicular to each other.

The resistive strips were designed with a total resistance between 10– and 20 kΩ. This range provided pulses with a rise time below 10 µs and, for a resistance of 20 kΩ, the SNR for 5.9 keV was 25 (FWHM, see fig. 2.13). With a 28 mm long resistive strip and using charge preamplifiers with an input impedance of $Z = 100\,\Omega$, from eq. 2.7, the position resolution is expected to be $\sigma_x = 0.180$ mm (0,43 mm FWHM), well under 1 mm, as proposed in this work. Some further discussion on the practical consequences

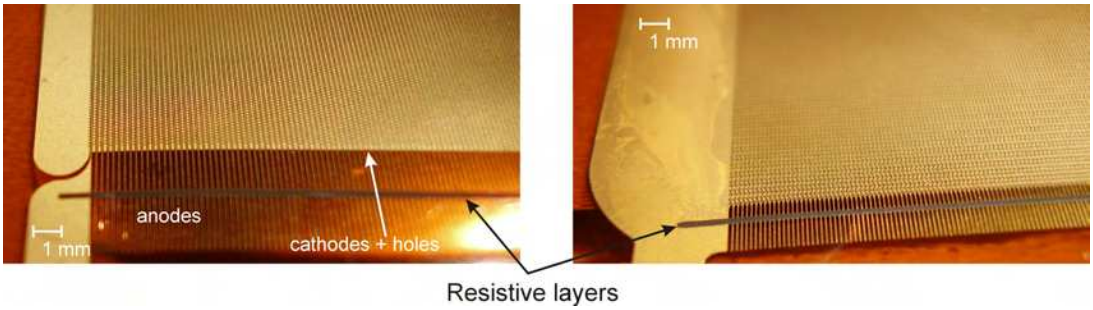

Figure 2.15: Both sides of the 2D-MHSP, where the resistive strips are visible. The GEM-side, on the right, is structured in *zigzag*-shaped strips.

of what was described here will be carried out in the next chapters as the experimental results of the imaging detector are discussed. The resistive strip had a width of 200 µm and length of 28 mm, with a total resistance of $\sim 15\,\mathrm{k}\Omega$, for a sheet resistance of around $100\,\Omega/\square$. A higher sheet resistance would imply reducing the thickness of the resistive strip, leading to higher nonuniformities, because it would be more difficult to keep a constant cross section over the whole length of the strip. Reducing the width of the strip would have the same effect.

The detector prototype used in this chapter (1D-readout) consisted on a simple adaptation of the system described in section 2.1. It had only four electrical connectors: two for biasing and signal collection from the resistive strips and two biasing inputs. As only one coordinate could be read at a time because there was no possibility to correlate both coordinates in time and only *line spread functions* (LSF) were obtained. Despite the impossibility of delivering 2D-images, it was possible to study the imaging capability of the MHSP when the charge was collected from either the anode strips or the GEM-electrode using analog and digital electronics.

For image collection the MHSP was biased with $\mathcal{E}_{\mathrm{drift}} = 200\,\mathrm{V/cm}$, $\Delta V_{\mathrm{h}} = 460\,\mathrm{V}$ and $\Delta V_{\mathrm{s}} = 260\,\mathrm{V}$. This corresponds to a gain of around $10^4 \pm 10\,\%$ when the charge is collected from the anode strips.

In the next subsection, the development of an analog computer to solve equation 2.2 is explained in detail as well as the results obtained. After that, subsection 2.4.2 explains how the same detector was used, with the signal sampled by a 200 MHz ADC, developed in the Electronics and Instrumentation Group (GEI) of the Physics Department in Coimbra. Results with the digitisation taking place before and after analog shaping of the signal are shown and compared with those obtained with the pure analog electronics.

2.4.1 Analog electronics

For the first studies of the imaging capability of the MHSP, a whole analog circuit was developed, having an analog signal multiplier/divider as the central component. Figure 2.16 shows a diagram of the division circuit, which worked as an analog computer, acquiring the two signals from both edges of a resistive strip and providing the result

of the division, as well as of the outputs for a coincidence circuit.

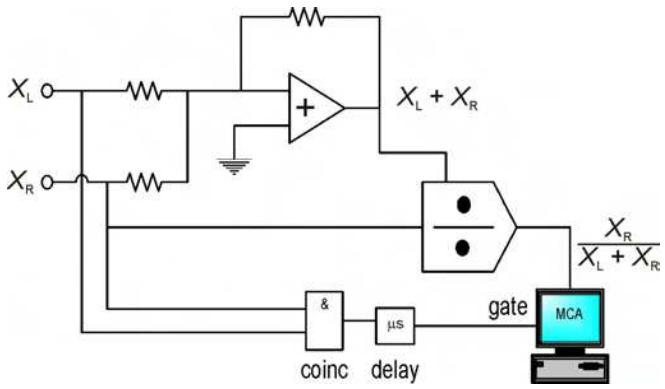

Figure 2.16: A diagram of the resistive charge division circuit. Inputs X_L and X_R are the outputs of the shaping amplifiers.

The AD734AQ 10 MHz, 4-quadrant analog multiplier/divider from Analog Devices™ [63] was used in this analog computer. The analog division is made in real time, which means that at each 100 ns the division between both inputs is being made. The consequence of this is that if the two pulses reach their maximum amplitudes at different times, the sum and the division are not accurate. That is why the signals from the shaping amplifiers were stretched with 1454 *Linear Gate and Strecher* NIM modules from Canberra™, providing square signals with height proportional to the amplitude of the Gaussian signals. It is as if the amplitudes were 'frozen' during a few microseconds. Both signals are then summed, using a standard operational amplifier (TL081IN from ST™) and then one of the pulses (X_R) is divided by the sum. With this circuit, the output of the divider is an amplitude between 0 and 10 V, proportional to the position, as in equation 2.2.

Since the divider performs the division in real time, in the absence of signals (a $\frac{0}{0}$ ambiguity) the output is a saturated voltage (around 10 V), corresponding to an *out of range* result. When one input is divided by the other, the output *drops* from this maximum value to a positive voltage. This poses a problem for the pulse height analyser (PHA): it is designed to sample pulses rising from 0 V to a positive voltage, and in this case, the pulse height to be measured is also referred to 0 V, but the pulse *falls* from 10 V, instead of *rising* from 0 V. The solution is to trigger the PHA acquisition with a coincidence circuit, connected to the PHA gate, which can be delayed to make sure the PHA reads the pulse in a flat zone, assuming that it rose from 0 V. Figure 2.17 describes the process of acquisition of one pulse, illustrating the stretched signals, the sum-signal, the division signal, the delayed TTL pulse used to open the PHA gate and the signal as read by the PHA.

For 2D-imaging purposes, a second circuit similar to this is needed. A further coincidence circuit allows correlating the pulses from both coordinates, which can be stored by a second PHA, synchronised with the first. In this section, only one analog computer was used, which means that only line spread functions were used to

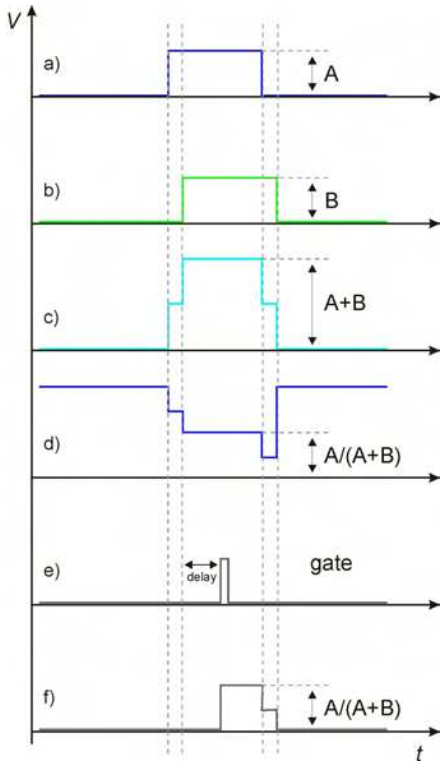

Figure 2.17: In order the PHA to recognise the signals arising from the divider, it is necessary to prepare them, using the PHA gate. a) and b) The stretched signals with an arbitrary (and overestimated) time difference. c) The summed signal. Due to the time difference, the shape of the signal suffers some change. d) The division originates a signal dropping from a maximum voltage, down to the correct value. The shape of the signal is also due to the time difference between both signals. e) The coincidence of a) and b) is used to generate a TTL pulse, which can be delayed and serves to open the gate of the PHA. f) when the gate is open, the PHA *sees* some signal amplitude, assuming that it rose from 0 V, as desired.

characterise its performance.

At a first stage, single rows (or columns, depending on the coordinate) of the 5×5 matrix of holes attached to the detector window were imaged. In order to minimise the effects of non-parallel X-photons from the ^{55}Fe radioactive source used in this section, it was placed as far as possible from the detector window. Since the source has a diameter of 0.5 cm, for a distance of 40 cm away from the detector window, the projection of a 2 mm hole on the MHSP surface, 0.5 cm away, has a circular 35 µm wide "penumbra". The activity of the radioactive source was not as high as desirable. Consequently, as the distance from the detector increased, the number of photons hitting the detector decreased and the background noise became important, reducing the contrast between the image and the background. The distance of 40 cm between the radioactive source and the detector window was a compromise between the counting rate and an optimal collimation of the X-ray beam.

The measurements were made for pulses collected from the resistive strip on the GEM side—defined as the y-coordinate—and then for pulses collected from the anode strips—the x-coordinate.

Charge collection from the GEM-electrode

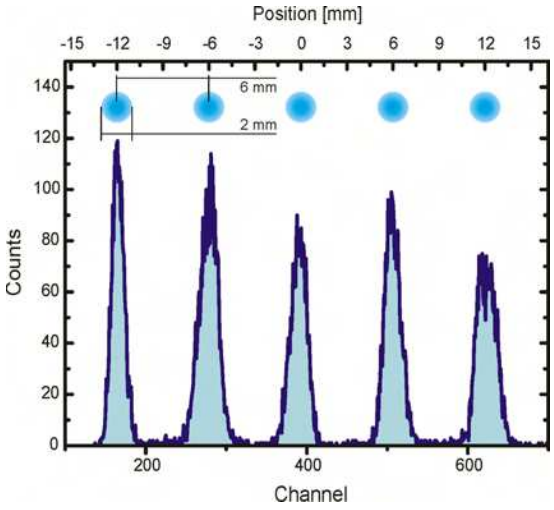

Figure 2.18: The line spread function of one column of holes measured with the charge collected from the top side of the MHSP. The scale of the holes is shown as blue/shaded circles above the peaks.

The amplitude of the pulses collected from this electrode is typically 35 % of that read from the strips, which means that, for the biasing voltages mentioned at the beginning of this section, the charge collected corresponds to a gain of 3500. Figure 2.18 shows the *line spread function* of a column of holes of the 5×5 collimator. The 2 mm holes, separated by 4 mm are represented in the figure as blue circles above the peaks. The peaks have the expected shape of LSFs calculated from circles, convoluted

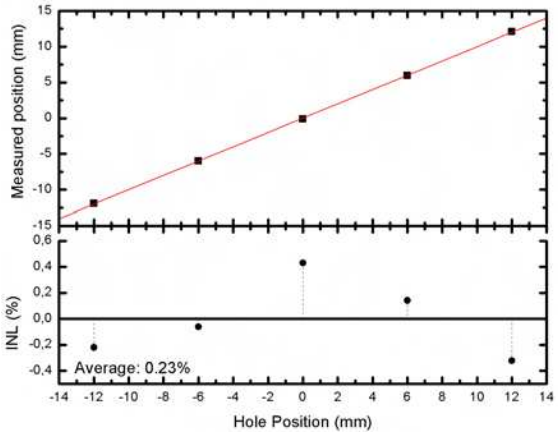

Figure 2.19: The measured position of the collimator holes as a function of their real position. The integral nonlinearity calculated for the five holes was 0.23 %.

with the bell-shaped curves of the system's PSF.

Since the peaks were symetric, they were fitted with Gaussian curves to determine their centroids and plotted as a function of the position of the holes. The plot can be seen in figure 2.19. The *integral nonlinearity* (INL) was found to be 64 µm. With respect to the full length of the resistive strip this corresponds to 0.23 %.

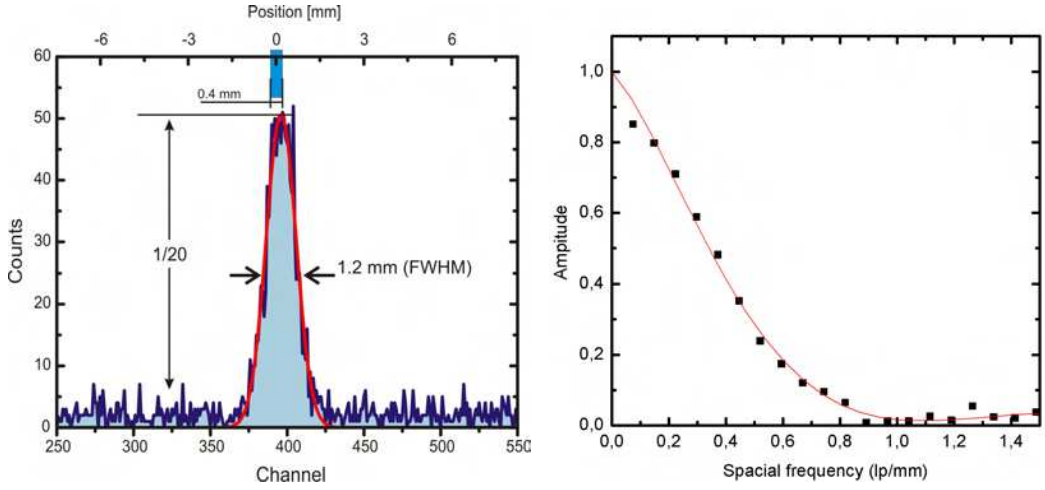

(a) (b)

Figure 2.20: (a) The LSF of a 400 µm slit and (b) its *Fourier Transform* — the MTF; signals collected from the GEM electrode of the MHSP. The width of the peak is 1.2 mm (FWHM), approximately equal to the position resolution. The MTF shows a resolution of 0.8 $^{\text{lp}}/_{\text{mm}}$ at an amplitude of 3 % of the MTF.

A 400 µm slit was also imaged and the distribution is shown in figure 2.20(a). The width of the Gaussian curve that fitted the peak was 1.2 mm (FWHM). There is no need of using equation 2.8 from page 40, since the distribution is much wider than the slit, which means that the resolution is given by the width of the peak, as discussed in page 40. The ratio between the background and the height of the peak is shown in the graph, with a value of 1/20. For smaller objects, the width of the distribution would be 1.2 mm, but the contrast would be smaller.

The *modulation transfer function* (MTF) is obtained calculating the *Fourier Transform* of the distribution of 2.20(a) as shown in (b). It is in agreement with the results found. The red curve is merely empirical, intended to guide the eye. The spatial frequency corresponding to 3 % of the MTF amplitude is around 0.8 line pairs per millimetre, leading to a minimum contrast for objects smaller than 1.25 mm. This confirms the relationship between the LSF and the MTF as described in section 2.3.3.

Charge collection from the anode strips

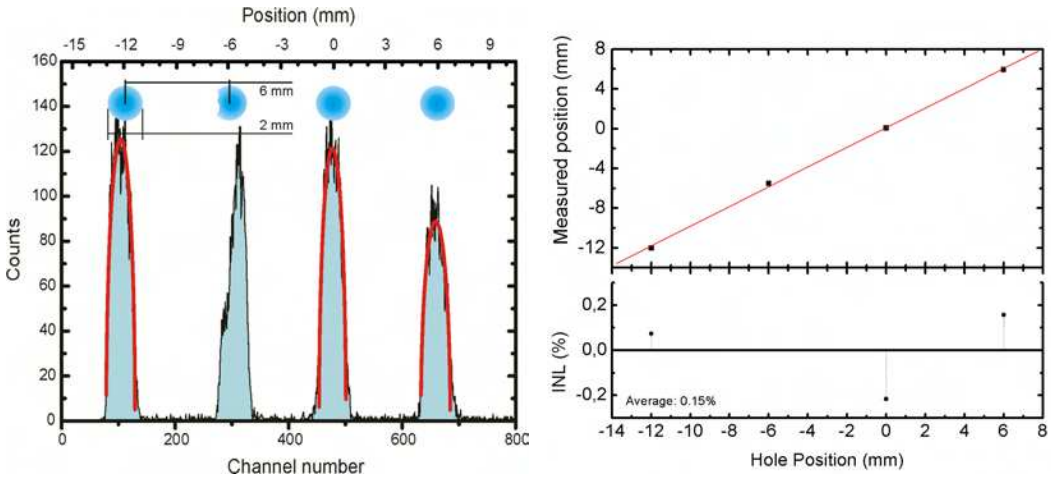

(a) (b)

Figure 2.21: (a) The line spread function of one row of four holes measured from the charge collected from the strips side of the MHSP. The holes are represented at the same scale as blue/shaded circles above the peaks. One of the holes was accidentally partially covered by epoxy and this is noticed in the distribution. (b) Three fitted peaks (explaination in the body text) were used to determine the *integral nonlinearity*, which was 41 µm — 0.15 % of the whole length of the MHSP.

When the charge pulses are collected from the anode strips—corresponding to the other position coordinate—the position resolution is expected to improve due to the higher signal-to-noise ratio. The detector was, therefore adapted to allow charge collection from the strips of the MHSP.

One single row of the 5×5 collimator matrix was imaged, with the ^{55}Fe radioactive

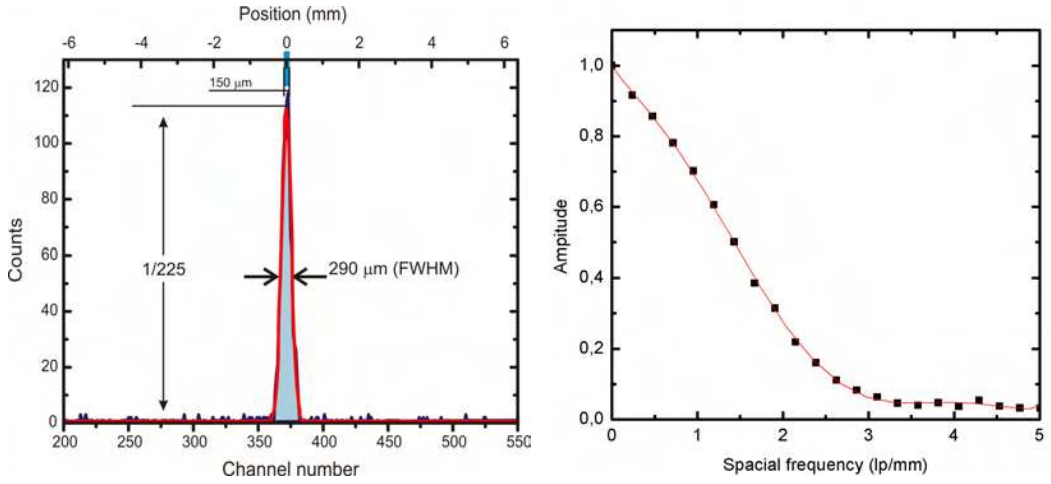

Figure 2.22: (a) The *line spread function* of a 150 µm slit and (b) its *modulation transfer function*; signals collected from the anode strips of the MHSP. The width of the peak is 290 mm. The position resolution from application of equation 2.8 is 276 µm. The MTF shows a resolution of 3.5 line pairs per millimetre at an amplitude of 3 % of the MTF.

source at a distance of 40 cm from the detector window. The same set of measurements was made for this situation. Figure 2.21(a), depicts the LSF distribution of four of the five holes of one row. The MHSP was not centred with the detector window therefore, the fifth hole is out of the sensitive area. One of the holes was partially covered with the epoxy used to seal the detector window during its manufacture and the consequences in the shape of the peak are clearly seen. Despite this, the distribution already reveals an improvement of the position resolution. The three *eligible* peaks have the expected shape of LSFs of circles showing that the influence of the detector PSF is much smaller than in the case of the pulses read from the GEM-electrode. The regions where no radiation hits the detector are sharply separated from the regions of the holes. These three peaks were fitted with circles to determine their centroids.

The position was calibrated and the measured positions were then plotted as a function of the position of the holes. The average distance between the measured hole positions and the linear fit — the INL — was 0.15 %, corresponding to 41 µm when the length of the resistive strip is taken into account.

To estimate the position resolution of the MSHP for charge pulses collected from the strips, a 150 µm thick slit was imaged. The distribution is shown in fig. 2.22(a) along with its MTF (b). The first aspect that catches the readers attention is certainly the increase of contrast between the slit and the background. Even for a much smaller object, the contrast with the background increases from $1/20$ in the case of a 400 µm slit with charge collection from the GEM electrode, to $1/225$. The width of this distribution is 290 µm, which is close to the size of the slit. Following the criteria used until now,

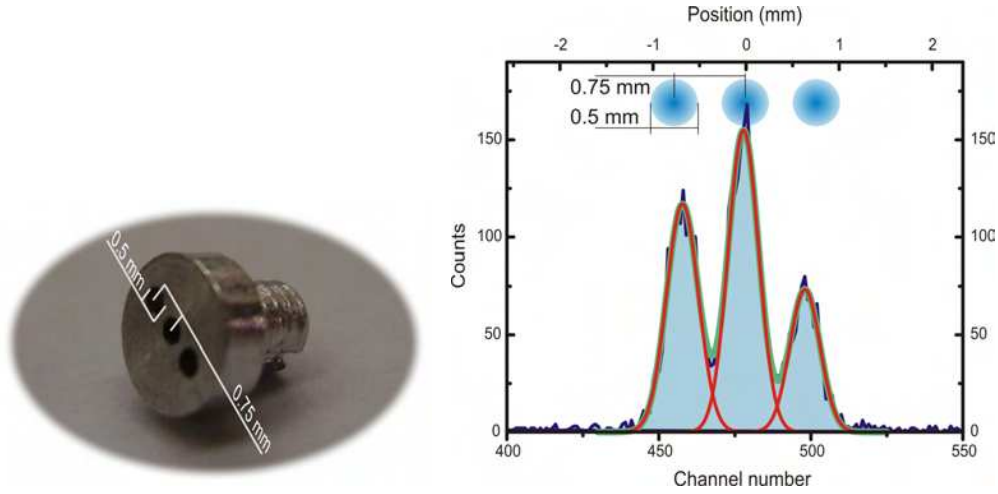

(a) (b)

Figure 2.23: (a) The aluminium collimator, specially designed to fit one of the 2 mm holes of the 5×5 collimator matrix. It has three 0.5 mm aligned holes with their centres at 0.75 mm from each other. (b) The three peaks are completely separated from each other, showing that it is already possible to image objects as small as 0.5 mm diameter holes. The space between the holes (corresponding to the valleys between the peaks) is 250 µm wide.

the position resolution obtained when equation 2.8 is applied, the position resolution is 276 µm (FWHM). The analysis of the MTF shows a resolution of 3.5 line pairs per millimetre at 3 % of the maximum amplitude.

A special collimator was designed to fit one of the holes of the collimator matrix. It was made of 3 mm thick aluminium, containing three holes with a diameter of 0.5 mm in a straight line. The edges of the holes are separated by 0.25 mm, as shown in fig. 2.23(a). The three holes were irradiated with the ^{55}Fe radioactive source and the distribution of fig. 2.23(b) was obtained. The peaks were fitted with three Gaussian curves. The peak at the centre is higher due to the tails of the other two peaks. The LSFs of the three holes are completely separated from each other, showing that it is possible to distinguish objects as small as 0.5 mm diameter holes. It is remarkable that the valleys correspond to a distance of 250 µm between two holes.

The energy resolution was also determined. By irradiating a small area of the detector (one of the 2 mm holes) and summing the charge collected from each edge of the resistive strip, a pulse height distribution of the ^{55}Fe source was acquired. This spectrum, is shown in fig. 2.24. The MHSP was operating at a charge gain of 10^4 ($\mathcal{E}_{\text{drift}} = 200\,\text{V/cm}$, $\Delta V_{\text{h}} = 440\,\text{V}$ and $\Delta V_{\text{s}} = 260\,\text{V}$). The tail due to the K_β X-rays was excluded from the distribution and the resolution obtained for the K_α peak was found to be 15.3 %. This value is worse than the values obtained with the standard MHSP, but is still within the typical energy resolution obtained for gaseous detectors. The

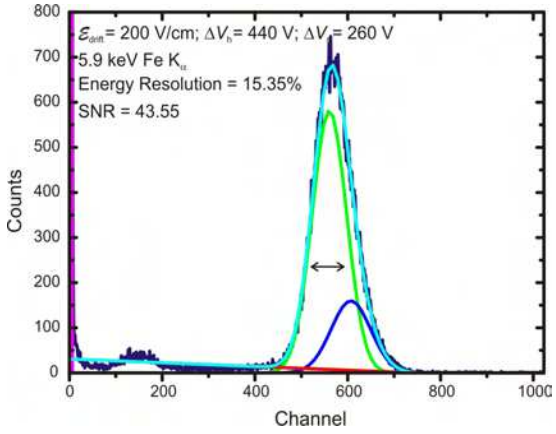

Figure 2.24: The spectrum of a ^{55}Fe source, obtained by summing the charge signals from both edges of the resistive strip. The energy resolution is 15.35 % (FWHM)

signal-to-noise ratio in these conditions was 43.55, higher than the 25 obtained with the proportional counter connected to the resistor chain.

2.4.2 Digital electronics

As discussed at the beginning of this chapter, another possible approach for data acquisition is the digital sampling and further processing of the signals in an event-by-event philosophy. Digital electronics for signal sampling and processing can drastically reduce the price of the acquisition system. It also simplifies data processing, opening a window to many possibilities such as event discrimination based on parameters like pulse height, rise- or falling time or pulse shape, and application of energy weighing or other image enhancement techniques. All this can be done off-line or in real time. Nowadays, digital electronics allows sampling rates of the order of hundreds of MHz, leading to a much lower electronics dead time, providing much more information at high counting rates. The drawback is the electronic noise introduced in the system. This should be carefully taken into account, given its sensitivity to the signal-to-noise ratio.

Taking advantage of the promising results obtained in the last section, when collecting the charge pulses from the anode strips of the MHSP, a PCI board equipped with 4, 200 MHz 8-bit ADCs designed in the Electronic Instrumentation Group of the Physics Department of the University of Coimbra (GEI) was used to estimate the possibility of digital readout of the signals. This board was prepared to acquire voltage signals with a positive amplitude up to 1 V. Since the resolution of the ADCs was 8 bits, the pulse amplitude of each channel is converted to an integer value between 0 and 255. The sampling rate was 200 MHz so, the pulses were fully sampled in bins of 5 ns over a user defined number of bins N. The result was a N-dimensional vector of 8-bit unsigned integers proportional to the pulse height in the 5 ns interval marked with a time stamp.

The photon energy is the sum of two pulses, therefore it has a resolution of 8+1 bits and takes values between 0 and 511. For the position, a division is made. The number of values it can take is the sum of the number of bits of one channel (8 bits) with the number of bits of the photon energy (9 bits): 17 bits of information. The stored data was then manipulated through a simple `MatLab`™ routine to allow the construction of energy and position histograms.

The same set of measurements was made as in the previous section: measurements of a single row of the 5×5 collimator matrix for INL estimation; measurement of a 150 µm thin slit for MTF calculation; and measurement of the aluminium collimator containing three 0.5 mm aligned holes, with a pitch of 0.75 mm. The energy distribution was not satisfatory due to the high noise of this board and low resolution of the ADCs. The measurements were done collecting the charge from the anode strips of the MHSP. The MHSP was biased to have a drift field $\mathcal{E}_{\text{drift}} = 200\,\text{V/cm}$, a voltage across the holes $\Delta V_{\text{h}} = 440\,\text{V}$ and a voltage of $\Delta V_{\text{s}} = 260\,\text{V}$ across the strips.

Two approaches were studied. In the first, the charge signals were integrated and shaped, and only then, they were sampled and stored. In the second, the analog shaping amplifiers were not used and the signals were sampled directly after being integrated, i.e., from the preamplifier output. The stored events were then processed off-line in both cases. This would test if it is reasonable to save the cost of having a further shaping stage for each of the four electronic chains.

Digital sampling after analog shaping of the integrated charge

As mentioned before, the same single row of holes used in section 2.4.1 for signal collection from the strips of the MHSP was irradiated. The row is the same from the previous section, as can be verified in fig. 2.25(a) by the partially covered hole. The rightmost peak is not a hole, and results from signals with an amplitude higher than the maximum input of the board, clipped to the maximum 8-bit value, which originated false coincidences with the noise. They did not influence the final result. The *integral nonlinearity* is roughly the same as achieved with the analog divider, as expected. The INL is a property of the MHSP dominated by the uniformity of the resistive strip and is barely influenced by the electronics.

The LSF of the 150 µm thin slit shows poorer position resolution and contrast when compared to the studies made with analog electronics. From fig. 2.26(a) it is noticeable that the slit was not exactly in the middle of the central 2 mm circular hole. This deviation, measurable from the calibrated data, is 0.38 mm. It corresponds to an effective area less than 10 % smaller than the area of the slit if it were exactly centred in the circular hole. The loss of contrast compared to the case of analog electronics is 72 %, which shows that the reason for loss of contrast is beyond the slit's deviation from the centre. The amount of noise introduced in the system due to the PCI board decreases the signal-to-noise ratio, having consequences in the position resolution. The width of the slit's LSF was found to be 435 µm. From equation 2.7, the resolution corresponds to an estimated decrease of 30 % in the SNR. Nevertheless, it is still possible to have submillimetric position resolution. The MTF shows a resolution of $2.5\,\text{lp/mm}$ at an

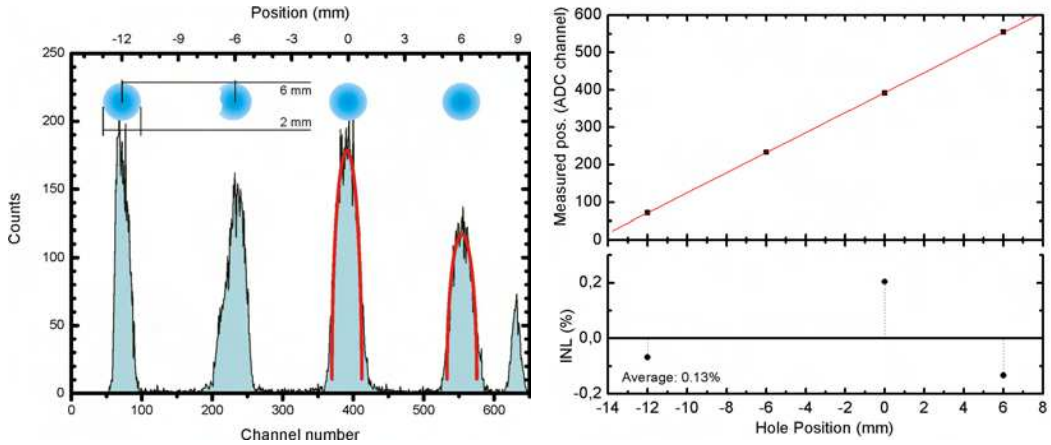

(a) (b)

Figure 2.25: (a) A row of four holes from the 5×5 collimator matrix, with the pulses digitised after being integrated and shaped. The scale of the holes is represented as blue/shaded circles above the peaks. The hole that was partially covered by epoxy is clearly seen in the distribution. (b) The *integral nonlinearity* was 0.13 % of the whole length of the resistive strip, as expected from the measurements in the previous section.

amplitude of 3 %.

This position resolution is enough to distinguish the three holes in the aluminium collimator as seen in fig. 2.27. The peak-to-valley ratio is smaller than in fig. 2.23(b) due to the poorer position resolution.

Direct digital sampling of the integrated charge

In this subsection, the analog shaping amplifiers were removed from the electronic chain, and the charge pulses were sampled immediately after the pulses were integrated by the preamplifiers. Without the shaping amplifiers to remove part of the noise and without any software for signal treatment, the position resolution is expected to get worse. This is already noticeable in the distribution of fig. 2.28. The same row of holes is irradiated with the ^{55}Fe source and the peaks appear with a shape closer to bell shaped curves than to the already known LSF of circles. This means that the resolution is much poorer. However, the partially covered hole can still be recognised as before. The leftmost hole appears completely deformed because the pulses closer to this edge of the MHSP's resistive strip were saturated.

Figure 2.29(a) shows the LSF of the 150 µm slit, much wider due to the lower SNR. It has a width of 716 µm (FWHM), and a contrast of $^1/_{24}$. With this loss in position resolution, it is expected that the MTF decreases much faster, showing a resolution of 1.4 $^{\text{lp}}/_{\text{mm}}$ at 3 % of its maximum amplitude. Despite the poor resolution, the three holes of the aluminium collimator can still be distinguished (fig. 2.30).

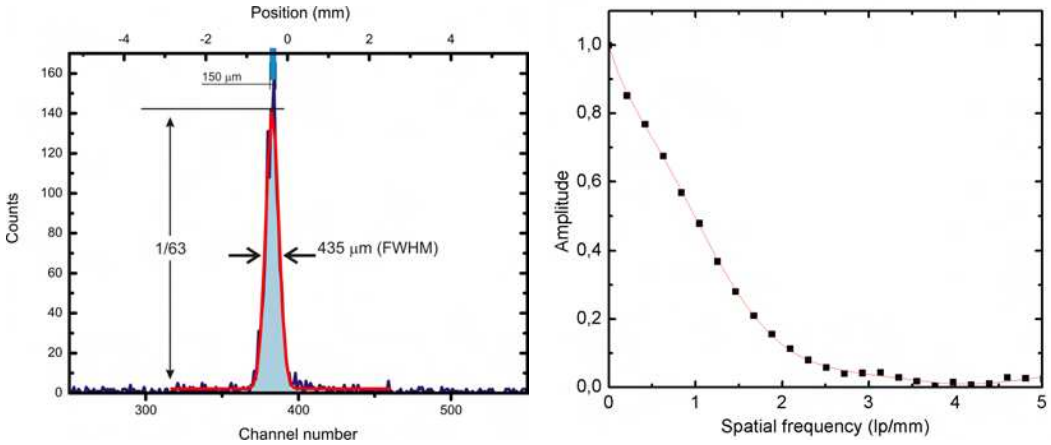

(a) (b)

Figure 2.26: (a) The 150 µm thin slit. The contrast and position resolution are much worse than those obtained with analog electronics. The fact that the slit is not centered with the 2 mm hole has less influence than the noise generated by the PCI board. (b) The MTF shows a resolution of 2.5 $^{lp}/_{mm}$ at an amplitude of 3 %, due to the decrease of contrast.

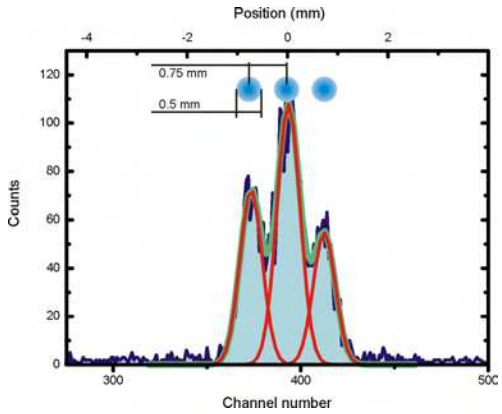

Figure 2.27: The LSF of the aluminium collimator with the position determined digitally. The resolution is worse than that obtained with analog electronics, but the three holes are well distinguishable.

This shows that the term "position resolution" does not represent the limit of the size of the objects that can be visualised, as described in section 2.3.3. The position resolution just arises from the need of using a quantitative term to define a property of the system.

2.5 Discussion

The total resistance of the resistive strip used in these studies was a compromise between the pulse rise time and the signal-to-noise ratio. With the typical 15 kΩ, a SNR above 40 was achieved with the ^{55}Fe radioactive source, with the pulses collected from the strip electrodes. According to equation 2.7, for a SNR of 43.6, $\sigma_x = 230\,\mu m$, which, multiplied by $\sim$ 1.175 is the value obtained experimentally. Applying the same reasoning to the signals collected from the GEM-electrode, assuming the SNR to be 35 % of 40, one would expect a position resolution around 800 µm for the other coordinate. It is obvious that the noise problems in the GEM-electrode are not only due to the resistive strip. In fact, the biasing potential of the GEM-electrode is much lower than the others and serves only to create the drift electric field. Lower voltages are much more sensitive to external noise sources and, although the signals have typically 35 % of those from the strips, the SNR is around 10, which might explain the spatial resolution obtained.

Other limiting factor in the position resolution is the range of the photoelectrons in the gas. Each X-ray from the ^{55}Fe radioactive source typically removes one electron from the L-shell of xenon and one Auger electron. The energy of the photoelectron is $E_{K_\alpha} - E_L \approx 1\,keV$, whereas the energy of the Auger electrons is in average 3.6 keV. According to [15] and [16], this corresponds to a position resolution limit of 60 µm due to the electron range in the gas. At this energy, the position resolution is doubtlessly limited by the noise rather than the range of the photoelectrons. In the next chapter, the dependence on the electron range will be discussed, describing experiments where an X-ray tube was used, providing measurements over a wide range of energies.

After confirming the imaging capability of the MHSP, using it with analog electronics, the tests made with digitisation of the pulses might limit the performance of the imaging system. The results obtained with the fast PCI board developed in GEI

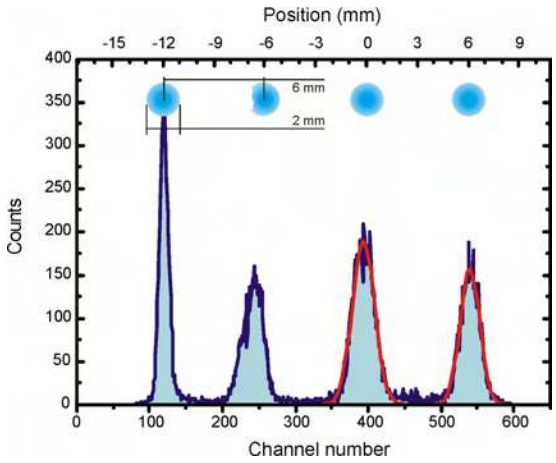

Figure 2.28: The row of holes presented before. The pulses were collected directly after charge integration, with no shaping stage.

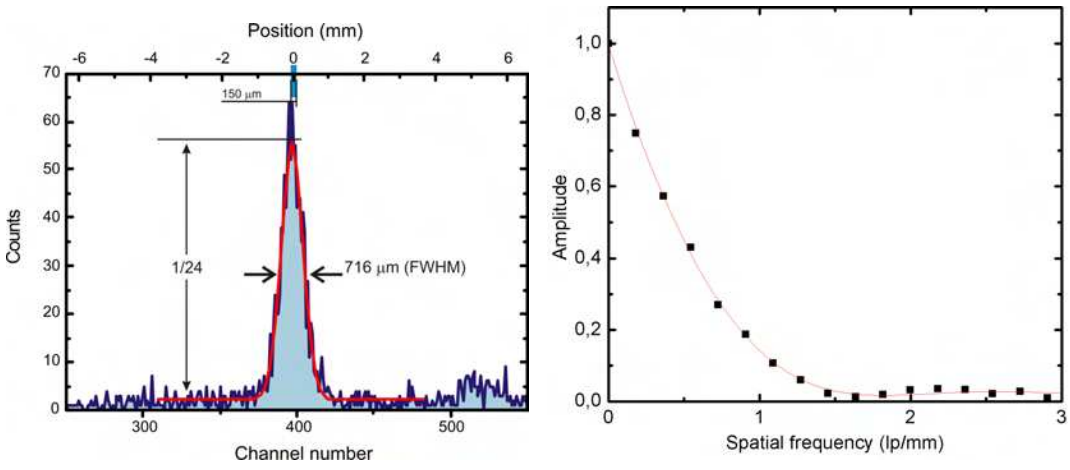

Figure 2.29: (a) The 150 µm thin slit without the shaping stage. The contrast and position resolution are worse than those obtained with the analog shaping stage. (b) The MTF shows a resolution of 1.4 lp/mm at an amplitude of 3 % of its maximum.

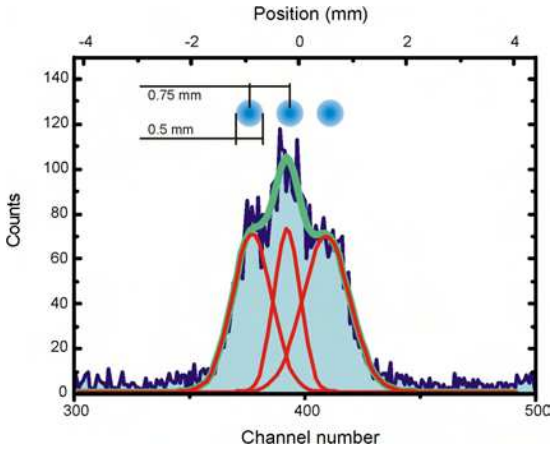

Figure 2.30: The LSF of the aluminium collimator with the position determined digitally. The resolution is worse than that obtained with analog electronics, but the three holes are still distinguishable.

have shown that a limited resolution of the ADCs jeopardises the energy resolving capability. Furthermore, introducing a high amount of noise in the electronic chain results in poorer position resolutions. However, it has been shown that the need of analog shaping amplifiers can be questioned, because a resolution just above 700 µm was obtained even without the analog shaping stage. The use of digital shaping is a reasonable solution as an effective way to reduce the noise introduced by the digital electronics, while reducing the cost of the signal acquisition and processing system.

After the 1D-images analysed in this chapter, a detector designed for data acquisition in four channels, providing all the information needed for 2D-imaging was ready to be used with the 2D-MHSP, as described in the next chapters.

Chapter 3

Imaging with the Micro-Hole & Strip Plate in xenon

The conclusions reached with the studies at 1D were applied in a truly X-ray imaging detector. A new detector provided with all the necessary biasing and signal feedthroughs to acquire signals from both edges of each resistive strip was built. The radiation entrance window was a $25 \times 25\,\mathrm{mm}^2$ square made of 75 µm thick Kapton™ foil, evaporated with aluminium.

For digital sampling of the pulses, the CAEN™ 1728b NIM module [64], equipped with 4 ADCs with a resolution of 14 bits and a 100 MHz sampling rate was chosen. The module provides real time digital signal shaping, along with data storage for further processing. It contains a TNT2 board[1] developed in the *Institut Pluridisciplinaire Hubert Curien* (IPHC) of the *Institut National de Physique Nucléaire et de Physique des Particules* (IN2P3), *Centre National de la Recherche Scientifique* (CNRS) in Strasbourgh, France.

The module is equipped with a Xilinx Virtex II FPGA for pulse processing and hardware control, and a Spartan II FPGA for system configuration [65]. It operates in several modes, namely in *oscilloscope mode*, sampling the pulses in bins of 10 ns, as a sampling ADC; or in *energy mode*, storing each event in a table with the pulse amplitude, time stamp, input channel and trigger number. This second possibility discards the information relative to the pulse shape, saving resources in terms of memory and processing, leading to much faster data processing. The capabilities of the TNT2 board are immense and all the parameters related to the data acquisition and processing can be adjusted according to the user's needs.

It acquires the integrated charge from the preamplifiers and the digital shaping is done using the Jordanov algorithm [5,66,67] to make a trapezoidal pulse. In short, the

[1] TNT is the acronym for *Treatment for Numerical Tracking*. This board was designed for digital acquisition in the *Traccking gamma AGATA* and the *NTOF* projects in former *Institut de Recherches Subatomiques* (IReS), now *Institut Pluridisciplinaire Hubert Curien* (IPHC). The first finished version (TNT) had two channels sampled at 65 MHz and one FPGA. The TNT2 was released in 2004.

exponential pulse at the output of the preamplifier can be approximated to the form

$$\nu(t) = \frac{1}{\tau - \theta}\left(e^{-t/\tau} - e^{-t/\theta}\right),$$

where θ and τ are the rise- and decay time of the pulse. The pulse is then digitised and converted to a symmetrical trapezoidal pulse $s(n)$ through a recursive algorithm given as [66]:

$$\begin{aligned} &d^{k,l}(n) = \nu(n) - \nu(n-k) - \nu(n-l) + \nu(n-k-l), \\ &p(n) = p(n-1) + d^{k,l}(n) \quad n \geq 0, \\ &r(n) = p(n) + M d^{k,l}(n), \\ &s(n) = s(n-1) + r(n) \qquad n \geq 0. \end{aligned} \tag{3.1}$$

The parameter n is the time and k is the time of the trapezoid's leading edge (the time the amplitude takes to reach the maximum), defined by the user. The value of l is given by $l = k + m$, where m is the width of the flat top (also user defined). All time units are in sampling periods ($T_{\text{clk}} = 10\,\text{ns}$, in the case of this board), i.e., to have the real time, they must be multiplied by 10 ns. The total width of the trapezoid base is, therefore, $2k + m$. The parameter M depends on the decay time τ of the pulse and on the sampling period:

$$M = \frac{1}{\exp(T_{\text{clk}}/\tau) - 1}.$$

The pulse height can be averaged over any region of the flat top, where the width of the region and its location are also user defined (called *average width* and *average shift*, respectively). This has some importance because, for pulses crossing a longer distance over the resistive strip (hence higher resistance), the rise time θ increases. The intersection of the leading edge with the flat top of the trapezoid becomes round and the trapezoid reaches the maximum amplitude closer to the end of the flat top.

The user interface with the board is made via USB, controlled through a `Java`™ application (TNT2 USB Control Software — `TUC`), from where all the parameters are set and the data acquisition and storage processes are controlled. The NIM protocol, standard power supplies for all the electronics used in the laboratories where this work was carried out; as well as the USB2 interface with a personal computer, with a "ready-to-use" `Java`™ application were the decisive factors for the choice of the CAEN™module. The use of VME or CAMAC protocols might be more appropriate, but this would imply the acquisition of crates and the development of the control software from the very beginning, requiring a type of work out of the frame of this research.

An adapted educational copper X-ray tube was used as the X-ray source. The X-ray energy could be set to 25- or 30 keV and its maximal current was 0.13 mA. The tube was placed about 1 m away from the detector. For image acquisition, the objects were simply placed between the X-ray tube and the detector, as close to the radiation window as possible.

Each pulse triggered in the NIM module was recorded in a binary file. This file was then processed with the program `Radix`, developed in our research group, over

the MatLab™ platform. Although Radix is a program for data filtering, organising and displaying rather than for actual data analysis, it proved to be a very important tool in the manipulation of the data. Each detected X-ray photon is one event providing one charge pulse in each of the four input channels. This routine organises the pulses in groups of four, inside user defined time windows. The pulses in a time window where one or more channels are missing do not form an event and are discarded. The x- and y-coordinates are then calculated through equation 2.2 and plotted in 2D intensity maps forming an image, together with the energy spectrum. With Radix, different energy regions can be selected to visualise the corresponding image and, conversely, different regions of the image can be used for energy spectrum visualisation. The intensity maps and spectra can also be converted into numerical vectors and matrices for further analysis with standard data analysis software.

3.1 Integral Nonlinearity

To study the *integral nonlinearity* of the detector and to calibrate the images, determining how many pixels correspond to 1 mm, an image was taken from a 300 µm thick stainless steel hexagonal mesh. The hexagons had 2.8 mm long edges with a width of 360 µm, as seen in fig. 3.1(a). The X-ray transmission for 300 µm of stainless steel is around 16 % for 30 keV and is negligible below 20 keV [68]. Given the energy spectrum of the X-ray tube, it is expected that most of the radiation is absorbed by the mesh material. For the energy of the X-ray photons crossing the mesh material, the detector has a very low efficiency. Figure 3.1(b) shows the X-ray image obtained, in a 300×300 pixel matrix. The size of the matrix was chosen to have a pixel size small enough not to limit the actual detector position resolution at the same time the intensity of each pixel was statistically significant.

The position of each vertex of the mesh was compared to the position obtained in the X-ray image. For that, position (0,0) was assigned to one of the vertices and the position of the others was measured relatively to this. The fact that the mesh was tilted by 2.9° was taken into account. The correction factor corresponds to 5 % in the final $^{\text{pixels}}/_{\text{mm}}$ ratio, but has influence in the correct determination of the INL. The comparison between the expected position of each vertex and the measured value is shown in fig. 3.2. The INL is the distance between the red and the green data points averaged over the whole data set. It was 270 µm, corresponding to 1 % of the length of each resistive strip. In fact, some of the hexagons appear distorted in the X-ray image.

A thorougher inspection of fig. 3.2 reveals, that in the region inside the rectangle, the red and the green data points are closer together. If only these points were taken into account, the INL would drop to 180 µm, corresponding to 0.6 % of the length of the resistive strips, suggesting that the images are less distorted at the centre of the MHSP.

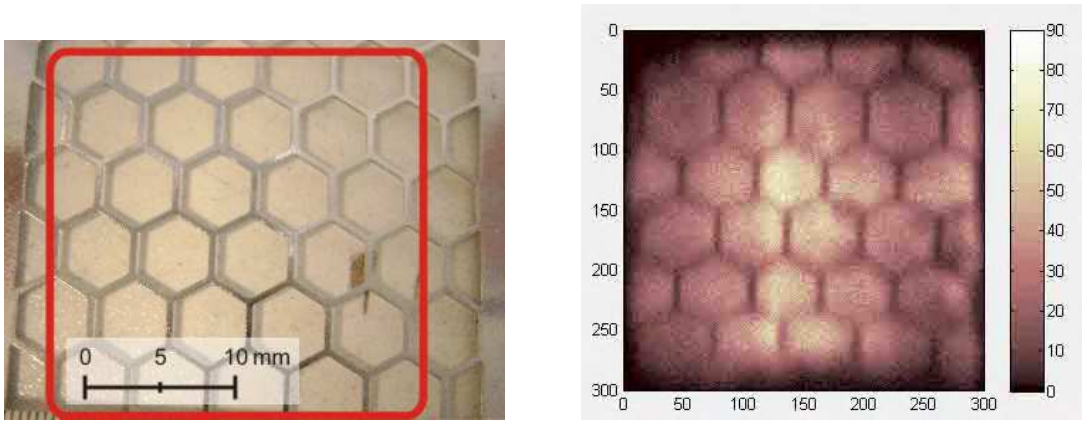

(a) (b)

Figure 3.1: (a) A picture of the hexagonal mesh used to determine the INL of the system. The edges of the hexagons were 2.8 mm long and 360 µm wide. The red square represents the detector window and the area imaged. (b) The X-ray image of the mesh.

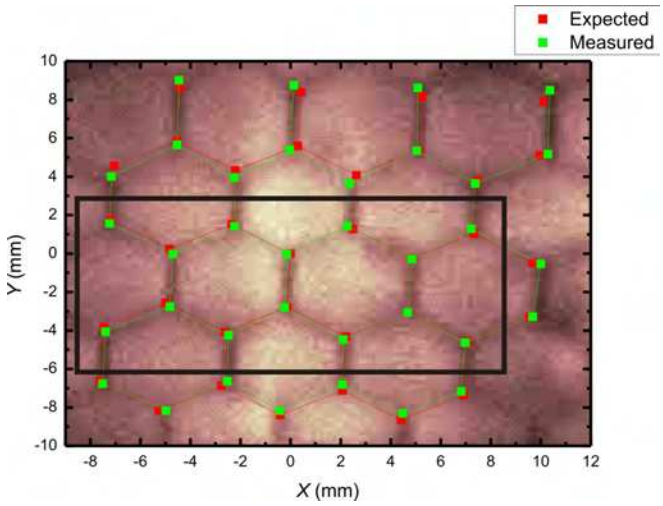

Figure 3.2: The position of the mesh vertices in the X-ray image (green) is compared with the expected position calculated from the mesh dimensions (red). The INL is 1 % of the length of the resistive strip, when all the points are taken into account. If only the points at the center of the image are considered (area inside the rectangle), the INL drops to 0.6 %.

3.2 Position resolution

As in chapter 2, a 150 µm thin slit was imaged, but now it was possible to visualise it, as shown in fig. 3.3(a). A small area of the image, marked with a red rectangle was selected to calculate the *line spread function* of the slit, shown in fig. 3.3(b). The width

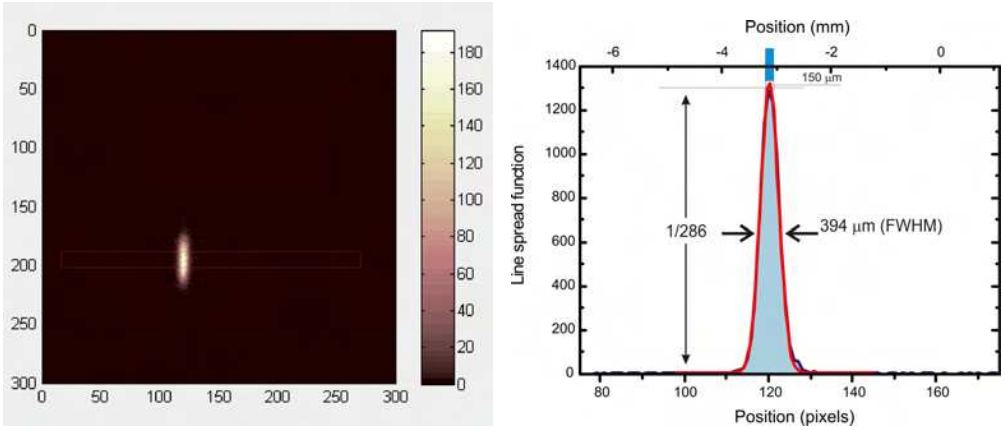

(a) (b)

Figure 3.3: (a) The 150 µm slit was imaged in the vertical position to determine the resolution of the imaging system in the x direction. (b) The line spread function (LSF) of a selected area of the slit gives a distribution with a width of 394 µm (FWHM), corresponding to a position resolution of 386 µm.

of the LSF was 394 µm (FWHM), corresponding to a position resolution of 386 µm. This was slightly better than that obtained with the fast digital electronics (page 54). In that case, a shaping amplifier was used in each electronic channel, and in this case, only the Jordanov algorithm was used. The contrast obtained was higher than in the case of analog electronics, but now, a much higher X-ray intensity was used. This has the consequence of reducing the influence of the background, even if the position resolution is poorer.

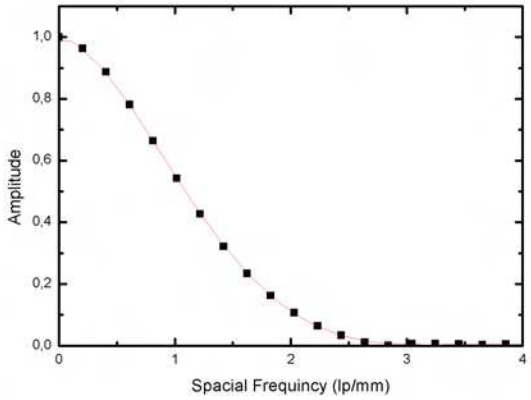

Figure 3.4: The modulation transfer function (MTF) of the region marked in fig. 3.3(b) shows 2.5 $^{\text{lp}}/_{\text{mm}}$ at 3 % of the maximum amplitude.

The *modulation transfer function*, calculated from the slit's LSF, is shown in fig. 3.4.

The resolution at 3 % of its maximum is 2.5 $^{\mathrm{lp}}/_{\mathrm{mm}}$, once again consistent with the relationship between the LSF and the MTF, and very similar to what was obtained with the digital electronics with analog shaping.

Figure 3.5: A 0.5 mm thick stainless steel mask with the shape of the griffon vulture, the symbol of the University of Aveiro. This mask had both small and large features and could be used to evaluate the ability of the detector to distinguish smaller details.

A 0.5 mm thick stainless steel plate with the symbol of the University of Aveiro—the griffon vulture—was used in front of the detector window to project its *shadow* in the MHSP. Figure 3.5 shows how small are some features of the mask (tongue and tail of the vulture) at the same time it has other larger features. This mask was very helpful during the measurements, providing a quick qualitative estimation of the image quality.

The X-ray image can be seen in fig. 3.6(a), for which only the events in the region of interest marked in red in fig. 3.6(b) were used. Even the smallest details can be distinguished. Furthermore, it confirms that the position resolution does not deteriorate visibly in most of the imaged area. Some *pincushion* distortion is noticed near the edges, as expected. The energy spectrum on the right is the typical spectrum obtained for gaseous detectors. This energy resolution is not enough to separate the copper K_α and K_β lines, but the xenon escape peak is clearly seen, as well as the *bremsstrahlung* continuum of the X-ray tube.

The image of the griffon vulture has enough information to allow determination of the position resolution of the system through the *edge spread function*. In fact, one just needs to choose one edge sharp enough for each of the x- and y-coordinates and determine the position resolution in both directions. Figures 3.7(a) and (b) are the *edge spread function* taken from the red (a) and the blue (b) rectangles marked in fig. 3.6(a). As explained in the last chapter, ideal distributions should be step functions, however, for the real case, the edges of the steps are rounded due to the *point spread function* of the system.

The distributions were adjusted to sigmoidal functions. After calculating the derivative of the fitting function, a peak function is obtained and its width is the spatial resolution. The results obtained for the x-coordinate are consistent with what has been measured by the LSF of a 150 µm slit, therefore this method can be used to determine the position resolution of the y coordinate: 1.1 mm. The *pincushion* distortion was taken into account when calibrating the image ($^{\mathrm{pixels}}/_{\mathrm{millimetre}}$) in this region

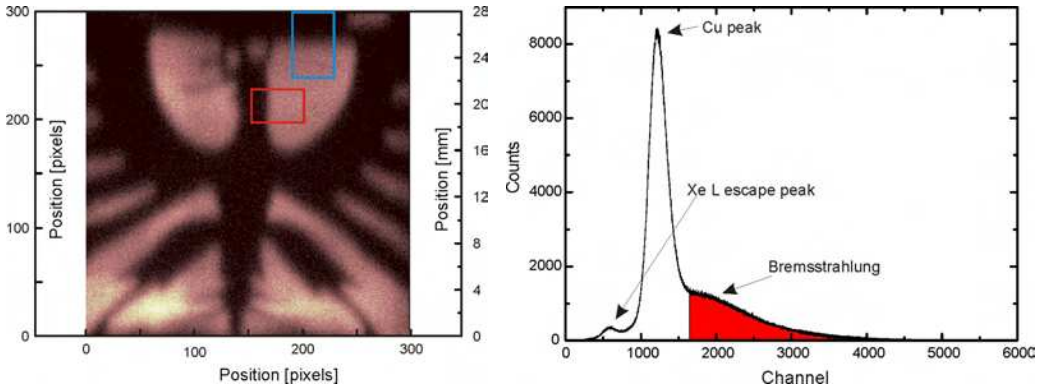

(a) (b)

Figure 3.6: (a) The X-ray image of the griffon vulture: small details such as the tongue and the tail features can be distinguished. The tongue has a width of around 0.5 mm. (b) The energy spectrum of the X-ray image on the left. Different parts of the energy spectrum can be selected to build the image. The image in (a) was built using the energy region marked in red.

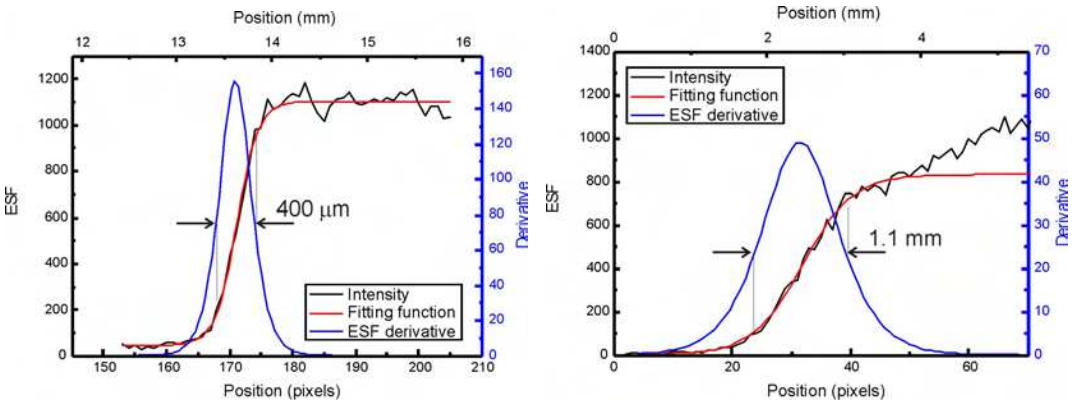

(a) (b)

Figure 3.7: Two edge spread functions used to determine the position resolution in x (a)—red rectangle; and y (b)—blue rectangle. The value obtained for x is consistent with that obtained from the LSF of the 150 µm thin slit. The position resolution for the y coordinate is 1.1 mm (FWHM).

near the edge of the MHSP.

3.3 Energy discrimination

As mentioned before, the images acquired with this system are also energy resolved. For each event, three coordinates are stored: x, y and E—the X-ray energy. It is a *colour* X-ray image, where the *colour* is given by the X-ray energy. The `Radix` software allows to select energy regions to obtain the image formed only by those events within that energy region.

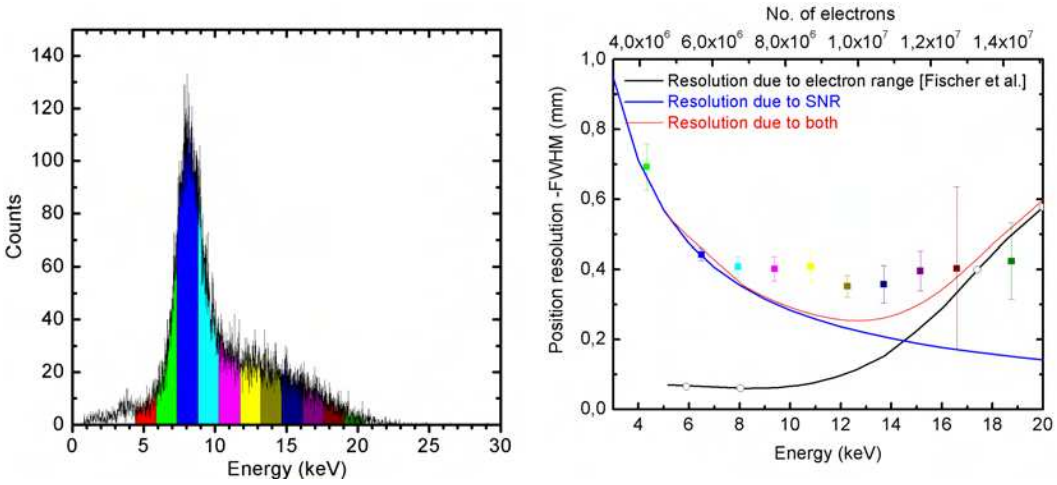

(a) (b)

Figure 3.8: (a) The energy spectrum of the image of the 150 µm thin slit image. Several energy regions were selected and the position resolution of the correspondent image was measured. (b) The width of the imaged slit as a function of the energy region. For the lower energies, the position resolution is limited by the SNR (blue curve), but at higher energies, the range of the photoelectrons dominates (black curve). The red curve represents both contributions.

Figure 3.8(a) shows the energy distribution of the image of the slit. Different regions of interest in the energy distribution were selected and the width of the image was determined for each of the regions. Figure 3.8(b) depicts the FWHM of the slit's image for each of the energy intervals. The error bars are the standard deviation of the width of the slit, fitted with a Gaussian curve in each line of the image with the width of one pixel. They reflect the variations in the statistical quality of the data. For some regions of energy, the number of events was much lower, giving origin to larger statistical fluctuations and, therefore, less accurate fittings. The curves in the graph have the expected behaviour of the energy dependence of the position resolution, due to the signal-to-noise ratio according to equation 2.7 in page 37, for an electronic noise of around 300 eV (blue curve); and due to the primary electron range. The black curve is the data from fig. 2.14, as published in [15] and [16]. The red curve represents the

expected resolution due to the influence of the SNR and the photoelectron range

$$\sigma = \sqrt{\sigma_{\mathrm{SNR}}^2 + \sigma_{\mathrm{range}}^2}.$$

A detailed discussion on the position resolution limitations will be carried out in the next section of this chapter.

The possibility of defining energy regions has, however, other advantages besides the eventual improvement of the position resolution. For objects with internal structure, such as small vertebrates, harder X-rays penetrate more dense matter and softer X-rays are transmitted only by less denser structures. This can be used to *tune* the image contrast according to the type of object to be imaged. The wing of a common quail (*Coturnix coturnix*) was used, transmitting the X-rays from the tube. Figure 3.9(a) is the false coloured X-ray image of the wing when all the X-ray energies were used to build the image. Some bones are clearly distinguishable, such as the humerus, the ulna and the radius. The contour of the soft tissue, composed by the flesh and the skin can also be distinguished. In fig. 3.9(b), the transmitted energy spectrum is shown. The X-ray beam was *hardened* by the quail wing, decreasing the intensity of the copper peak and enhancing the *bremsstrahlung* continuum above channel 1700. Two energy regions were selected to rebuild the image. The lower energies, up to around 10 keV, marked in red, had the result shown in fig. 3.9(c) and the higher energies, marked in blue, built the image in fig. 3.9(d). The lower energies enhanced the contrast in the softer tissue and the higher energies revealed extra features in the bones. The amount of information contained in each image, including energy, can be used to improve contrast in special areas of the objects.

3.4 Discussion

The use of xenon as the filling gas at 1 bar tested the performance of the 2D-MHSP. The properties of xenon working with gaseous proportional counters are well known as well as its ionisation and excitation thresholds. Furthermore, this gas is among the most used in the labs where this work was carried out. It was assumed from the beginning that the gradual development of the imaging system should be made using a well known non-molecular gas. With this, it would be simple to isolate eventual artifacts that could appear and to identify if the cause was due to subtleties related to the gas or the detection system itself.

The most important limitation of the detection system in terms of the position resolution is the signal-to-noise ratio. The width of the image obtained with the thin slit can be plotted as a function of the total biasing voltage of the MHSP and the gain in charge. Figure 3.10 shows that the width of the thin slit in the X-ray images decreases as the detector gain increases. It was shown that the position resolution keeps improving with the biasing voltage, as expected from equation 2.7. If the biasing voltage could be indefinitely increased, at some point, the signal-to-noise ratio would be so high that the position resolution would be limited only by the range of the photoelectrons. This limit has not yet been achieved and the only factor that is keeping

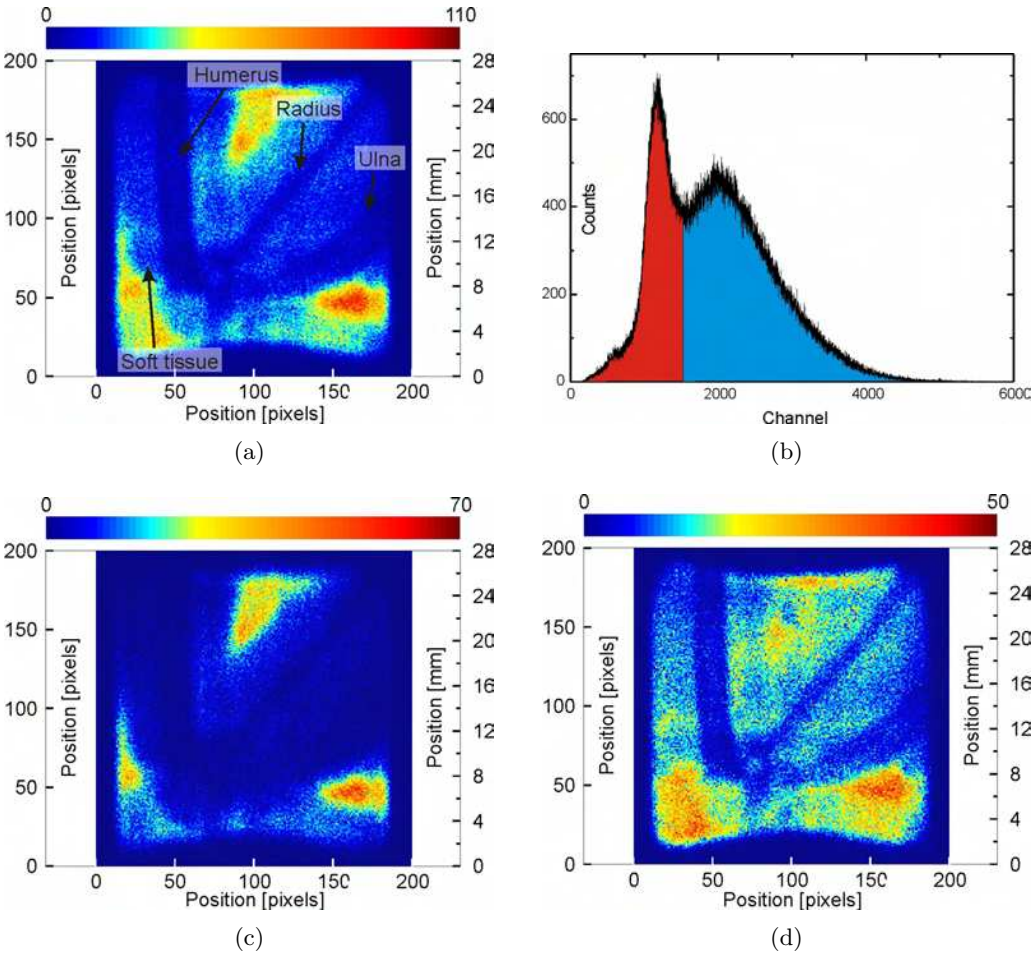

Figure 3.9: (a) The image of a folded common quail (*Coturnix coturnix*) wing, using the whole energy spectrum. (b) The transmitted energy spectrum. The lower energies were mostly absorbed within the object. Two energy regions were selected to rebuild the image. (c) The lower energies originate a loss of contrast in the bones, but enhance it in soft tissue. (d) The higher energies are more suitable to visualise features in the bone at the same time the soft tissue vanishes from the image.

from increasing the signal-to-noise ratio through the detector gain is the sensitivity of the MHSP to electrical discharges above some voltage threshold. This threshold depends on the MHSP quality of manufacture, which is improving as the technique is developing. The maximum biasing voltages achieved along these studies were dictated by the onset of micro-discharges and unstable behaviour in the MHSP.

The performance of the imaging system developed in this chapter is consistent with the expected limitations due to the SNR and due to the range of the photoelectrons in the gas, showing an improvement due to the SNR as the X-ray energy increases up to a certain point, from where limitations due to the electron range become dominant.

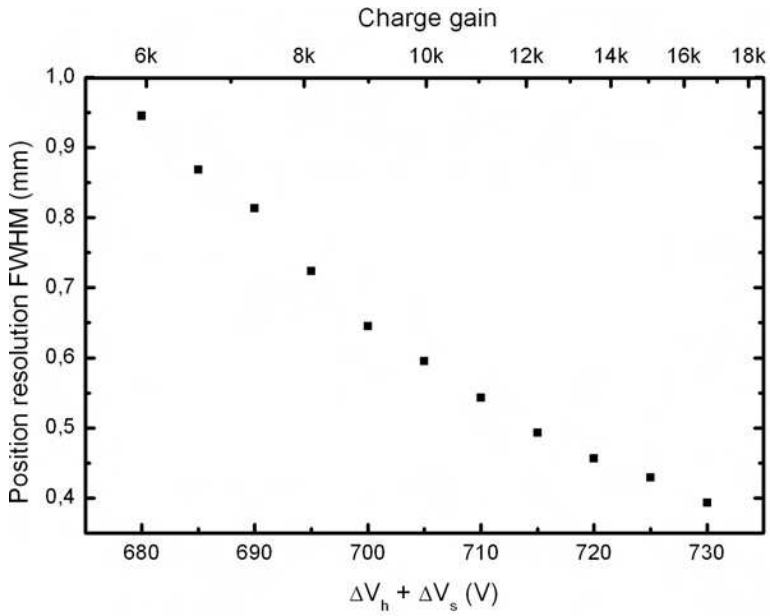

Figure 3.10: The width of the image of the slit (FWHM) as a function of the total biasing voltage of the MHSP and the total charge gain. A region where the position resolution stabilises has not yet been reached, showing that there is some room for improvement.

The other major issue is the *integral nonlinearity* (INL), which is directly related to the resistive strip in two aspects:

the nonuniformity of the resistive line which is presently, the most important factor. The width and thickness of the resistive strip have variations along its length. Therefore, the resistance between adjacent strips is not constant, causing distortions in the image. If the position determination is seen as a measurement of the resistance, then it can be written as:

$$x = \frac{l}{2}\left(\frac{R_\mathrm{L} - R_\mathrm{R}}{R}\right), \tag{3.2}$$

with $R = R_\mathrm{L} + R_\mathrm{R}$ and l as the length of the resistive strip. This equation is slightly different from equation 2.3, because the charge used to build the image passes through R_L and R_R, which are not independent. Equation 3.2 can be rewritten using only variable R_L:

$$x = \frac{l}{2}\left(\frac{R_\mathrm{L} - (R - R_\mathrm{L})}{R}\right) = \frac{lR_\mathrm{L}}{R} - l.$$

R_L can be replaced to include the thickness t, the width w, the partial length l_L and the resistivity ρ of the resistive strip:

$$x = \frac{l}{R} \cdot \frac{l_\mathrm{L}}{wt}\rho - l. \tag{3.3}$$

Assuming the width and the thickness of the resistive strip independent, the error in the position is given as:

$$\sigma_x^2 = \left(\frac{\partial x}{\partial w}\sigma_w\right)^2 + \left(\frac{\partial x}{\partial t}\sigma_t\right)^2$$

and

$$\sigma_x = \frac{lR_{\mathrm{L}}}{R}\sqrt{\frac{\sigma_w^2}{w^2} + \frac{\sigma_t^2}{t^2}}. \tag{3.4}$$

From this, it is easy to conclude that a standard deviation of 1 % in the width and in the thickness of the resistive strip causes a deviation of 1.4 % in the position. While the resistive strip can be considered uniform as a whole, the resistance between two adjacent strips is around $100 \pm 10\,\Omega$. This difference evens out through the length of the strip, but sometimes, regions of lower or higher resistance appear.

Some development in the procedure of application of the resistive strip is being carried out, shown by the high level of uniformity of the most recent batch of 2D-MHSPs manufactured in CERN, almost eliminating these artifacts. The off-line correction of this kind of nonuniformity in images is not trivial and would imply a very thorough study of the properties of each resistive line. Therefore, the improvement of the uniformity of the resistive line is an imperative to optimise the INL.

***pincushion* distortion** this was already expected and has been commented in section 2.2.1, page 33. Near one edge of the resistive strip, the pulse on the opposite side not only decreases its maximum amplitude, but also takes a longer time to reach it (in electronics jargon: it becomes *slower*). Since the value of k (the time of the trapezoid's ramps) in the digitising board is constant, the ballistic deficit increases with the pulse rise time. The consequence is: for events close to the edges of the resistive strip, the signal amplitude on the opposite side is smaller than the amount of charge arriving there, resulting in a deviation of the calculated position towards the edge. In the image, the corners look as if "pulled" away from the centre, resembling a pincushion. This artifact is relatively simple to correct whether by using suitable shaping constants to reduce the ballistic deficit (with some loss in high rate capability) or by using image correction algorithms.

The results of X-ray imaging using pure xenon have allowed to characterise the 2D-MHSP as an imaging device. Resolutions under the threshold of 1 mm have been achieved with good *integral nonlinearity*. This is consistent with the requirements for many X-ray digital imaging applications. Xenon has been successfully used in other works, including operating at higher pressures to decrease the photoelectron range at high energies (for example [58]). The advantages of recording the energy of each event together with its position are of major importance, allowing further image enhancement based in the energy of the photons. Furthermore, since all the validated events are recorded, the only limit in terms of dynamic range is the memory of the

data acquisition system. Theoretically, it is possible to acquire images with a very high number of shades of grey, as long as exposure time or radiation dose are not a limitation.

Chapter 4

The MHSP in tetrafluoromethane: aiming neutron imaging

As mentioned before, due to their charge neutrality, neutrons do not interact electromagnetically with matter. To detect them, they must be subject to a nuclear reaction. The isotope with the highest cross section for thermal neutrons is ^{3}He. As described in section 1.1, this isotope reacts with neutrons releasing a 573 keV proton and a 191 keV triton through the nuclear reaction: $\mathrm{n}(^3\mathrm{He}, \mathrm{T})\mathrm{p}$. The proton and the triton transfer their kinetic energy to the electrons in the gaseous medium.

Figure 4.1 shows the Bragg curves of protons and the tritons making use of data taken from the SRIM software [69]. It shows the energy loss of the particles created in the nuclear reaction along their paths in the gaseous medium. The number of electrons removed from the medium is proportional to the energy loss. The tritons loose their kinetic energy within a much shorter distance than the protons, due to their size. The result is a much smaller energy range (dashed peaks).

The centre of mass of the charge cloud is marked in the graph. This is the position of the centroid, obtained with the MHSP. It is shifted from the real position of the nuclear reaction by roughly 50 % of the proton range. This means that there is an intrinsic limitation to the position resolution, which depends on the proton range. The centroid obtained for an event gives the position of interaction with an uncertainty of nearly one half of the proton range around that point, as illustrated in fig. 4.2, where only the black dot is detected, but it can correspond to an infinity of possible orientations of the tracks.

In neutron applications, such as beam monitoring, the desired position resolution is 1 mm. Taking the proton range as a reference for the intrinsic position resolution, one has to reduce this range to 1 mm. Increasing the pressure of ^{3}He is out of question because the pressure at which the proton range is 1 mm is 66 bar [69] which, at the price of this isotope, is prohibitive. Furthermore, the design of a vessel capable of standing such a high pressure is not trivial. The solution is the addition of another

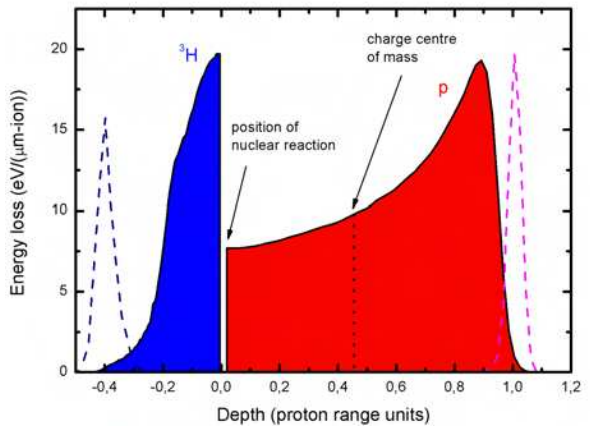

Figure 4.1: The energy deposited along the paths of the tritons (blue) and the protons (red). The energy deposition is proportional to the number of free electrons. The centroid of the distribution (centre of mass of the electron cloud) is not at the same spot of the nuclear reaction vertex. It is shifted by roughly 50 % of the proton range. The dashed peaks are the ranges of the tritons and the protons.

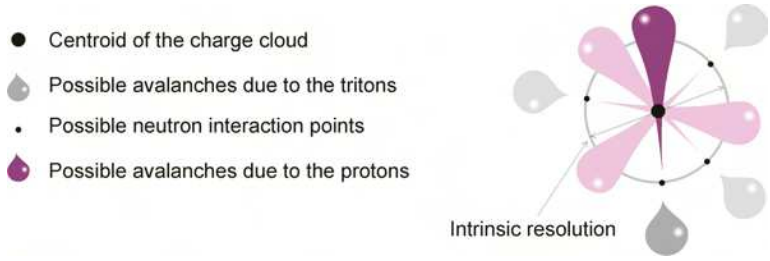

Figure 4.2: The position where the neutron was absorbed can be anywhere within the radius of one half of the proton range in the gaseous medium. This is an intrinsic limitation to the position resolution in neutron imaging.

gas, with higher density, to absorb the protons and tritons. A low gamma efficiency is mandatory, because nuclear reactions are followed by γ-ray emission, which give origin to photoelectrons with a high kinetic energy—hence a high range—, jeopardising the position resolution of the system.

The most popular gas is tetrafluoromethane, also known as carbon tetrafluoride (CF_4). The CF_4 molecule has a tetraedrical shape with the carbon atom surrounded by the four fluorine atoms at a distance of 132.3 pm. Although it is less dense than xenon (the density of CF_4 is 3.72 g/l, lower than the 5.89 g/l of xenon) it stops the protons in a shorter range. This is because the masses of fluorine and carbon are more similar to the mass of one proton, meaning a higher transfer of energy in each collision. In order to stop the protons in 1 mm, a pressure of only 2.6 bar is needed, which is much simpler to handle than the 66 bar of ^{3}He. A mixture of ^{3}He and CF_4,

with partial pressures of 6- and 2.6 bar, respectively guarantees that the neutrons are captured within a short distance, while the intrinsic position resolution stays below 1 mm.

For practical reasons, the studies in this chapter are once again carried out using X-rays to produce the charge clouds. The future test of this detector in a neutron beam implies the access to the nuclear spallation source, available in facilities like ISIS in the Rutherford Appleton Laboratory.

4.1 The standard MHSP in tetrafluoromethane

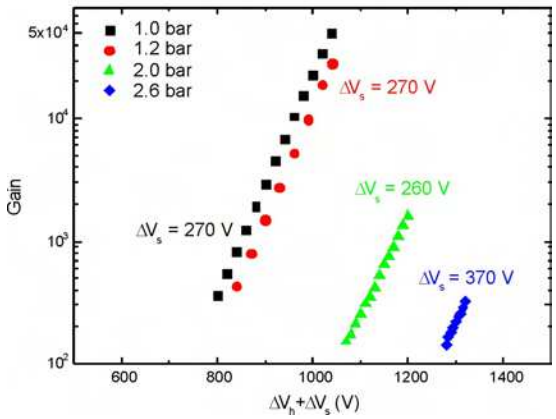

Figure 4.3: The gain in charge with an MHSP operating at different pressures of pure CF_4. At 1 bar, a gain of 5×10^4 was achieved. The gain drops rapidly with the increase of the pressure, but at 2.6 bar it was still above 300.

The performance of a standard MHSP in tetrafluoromethane (CF_4) atmosphere was tested in the pressure range of 1– to 2.6 bar. The detector was the same used in section 2.1. As expected, the detector gain drops as the gas pressure increases (fig. 4.3). To have the energy peaks above the electronic noise threshold, a ^{55}Fe X-ray source was used for pressures below 2 bar, and a ^{109}Cd source was used for pressures of 2 bar and higher. The gain distribution as a function of the biasing voltage has the expected logarithmic behaviour and can be fitted with equation 1.11 up to the maximum values used for these studies.

The values of the gain in charge were obtained by calibrating the electronic chain with the help of a calibrated 2 pF capacitor and a precision BNC™ pulse generator. By knowing the w-value of CF_4 ($w_{CF_4} = 54$ eV) and the energy of the radiation, it is possible to derive the gain in charge for each set of measurement conditions. The biasing voltage was increased across the holes and between the strips until the eminence of electrical discharge. CF_4 allows to use much higher voltages before the onset of discharges, due to its high dielectric strength. This has to do with the high electronegativity of the fluorine atoms and to the stability of the CF_4 molecule. The CF_4 molecule captures free electrons, giving origin to heavy negative ions which inhibit

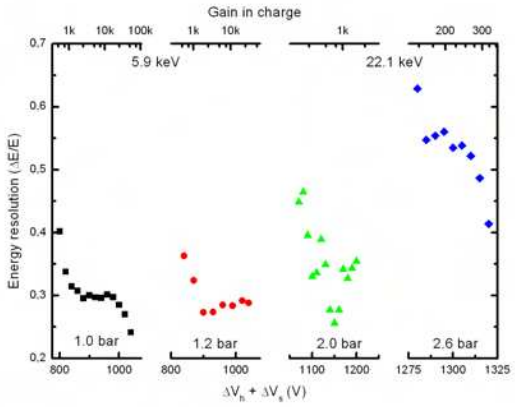

Figure 4.4: The energy resolution degrades with the increase of the pressure, maily due to the decrease of the charge gain. However, it was always possible to obtain energy resolutions below 50 %.

the onset of further electron streams. Due to small defects in the MHSP manufacturing, the MHSPs used in this set of measurements did not stand very high voltages between the strips. Nevertheless, it was possible to achieve much higher gains than in xenon atmosphere.

For 1 bar of CF_4 a charge gain above 5×10^4 was obtained. There is no doubt that the high dielectric strength of CF_4 is working in favour of achieving much higher charge gains with the MHSP. Very high gains with CF_4 have also been reported in other works [31]. However, the maximum charge gain drops significantly as the gas pressure increases. For 2.6 bar, it is possible to achieve gains just above 300. In the real case of neutron detection, where the deposited energy is 765 keV, instead of 22.1 keV, the amount of electrons generated by one single event will be quite enough to allow neutron detection with the MHSP, with a SNR around 35 times higher.

The energy resolution as a function of the biasing voltage applied (and the charge gain) is depicted in fig. 4.4. Energy resolutions below 50 % were always possible to achieve, regardless of the pressure of CF_4 that was used. It is also noticeable that the energy resolution degrades as the pressure increases, despite the higher energy of the X-rays used for 2- and 2.6 bar. This is because at higher pressures, it is not possible to achieve higher gains, which makes the detection more prone to statistical fluctuations.

A pulse height distribution is shown in fig. 4.5. For a gain of 1000 at 1 bar and the energy of an ^{55}Fe radioactive source ($K_\alpha = 5.9$ keV and $K_\beta = 6.5$ keV), a resolution of 29 % can be obtained for the K_α peak. This is within the typical range of values of energy resolution obtained with micro-pattern gaseous detectors operating in CF_4 [70–72]. Furthermore, it can be seen that at a gain of 1000, the 5.9 keV peak is completely separated from the electronic noise which, in this detector, was rather high—around 2 keV.

The studies of gain in charge presented in this work were done in pure CF_4. The

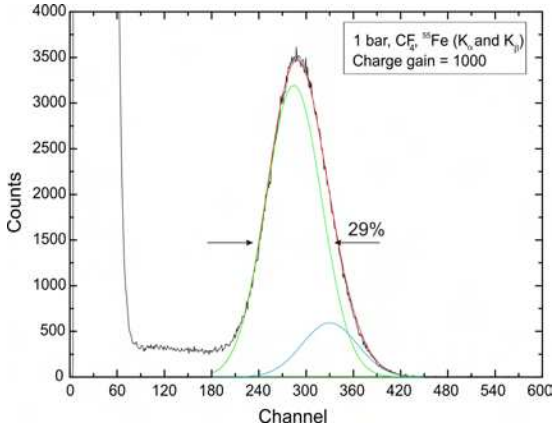

Figure 4.5: An energy distribution of the K_α and K_β X-rays from an ^{55}Fe radioactive source. The detector was operating at 1 bar, and with a gain in charge of 1000. The values are within the typical energy resolutions obtained with gaseous micropattern detectors.

addition of helium has a small effect in the gain, compared to the effect of increasing the partial pressure of CF_4, resulting in a shift of the gain curves to slightly higher biasing voltages. This will be discussed in section 4.4.

4.2 Imaging with tetrafluoromethane

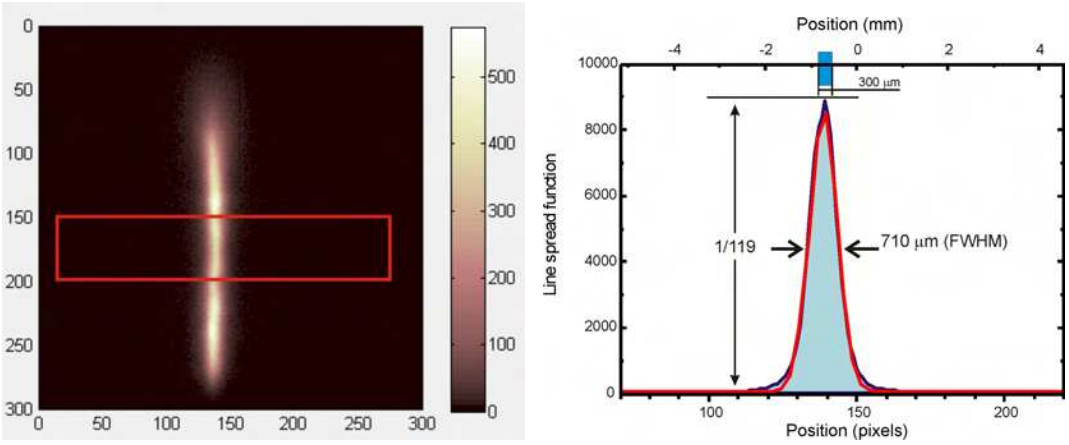

(a) (b)

Figure 4.6: (a) The image of a 300 µm slit. The red rectangle marks the area selected to calculate the *line spread function* in (b) The LSF of the slit in the x coordinate. The distribution has a width of 710 µm (FWHM). The contrast of 1/119 is lower than expected due to a noisy electronic channel.

To determine the performance of the MHSP when imaging in an atmosphere of tetrafluoromethane (CF_4), the technique of imaging a thin slit was used, as in the previous chapters. This time, a molybdenum X-ray tube was used. Its voltage and current were variable, within the rages of 0–50 kV and 0–1 mA. The tube was placed at a distance of 1 m from the detector window.

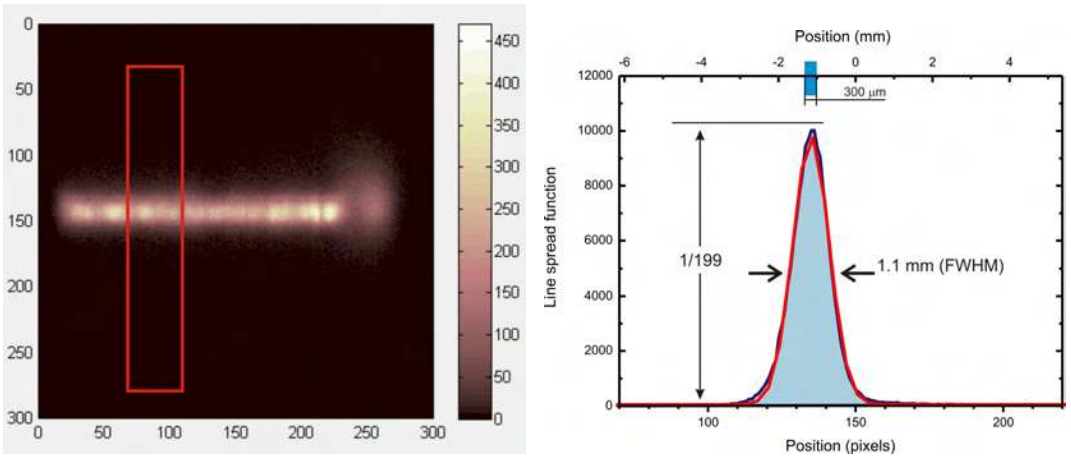

(a) (b)

Figure 4.7: (a) The 300 µm slit oriented horizontally. It is obvious that the image appears wider. (b) The LSF shows a width of 1.1 mm (FWHM) and contrast of 1/199.

Two lead plates with sharp edges were used to make the slit, using 300 µm thick stainless steel spacers to ensure the correct width of the slit. The system was calibrated using the stainless steel hexagonal grid as in last chapter. The image of fig. 4.6(a) is the slit, imaged with the detector filled with 1 bar of CF_4, biased with the following voltages: $\mathcal{E}_{\text{drift}} = 200\,\text{V/cm}$, $\Delta V_{\text{h}} = 730\,\text{V}$ and $\Delta V_{\text{s}} = 330\,\text{V}$. Taking into account that $\Delta V_{\text{h}} + \Delta V_{\text{s}} = 1060\,\text{V}$ and the graph of fig. 4.3, assuming that this MHSP has the same characteristics of all the others used over this work, the charge gain should be around $5 \times 10^4 \pm 10\,\%$. In the graph of fig. 4.3, ΔV_{s} was smaller than in the present case, but ΔV_{h} was higher. The gain is more sensitive to changes in ΔV_{h}, hence this assumption for the gas gain.

The contrast of the image with the background is 1/119, but this is due to the noise in one particular electronic channel, which leads to an increase of the background for this dimension. The width of the slit's LSF is 710 µm(FWHM), which shows that it is possible to have a position resolution of less than 1 mm with CF_4, at the pressure of 1 bar. If equation 2.8 is used to deconvolute the PSF from the slit in the LSF, a position resolution of 690 µm is obtained. It should be noticed that, for neutron detection, the electron avalanche corresponds to a deposited energy of 764 keV (whereas in this image the energy was spread around a maximum of intensity at 10 keV as described in the next subsection), having many more electrons, resulting in a much better signal-to-noise ratio and therefore much better position resolution. The same slit was then

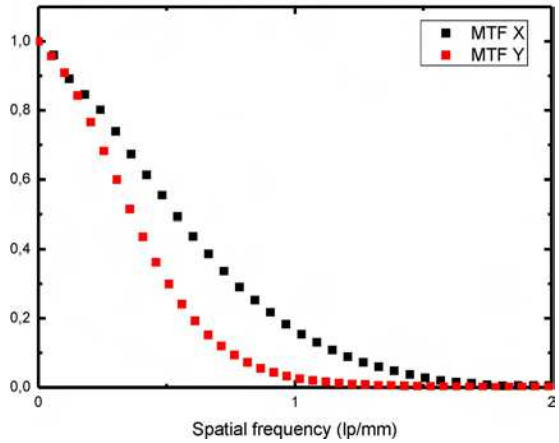

Figure 4.8: The Modulation Transfer Function derived from the images of the slit. The x-coordinate has a better response to spatial frequencies.

rotated by 90° and again imaged, as shown in fig. 4.7(a). It is obvious that the image of the slit is wider. As expected, the position resolution derived from the LSF was worse than for the x direction. The LSF has a width of 1.1 mm (FWHM), similar to that obtained with xenon and a contrast of $1/199$ with the background. This suggests that the value obtained for the position resolution in x might already be near the physical limit of CF_4 at 1 bar, due to the range of the photoelectrons.

To completely describe the detector in terms of its response to the spatial frequencies involved in the imaging process, the *modulation transfer function* was also derived from the distributions obtained with the slit. Figure 4.8 shows the MTF for both x- and y-coordinates. The values at 3 % of their amplitude are 1.5- and 1.0 $\mathrm{lp/mm}$ for x and y, respectively, consistent with what has been observed throughout this work.

4.2.1 Energy dependence of the position resolution

Figure 4.9(a) shows the energy spectrum of the Mo X-ray tube, as detected with the MHSP operating in CF_4 at the pressure of 1 bar. The red curve is the absorption of the X-rays in the detector volume as a function of their energy. The detector efficiency drops two orders of magnitude between 1 and 10 keV. That explains the shape of the energy spectrum obtained.

As for the studies made with the detector filed with xenon, the width of the slit was measured over several different energy ranges, marked with different colours in the graph. For each of these ranges, the width of the image of the slit was averaged over its length and plotted as shown in fig. 4.9(b). The error bars are the standard deviation of the values obtained for the width measured along the whole length of the slit. As expected, for the higher energies, the error bars are larger because there are

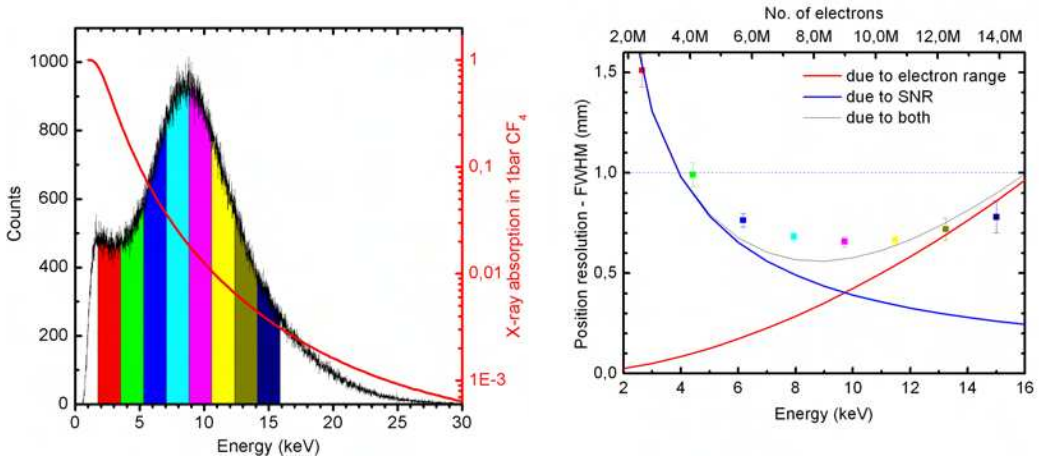

(a) (b)

Figure 4.9: (a) The energy distribution of the Mo X-ray tube as obtained with the detector. The red curve is the X-ray absorption of a 5 mm thick layer of CF_4 at 1 bar. The detector has an efficiency below 1 % for energies above 10 keV. (b) The position resolution measured using the energy regions marked in (a). The red curve is the range of electrons in CF_4 at 1 bar [73] and the blue is the resolution limit due to the SNR, for an electronic noise of around 1 keV.

fewer events. The red curve is the function [16]

$$\sigma_{CF_4} = k\frac{E^{1.75}}{\rho},$$

where σ_{CF_4} is the resolution limit, empirically estimated taking into account the data points, with $k = 280\,\mathrm{g/keV^{1.75}cm^2}$ and $\rho = 3.72\,\mathrm{g/l}$. The effect of the signal-to-noise ratio (blue curve) is dominant for low energies, but at higher energies, the effect of the photoelectron range becomes important and limits the position resolution. The value of k was chosen to fit the data, and is smaller than the determined for hydrocarbon gases (subsection 2.3.2 and references [14, 15, 74]). This suggests that, at the contrary of the hydrocarbon gases studied in the references, the position resolution limit is lower than the range of the photoelectrons. The ionisation is not evenly distributed over the photoelectron track, but is larger at the beginning, with the centroid of the charge closer to the interaction point. The behaviour of CF_4 is also approximately proportional to $E^{1.75}$, but the proportionality constant is smaller than the values presented in [15] for methane and ethane.

4.3 The standard GEM in tetrafluoromethane

During this work, some parallel measurements were made using a GEM, for comparison. The data obtained for the gain in charge proved to be useful because updated results for the gain in charge of single-GEMs operating in CF_4 were needed.

Over several years of work with the MHSP, a steep development in terms of performance and reliability was noticed. This was attributed on a first approach to a gain of experience when handling such sensitive devices, from the detector assembly phase to the polarisation and conditioning. However, the most important part was due to the increase of the manufacturing quality of the MHSPs. In fact, a visual inspection at the microscope of the first MHSPs manufactured, side-by-side with the newest stocks reveals that the amount of defects and imperfections has significantly dropped. As a consequence, much higher charge gains and energy resolutions over the whole surface can now be achieved.

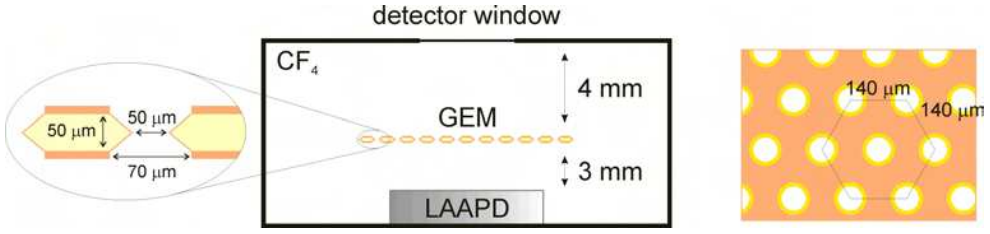

Figure 4.10: The detector setup used in this section. The GEM was 50 µm thick, with 50/70 µm holes in a hexagonal distribution with 140 µm long edges. The drift region was 4 mm deep. This detector was also equipped with a LAAPD for scintillation studies (not in the frame of this work).

If the performance of the MHSP presented in this work is to be compared with the performance of a GEM, data up to date should be used. The last results on the performance of single GEMs working in CF_4 atmosphere date back to the beginning of the decade. Since the MHSP manufacturing has undergone such a development, it is reasonable to think that today, the performance of a GEM should be much better than some years ago, and the argument that the charge gain of the MHSP is higher because it has two amplification stages should be carefully tested. With CF_4 the gains and the electric fields achieved can be so high that there is no guarantee that the field lines between the strips do not penetrate the holes, shaping the field in a different way. This section can be read as a sort of outlook, providing a glimpse on other possibilities for neutron imaging with GEMs. For these studies, another detector vessel was used and the MHSP was substituted by a 50 µm thick standard GEM with 50/70 µm holes distributed in a hexagonal array with edges 140 µm long, as shown in fig. 4.10. The drift region was set to 4 mm. The induction electrode was grounded, at a distance of 3 mm. It was, in fact, the shielding of LAAPD used to detect the scintillation light of CF_4. The X-rays from a ^{109}Cd radioactive source (silver X-rays: $K_\alpha = 22.1$ keV and $K_\beta = 24.9$ keV) were used to generate the primary cloud and the charge was collected directly from the bottom electrode of the GEM by a Canberra™

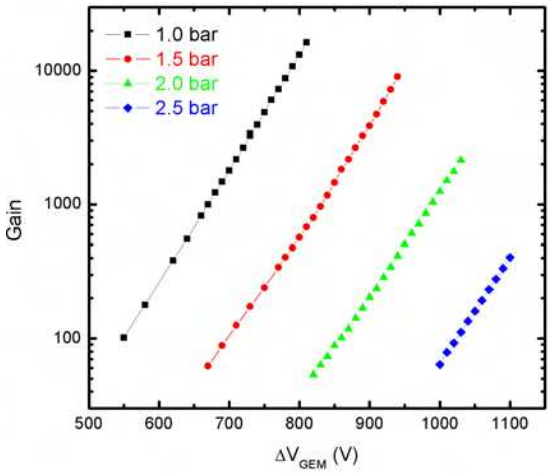

Figure 4.11: The gains obtained with a GEM operating in pure CF_4, at the pressures of 1.0, 1.5, 2.0 and 2.5 bar.

2006 charge preamplifier, with a charge sensitivity of 235 mV/Mion-pair. The shaping was made with a Tenelec™ TC243 amplifier with 4 µs peaking time. The gain in charge was determined with the help of a calibrated 2 pF capacitor and a precision BNC™ pulse generator. The gain curves as a function of the GEM voltages are depicted in

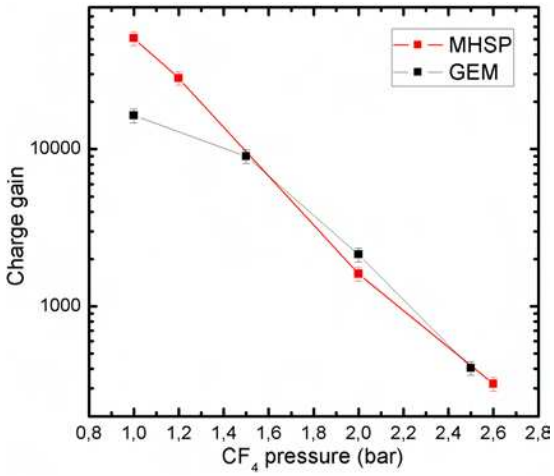

Figure 4.12: The maximum gain obtained as a function of the pressure, for the GEM and the MHSP. Although higher gains were obtained with the MHSP at 1 bar, given this distribution, it is reasonable to assume that both MPGDs have a similar behaviour.

fig. 4.11 for the pressure range of 1– to 2.5 bar. The pressure limit was imposed by the specifications of the LAAPD[1]. The GEM was not able to reach gains as high as

[1]Deep UV Series, Advanced Photonix Inc., Camarillo, CA. The detector described in this chapter

with the MHSP at 1 bar (the maximum gain was 16.3×10^3), but at 2.5 bar, the gain was 400. The maximum gain drops for high pressures, therefore, it is reasonable to estimate that the behaviour of the GEM would be similar to the MHSP at 2.6 bar.

While for a given biasing voltage, it is possible to extrapolate the gas gain by fitting equation 1.11 to the data, the estimation of the maximum gain achieved is more tricky, since many other important factors influence the physical limits of micropattern detectors. The presence of microscopic imperfections in the copper layer or even small dust particles might form sources of electrical discharges and limit the maximum voltage possible to apply to the detector.

As shown in fig. 4.12, if the maximum charge gain is plotted as a function of the pressure for the GEM and for the MHSP, the data are roughly equivalent for pressures above 1.5 bar. It is difficult to estimate the tendency for the pressures of 2.5- and 2.6 bar and the assumption that both micropattern detectors are equivalent seems to be the most reasonable.

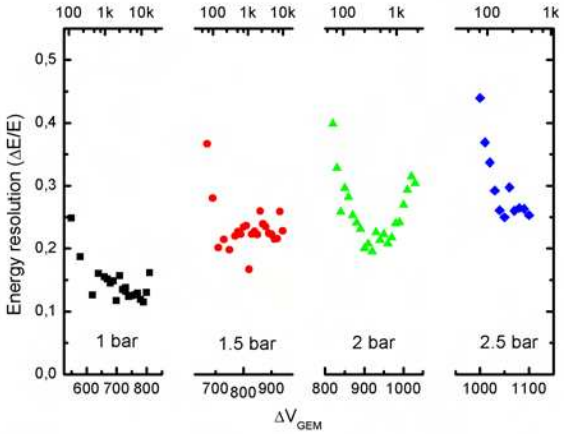

Figure 4.13: The energy resolution with a ^{109}Cd source ($K_\alpha = 22.1$ keV) for different pressures.

The distribution of the resolution as a function of the biasing voltage (or the gain) for the different pressures shows a small degradation as the pressure increases, due to the decrease in the gain. Energy resolutions of 12 % were achieved with the GEM operating at 1 bar, and for 2.5 bar, it was still possible to have energy resolutions below 30 %, for 22.1 keV.

was built prior to this thesis, for generic studies of charge gain ad scintillation yield. Therefore, the maximum pressure of the LAAPD was not a criterion for its purchase, the 2.5 bar limitation prevented made measurements at 2.6 bar would have the LAAPD damaged.

4.4 Discussion

The results in this chapter, were obtained operating the MHSP and the GEM in pure tetrafluoromethane (CF_4) at different pressures in the range of 1– to 2.6 bar. The gain in charge for this range of pressures was estimated.

The images obtained with the MHSP were measured with CF_4 at 1 bar, to demonstrate that the MHSP is actually able to achieve resolutions below 1 mm in this gas, being limited mostly by the range of the particle generating the charge cloud—in this case, the photoelectron; in the case of neutron detection, the proton. However, these results should be discussed within the frame of neutron detection to have some meaning.

One important aspect is how the detector will behave when a further partial pressure of 6 bar ^{3}He is added to the 2.6 bar CF_4. The mean free path of the electrons should be affected and this should affect the gain in charge. If a photon hits a ^{3}He atom or a CF_4 molecule, a photoelectron with an energy very close to the energy of the incident photon energy is removed. Several authors concluded that the electron-impact ionisation cross section (for elastic and inelastic collisions) of ^{3}He, as calculated through the Binary-Encounter-Bethe model (BEB) [73] (and references therein), is approximately 20 times smaller than that of CF_4 ($\sigma_{\mathrm{BEB}}\left(^3\mathrm{He}\right) = 0.019\,\text{Å}^2$ and $\sigma_{\mathrm{BEB}}\left(CF_4\right) = 0.396\,\text{Å}^2$). The mean free path of the electrons remains therefore almost unchanged with the addition of ^{3}He to CF_4. This minimal effect has been reported in works with several other gases [28,40,51,75], and means that the gain curves are slightly shifted towards higher voltages. The effect in position resolution results in a slight improvement, due to a decrease of around 14 % in the electron range.

If the products of the $\mathrm{n}\left(^3\mathrm{He},\mathrm{T}\right)\mathrm{p}$ reaction are considered, the position resolution is, as calculated before, 1 mm, limited by the gas mixture and not by the performance of the MHSP. The primary electron cloud is more than 70 times larger and the loss in gain is barely noticed. This high amount of deposited energy is also a feature to be taken into account in this discussion. The charge collected by the preamplifiers is given by:

$$Q = \frac{E_{\mathrm{x}}}{w} G_{\mathrm{x}} \cdot e,$$

where E_{x} is the X-ray energy, w is the w-value of the gas ($w_{CF_4} = 54\,\text{eV}$), G_{x} is the gain in charge and e is the charge of one electron.

If the charge collected does not change, it means that the SNR is also the same. Therefore, to calculate the gain needed to keep this SNR when detecting the nuclear reaction products, one simply must reverse the calculations:

$$G_{\mathrm{n}} = \frac{Q}{e} \cdot \frac{w_{CF_4}}{E_{\mathrm{n}}} \Leftrightarrow G_{\mathrm{n}} = \frac{E_{\mathrm{x}}}{E_{\mathrm{n}}} G_{\mathrm{x}},$$

where the subscript n denotes the nuclear reaction. To have a signal-to-noise ratio similar to that achieved with 5 keV at 1 bar as in fig. 4.9(b) (page 80), with a gain in charge of 50×10^3, a gain of only 327 is needed for the 764 keV deposited by the products of the $\mathrm{n}\left(^3\mathrm{He},\mathrm{T}\right)\mathrm{p}$ reaction. The results described in this chapter have shown

that this gain was achieved at 2.6 bar, the pressure needed for 1 mm intrinsic resolution. Figure 4.9(b) shows that with this SNR, the MHSP has a position resolution well below the proton range. If the SNR can be improved by reducing the electronic noise or with image processing and more sophisticated event discrimination, the detector can operate at even lower gain, because the primary electron cloud is much larger than the cloud generated by X-rays.

Finally, in section 4.3, it was shown that the manufacturing of MPGDs in general has improved over the past few years and that meanwhile the single-GEM has proved to be a very suitable alternative for neutron detection. At 1 bar, where the MPGDs are operated at moderate biasing voltages, the MHSP has a much higher gain than the GEM. However, as the pressure increases, the MHSP and the GEM must be able to stand higher biasing voltages and the tendency of achieving a higher gain with the MHSP starts to change. For pressures of CF_4 higher than 1 bar, it seems that the GEM is capable of achieving gains as high as the MHSP, despite the two multiplication stages of the latter. Other works report higher gains of the MHSP when compared with single-GEMs in gases such as argon or xenon [41]. Furthermore, the GEM seems to have a better energy resolution. This is consistent with the fact that, although the MHSP has a second multiplication stage which should give it a theoretical advantage, in practise, the process of manufacturing is more complex, making it less robust. With at least one additional step, it is more prone to imperfections and nonuniformities and more vulnerable to electrical discharges as the voltage increases. In fact, a large fraction of the problems faced with MHSPs have to do with defects in the strips and not in the holes. These defects decrease dramatically the maximum biasing voltage and consequently the gain achieved with the MHSP. The energy resolution is also affected, because if the strip thickness is not uniform, the charge gain is also not uniform along the surface of the detector.

Nevertheless, as mentioned more than once, the manufacturing process has undergone a very fast and consistent development and quality control made in the laboratories in Aveiro and Coimbra, has shown an improvement in every new patch of MHSPs, with lower leaking currents between strips and a higher reliability.

Chapter 5

Conclusions

In this work, an imaging detector based in a Micro-Hole & Strip Plate was developed for X-ray and neutron detection. The design of the standard MHSP was adapted to exploit its imaging capability. The anode strips were separated and interconnected with resistive strips and the GEM-side was structured also in separate strips interconnected with the resistive line to determine the second spatial coordinate. The position could be determined from the difference in amplitude of the signals collected at each edge of one resistive strip.

The performance of the imaging system was tested in xenon and tetrafluoromethane (CF_4) at 1 bar, with X-rays. The position resolution obtained with xenon was 380 µm and 1.2 mm for x and y, respectively. For CF_4, spatial resolutions of 700 µm and 1.1 mm were obtained. The results have a good agreement with what was expected, taking into account the signal-to-noise ratio and the range of the photoelectrons in the filling gas.

When using xenon, the position resolution obtained was used to distinguish small features in complex objects. The images presented in this work are raw data and have not undergone any kind of image processing. Nevertheless, it was possible to distinguish the skeleton of a common quail wing or enhance features in soft tissue, by choosing suitable energy ranges.

For neutron detection, helium-3 has to be added to CF_4. Helium-3 has a loosely bound proton and if a neutron is in its vicinity, a nuclear reaction occurs, releasing one triton and one proton in opposite directions. To achieve a position resolution of 1 mm, the proton range must be shortened by increasing the pressure of CF_4 to 2.6 bar. Taking into account the minimum signal-to-noise ratio that allows achieving a position resolution of 1 mm, it was noticed that a charge gain of 327 is needed at 2.6 bar. This gain has been achieved with the MHSP in these conditions, which allows concluding that the 2D-MHSP operating together with resistive strips is suitable for neutron imaging with sub-millimetric spacial resolution.

The possibility of recording each event together with its energy puts the MHSP in advantage when compared to other imaging systems. In neutron detection this acquires greater importance, since it is possible to discriminate events corresponding to tracks

lost to the walls of the detecting volume, or events due to gamma interactions, which tend to deteriorate the spatial resolution. Furthermore, the event information can be used for off-line image processing, taking advantage of the energy information.

A very important advantage of this detector is its cost. One single MHSP has a cost below 100 €, which makes it tremendously competitive against most of the radiation imaging applications. Even with the addition of readout electronics, the final price of one imaging detector can be several orders of magnitude lower than other imaging systems. It might give the MHSP an advantage even against systems with a better resolution, but a higher price.

5.1 Applications

The 2D-MHSP can be used in a high number of imaging applications. The immediate utility of such a detector as described in this work is the monitoring of neutron beams. With a spatial resolution below 1 mm, the analysis of the shape of the beam is simple. The PEARL and ROTAX beams of ISIS have been used to test a neutron beam monitor based on a Microstrip Gas Detector [76]. The sensitive area was $5.8 \times 6\,\mathrm{cm}^2$. The strips were connected in groups of four and each group was readout with an independent electronic channel. Spatial resolutions around 500 µm (1D) are claimed for this detector, proving that MPGDs are suitable detectors to be used in neutron beam monitoring. The MHSP would deliver 2D images with a resolution below 1 mm, using much simpler electronics.

Applications including X-ray imaging have been tested with this system. One of them is Imaging X-ray Fluorescence Spectroscopy. By irradiating a sample with different materials with an intense X-ray beam and collecting the fluorescence X-rays in the detector, after they have passed through a pinhole, it is possible to obtain an X-ray image of the different elements present in the sample. The pinhole assures that the X-ray hitting the detector in one position can only come from one place in the sample. Tests have been already made with samples containing iron, germanium and zirconium, providing 2D images of the different materials [77] and in the analysis of the depth of led penetration in ceramics [78].

Some studies in X-ray polarimetry have also been performed, using a carbon crystal to polarise X-rays. The position resolution of the detector described in this work allows distinguishing the preferred direction of photoelectron emission. This work is under development and the results already obtained are promising [79].

The use of the imaging MHSP in X-ray or neutron diffraction can also bring many advantages due to the possible energy discrimination, which avoids the use of X-ray monochromators or movement during the data acquisition. In summary, as an imaging detector, the 2D-MHSP has the possibility of being used in many imaging applications, including medical, such as scintigraphy, tomography or PET.

5.2 Future work

There is still plenty of room for development of the imaging capability of the MHSP. As referred in the discussion sections, the signal-to-noise ratio is a key factor in the performance of the detector. The most recent batches of imaging-MHSPs manufactured in CERN, had a much better quality and allowed achieving higher voltages, leading to higher gains and higher SNR. Due to this, higher resolutions are expected in the newest detectors. The improvement in the uniformity of the resistive strip is also notorious. During the writing of this thesis, some images acquired with a new detector, with a larger window, have shown a much better uniformity of the image. All this reflects that the MHSP is getting more reliable, with the accidents due to defects in the anode strips leading to sparks happening more rarely.

The development of a larger imaging-MHSP is also under development. The new large area imaging-MHSP will have an area of $5 \times 10\,\mathrm{cm}^2$. The noise problems due to the resistive strips might be a challenge, but a larger detector will definitely broaden even more the range of applications of this detector.

Besides the improvements in terms of hardware, there are still many possibilities to further improve the results of the MHSP with software image processing techniques. The process of building the images in this system is different from the conventional medical X-ray imaging systems. The difference is related to the energy resolving capability. In conventional systems, the image obtained is the integrated energy deposited in the detector. The photons with higher energy have a higher contribution to the image than the less energetic photons. In this system, each pixel is the integral of its energy spectrum and every event has the same contribution regardless of the energy of the photons originating it. The intensity $\tilde{I}$ of each pixel is given by:

$$\tilde{I} = \sum_{i}^{n} I_i \cdot w_i, \tag{5.1}$$

where I_i is the intensity of the photons with energy given by i. w_i is the weighting factor. In conventional, non-energy resolving systems, w_i is proportional to i and in the system described in this work, w_i is constant over i. This typically provides a better contrast, when compared to the energy integrating image formation. Since the information of the energy of each event is recorded, any choice of w_i can be tested to enhance the image. Some techniques of image improvement are under development, using energy weighting to enhance the contrast of an image. This technique enhances the contrast of the image between two different materials, making use of their transmittance as a function of the energy [80]:

$$w_i = \frac{T_i - T_i'}{T_i + T_i'}. \tag{5.2}$$

The technique has been applied to fig. 3.9(d), resulting in a contrast enhancement of 27 %. This example shows that there is plenty of room for enhancements in the field of image processing.

Bibliography

[1] W. C. Röntgen. Über eine neue art von strahlen. In *Aus den Sitzungsberichten der Würzburger Physik.-medic. Gesellschaft Würzburg*, pages 137–147, 1895. Translation into Portuguese: A. C. P. Carvalho, Sobre uma nova espécie de raios, Rev. Imagem, 27(4):287-293, 2005.

[2] A. Einstein. Über einen die erzeugung und verwandlung des lichtes betreffenden heuristischen gesichtspunkt. *Ann. Phys.*, 17:132–148, 1905. Translation into English: Concerning an Heuristic Point of View Toward the Emission and Transformation of Light, Am. J. Phys., 33 n. 5, 1965.

[3] R. E. Van Grieken ad A. A. Markowicz. *Handbook of X-ray Spectrometry — Methods and Techniques*, volume 14 of *Practical Spectroscopy series*. Marcel Dekker, Inc., 1993.

[4] H. Bethe. Zur Theorie des Durchgangs schneller Korpuskularstrahlen durch Materie. *Annalen der Physik*, 397:325–400, 1930.

[5] Glenn F. Knoll. *Radiation detection and measurement*. John Wiley and Sons, Inc., 3rd edition, 2000.

[6] Kenneth S. Krane. *Introductory Nuclear Physics*. John Wiley and Sons, Inc., 1987.

[7] D. Findlay. Introduction to ISIS accelerator and target. In *ISIS lectures*, chapter Second series. ISIS, Rutherford Appleton Laboratory, 2006. URL: http://www.isis.rl.ac.uk/accelerator/lectures/lectures_series2.htm.

[8] H. Geiger and W. Müller. Elektronenzählrohr zur Messung schwächster Aktivitäten. *Naturwissenschaften*, 16(31):617, 1928. doi:10.1007/BF01494093.

[9] W. Diethorn. NYO-6628, 1956 (as cited in: G. F. Knoll, Radiation Detection and Measurement).

[10] C. A. N. Conde and A. J. Policarpo. A Gas Proportional Scintillation Counter. *Nuclear Instruments & Methods*, 53(1):7–&, 1967.

[11] A. C. S. M. Bento C. A. N. Conde, J. M. F. dos Santos. New concepts for the design of large area gas proportional scintillation counters. *IEEE Trans. Nucl. Sci.*, 40:452–454, 1993.

[12] H. Natal da Luz, J. F. C. A. Veloso, J. M. F. dos Santos, C. A. N. Conde, R. M. C. Silva, Pan H.-R., Lin H.-A., and Li Z.-Y. A large area gas proportional scintillation counter for solar X-ray spectrometry with a balloon born experiment. *IEEE Trans. Nucl. Sci.*, 49:2488–2491, 2002.

[13] G. Charpak, R. Bouclier, T. Bressani, J. Favier, and C. Zupancic. Use of multiwire proportional counters to select and localize charged particles. *Nucl. Instr. Meth.*, 62(3):262, 1968.

[14] J. E. Bateman, M. W. Waters, and R. E. Jones. Spatial resolution in a xenon filled MWPC X-ray imaging detector — a computing physics approach. *Nucl. Instr. Meth.*, 135:235–249, 1976.

[15] G. C. Smith, J. Fischer, and V. Radeka. Photoelectron range limitations to the spatial-resolution for X-rays in gas proportional chambers. *IEEE Trans. Nucl. Sci.*, 31(1):111–115, 1984.

[16] J. Fischer, V. Radeka, and G. C. Smith. X-ray position detection in the region of 6 μm rms with wire proportional chambers. *Nucl. Instr. Meth. A*, 252(2-3):239–245, 1986.

[17] A. F. Barbosa, G. P. Guedes, and H. P. Lima Jr. Recent results on a simple scheme for 2D localization of particles in a wire chamber. *Nucl. Instr. Meth. A*, 477:41–47, 2002.

[18] J. E. Bateman. A general parametric model for the gain of gas avalanche counters with particular attention to non-cylindrical geometries. *Physics Reports*, 375:411–443, 2003.

[19] A. Oed. Position-sensitive detector with microstrip anode for electron multiplication with gases. *Nucl. Instr. Meth. A*, 263:351–359, 1988.

[20] J. F. C. A. Veloso, J. A. M. Lopes, J. M. F. dos Santos, and C. A. N. Conde. A microstrip gas chamber as a VUV photosensor for a xenon gas proportional scintillation counter. *Nuclear Science, IEEE Transactions on*, 43(3):1232–1236, Jun 1996.

[21] J. F. C. A. Veloso, J. M. F. dos Santos, and C. A. N. Conde. Gas proportional scintilation counter with a CsI-covered microstrip plate UV photosensor for high-resolution X-ray spectrometry. *Nucl. Instr. Meth. A*, 457:253–261, 2001.

[22] J. E. Bateman, J. F. Connolly, A. B. Lodge, R. Stephenson, R. Mutikainen, I. Suni, and J. Morse. A gas microstrip detector for X-ray imaging with readout of the anode by resistive division. *Nucl. Instr. Meth. A*, 477:29–36, 2002.

[23] N. Vellettaz, J. E. Assaf, and A. Oed. Two-dimensional gaseous microstrip detector for thermal neutrons. *Nucl. Instr. Meth. A*, 392:73–79, 1997.

[24] F. Ortuño-Prados and C. Budtz-Jørgensen. The electron-conducting glass SCHOTT S8900 as substrata for microstrip gas chamber. *Nucl. Instr. Meth. A*, 364(2):287 – 289, 1995.

[25] Y. Giomataris, Ph. Rebourgeard, J. P. Robert, and G. Charpak. MICROMEGAS: a high-granularity position-sensitive gaseous detector for high particle-flux environments. *Nucl. Instr. Meth. A*, 376(1):29 – 35, 1996.

[26] J. P. Cussonneau, M. Labalme, P. Lautridou, L. Luquin, V. Metivier, A. Rahmani, and T. Reposeur. 2D localization using resistive strips associated to the micromegas structure. *Nucl. Instr. Meth. A*, 492:26–34, 2002.

[27] F. Sauli. GEM: a new concept for electron amplification in gas detectors. *Nucl. Instr. Meth. A*, 386:531–534, 1997.

[28] A. Bondar, A. Buzulutskov, and L. Shekhtman. High pressure operation of the triple-GEM detector in pure Ne, Ar and Xe. *Nucl. Instr. Meth. A*, 481(1-3):200 – 203, 2002.

[29] A. Orthen, H. Wagner, H. J. Besch, S. Martoiu, R. H. Menk, A. H. Walenta, and U. Werthenbach. Gas gain and signal length measurements with a triple-GEM at different pressures of Ar-, Kr- and Xe-based gas mixtures. *Nucl. Instr. Meth. A*, 512(3):476 – 487, 2003.

[30] A. Buzulutskov, A. Breskin, R. Chechik, G. Garty, F. Sauli, and L. Shekhtman. The GEM photomultiplier operated with noble gas mixtures. *Nucl. Instr. Meth. A*, 443(1):164 – 180, 2000.

[31] A. Breskin, A. Buzulutskov, and R. Chechik. GEM photomultiplier operation in CF_4. *Nucl. Instr. Meth. A*, 483:670–675, 2002.

[32] A. Bressan, M. Hoch, P. Pagano, L. Ropelewski, F. Sauli, S. Biagi, A. Buzulutskov, M. Gruwé, G. De Lentdecker, D. Moermann, and A. Sharma. High rate behavior and discharge limits in micro-pattern detectors. *Nucl. Instr. Meth. A*, 424:321–342, 1999.

[33] S. Bachmann, S. Kappler, B. Ketzer, Th. Müller, L. Ropelewski, F. Sauli, and E. Schulte. High rate X-ray imaging using multi-GEM detectors with a novel readout design. *Nucl. Instr. Meth. A*, 478:104–108, 2002.

[34] G. P. Guedes, A. Breskin, R. Chechik, D. Vartsky, D. Bar, A. F. Barbosa, and P. R. B. Marinho. Two-dimensional GEM imaging detector with delay-line readout. *Nucl. Instr. Meth. A*, 513:473–483, 2003.

[35] R. Chechik, A. Breskin, C. Shalem, and D. Mörmann. Thick GEM-like hole multipliers: properties and possible applications. *Nucl. Instr. Meth. A*, 535(1-2):303 – 308, 2004. Proceedings of the 10th International Vienna Conference on Instrumentation.

[36] M. Cortesi, R. Alon, R. Chechik, A. Breskin, D. Vartsky, and V. Dangendorf. Investigations of a THGEM-based imaging detector. *J. Inst.*, 2(P09002), 2007.

[37] J. A. Mir, R. Stephenson, N. J. Rhodes, E. M. Schooneveld, J. F. C. A. Veloso, and J. M. F. Dos Santos. Short induction gap gas electron multiplier (GEM) for X-ray spectroscopy. *Nucl. Instr. Meth. A*, 573(1-2):179 – 182, 2007. Proceedings of the 7th International Conference on Position-Sensitive Detectors - PSD-7, 7th International Conference on Position-Sensitive Detectors.

[38] J. A. Mir, R. Stephenson, N. J. Rhodes, E. M. Schooneveld, H. Natal da Luz, J. F. C. A. Veloso, J. M. F. Dos Santos, and C. D. R. Azevedo. Further studies on the gain properties of a gas electron multiplier with a micro-induction gap amplifying structure (GEM-MIGAS) aimed at low-energy X-ray detection. *Nucl. Instr. Meth. A*, 580(3):1372 – 1377, 2007.

[39] J. F. C. A. Veloso, J. M. F. dos Santos, and C. A. N. Conde. A proposed new microstructure for gas radiation detectors: The microhole and strip plate. *Rev. Sci. Inst*, 71(6):2371–2376, 2000.

[40] J. F. C. A. Veloso, F. Amaro, J. M. F. dos Santos, J. A. Mir, G. E. Derbyshire, R. Stephenson, N. J. Rhodes, and E. M. schooneveld. Application of the micro hole and strip plate detector for neutron detection. *IEEE - Trans. Nucl. Sci.*, 51(5):2104–2109, 2004.

[41] F. D. Amaro, A. S. Conceição, J. F. C. A. Veloso, L. C. C. Coelho, L. M. P. Fernandes, L. F. R. Ferreira, J. A. M. Lopes, and J. M. F. dos Santos. Operation of a single-GEM in noble gases at high pressures. *Nucl. Instr. Meth. A*, 579:62–66, 2007.

[42] J. F. C. A. Veloso, C. C. Caldas, C. A. B. Oliveira, C. D. R. Azevedo, J. M. F. dos Santos, A. Breskin, and R. Chechik. High-rate operation of the micro-hole and strip plate gas detector. *Nucl. Instr. Meth. A*, 580(1):362 – 365, 2007. Proceedings of the 10^{th} International Symposium on Radiation Physics - ISRP 10.

[43] R. Chechik, A. Breskin, G. P. Guedes, D. Mörmann, J. M. Maia, V. Dangendorf, D. Vartsky, J. M. F. dos Santos, and J. F. C. A. Veloso. Recent investigations of cascaded GEM and MHSP detectors. *IEEE Trans. Nucl. Sci.*, 51(5), 2004.

[44] E. D. C. Freitas, J. F. C. A. Veloso, A. Breskin, R. Chechik, F. D. Amaro, L. F. Requicha Ferreira, J. M. Maia, and J. M. F. dos Santos. Micro-hole and strip plate-based photosensor. *Nucl. Instr. Meth. A*, 580(1):214 – 217, 2007. Proceedings of the 10^{th} International Symposium on Radiation Physics - ISRP 10.

[45] J. F. C. A. Veloso, F. D. Amaro, C. D. R. Azevedo, J. M. F. dos Santos, A. Breskin, A. Lyashenko, and R. Chechik. PACEM: a new concept for high avalanche-ion blocking. *Nucl. Instr. Meth. A*, 581(1-2):261–264, OCT 21 2007. 11th International Vienna Conference on Instrumentation, Vienna, Austria, 2007.

[46] J. M. Maia, D. Mörmann, A. Breskin, R. Chechik, J. F. C. A. Veloso, and J. M. F. dos Santos. 2-D imaging with cascaded GEM/MHSP multipliers. *J. Inst.*, 2(P09008), 2007.

[47] A. Bressan, R. De Oliveira, A. Gandi, J. C. Labbé, L. Ropelewski, F. Sauli, D. Mörmann, T. Müller, and H. J. Simonis. Two-dimensional readout of GEM detectors. *Nucl. Instr. Meth. A*, 425:254–261, 1999.

[48] H. Tanaka, T. Nakamura, H. Yamagishi, K. Soyama, K. Aizawa, A. Ochi, and T. Tanimori. Development of two-dimensional micro-strip gas detector with individual readouts for neutron scattering experiments. *IEEE - Trans. Nucl. Sci.*, 2006.

[49] H. O. Anger, C. Martin, P. Jelinsky, M. Lampton, and R. F. Malina. Wedge-and-strip anodes for centroid-finding position-sensitive photon and particle detectors. *Rev. Sci. Instrum.*, 52:1067, 1981.

[50] F. Sauli, T. Meinschad, L. Musa, and L. Ropelewski. Photon detection and localization with GEM. In *IEEE Nuclear Science Symposium*, October 2004.

[51] F. A. F. Fraga, L. M. S. Margato, S. T. G. Fetal, M. M. F. R. Fraga, R. Ferreira Marques, A. J. P. L Policarpo, B. Guerard, A. Oed, G. Manzini, and T. van Vuure. CCD readout of GEM-based neutron detectors. *Nucl. Instr. Meth. A*, 478:357–361, 2002.

[52] V. N. Bychkov, G. D. Kekelidze, E. A. Novikov, V. D. Peshekhonov, M. D. Shafranov, and V. E. Zhiltsov. Cathode readout with stripped resistive drift tubes. *Nucl. Instr. Meth. A*, 367:276–279, 1995.

[53] A. Sarvestani, H. J. Besch, M. Junk, N. Pavel, N. Sauer, R. Stiehler, A. H. Walenta, and R. H. Menk. Gas amplifying hole structures with resistive position encoding: A new concept for a high rate imaging pixel detector. *Nucl. Instr. Meth. A*, 419:444–451, 1998.

[54] M. S. Dixit, J. Dubeau, J.-P. Martin, and K. Sachs. Position sensing from charge dispersion in micro-pattern gas detectors with a resistive anode. *Nucl. Instr. Meth. A*, 419:452–459, 2004.

[55] H. Natal da Luz, J.F.C.A. Veloso, F. Amaro, L.F. Requicha Ferreira, J.M.F. dos Santos, A Breskin, and R. Chechik. MHSP operation in pure xenon. *Nucl. Instr. Met. A*, 552:259–262, 2005.

[56] F. P. Santos, T. H. V. T. Dias, A. D. Stauffer, and C. A. N. Conde. Variation of energy linearity and w-value in gaseous xenon radiation detectors for x-rays in the 0.1 to 25 keV energy range: a Monte Carlo simulation study. *Nucl. Instr. Meth. A*, 307:357–352, 1991.

[57] T. H. V. T. Dias and F. P. Santos ad C. A. N. Conde. The primary electron cloud in xenon for X-rays in the 0.1 to 10 keV range. *Nucl. Instr. Meth. A*, 310:137–139, 1991.

[58] M. Li, M. S. Dixit, and P. C. Johns. Photon-counting digital radiography using high-pressure xenon filled detectors. *Nucl. Instr. Meth. A*, 471:215–221, 2001.

[59] Steven W. Smith. *The Scientist and Engineer's Guide to Digital Signal Processing.* California Technical Publishing, 2006. available at http://www.dspguide.com/.

[60] J. T. Bushberg, J. A. Seibert, Jr. E. M. Leidholdt, and J. M. Boone. *The essential Physics of medical imaging.* Lippincott Williams & Wilkins, 2002.

[61] W. R. Hendee and E. R. Ritenour. *Medical Imaging Physics.* Wiley-Liss, Inc., fourth edition edition, 2002.

[62] H. Klein, H. Brede, and B. R. L. Siebert. Energy and angle straggling effects in a D(d,n)^{3}He neutron source using a gas target. *Nucl. Instr. Meth.*, 193:635–644, 1982.

[63] Analog Devices, Inc., One Technology Way, P.O. Box 9106, Norwood, MA 02062-9106, U.S.A. *AD734, 10 MHz, 4-Quadrant Multiplier/Divider, product data sheet*, 1999.

[64] C.A.E.N., Via Vetraia, 11, 55049 - Viareggio (LU) - Italy. *Mod. N1728A/N1728B 4 Ch. Flash ADC, Revision n. 5*, October 2007.

[65] M. Richer and C. Santos. *TNT2 Digital Pulse Processor Functionalities & TUC control software.* Centre National de la Recherche Scientifique, Institut Pluridisciplinaire Hubert Curien – Institut National de Physique Nucléaire et de Physique des Particules, Strasbourgh, July 2007.

[66] V. T. Jordanov and G. F. Knoll. Digital synthesis of pulse shapes in real time for high resolution radiation spectroscopy. *Nucl. Instr. Meth. A*, 345(2):337 – 345, 1994.

[67] V. T. Jordanov, G. F. Knoll, A. C. Huber, and J. A. Pantazis. Digital techniques for real-time pulse shaping in radiation measurements. *Nucl. Instr. Meth. A*, 353(1-3):261 – 264, 1994.

[68] B. L. Henke, E. M. Gullikson, and J.C. Davis. X-ray interactions: photoabsorption, scattering, transmission, and reflection at E=50-30000 eV, Z=1-92. *Atomic Data and Nuclear Data Tables*, 54(2):181–342, 1993.

[69] J. F. Ziegler and J. P. Biersack. SRIM — The stopping and range of ions in matter. URL: http://www.srim.org, 2003.

[70] P. Jeanneret, J. Busto, J.-L. Vuilleumier, A. Geiser, V. Zacek, H. Keppner, and R. de Oliveira. Performance of a new micromegas detector, with woven wire mesh, in CF_4. *Nucl. Instr. Met. A*, 500:133–143, 2003.

[71] A. Kozlov, I. Ravinovich, L. Shekhtman, Z. Fraenkel, M. Inuzuka, and I. Tserruya. Development of a triple GEM UV-photon detector operated in pure CF_4 for the PHENIX experiment. *Nucl. Instr. Meth. A*, 524:345–354, 2004.

[72] L. M. S. Margato, F. A. F. Fraga, S. T. G. Fetal, M. M. F. R. Fraga, R. Ferreira Marques, A. J. P. L Policarpo, B. Guerard, and G. Manzin. Time analysis of the light pulses on gaseous active scintillators using GEMs with He/CF_4. *Nucl. Instr. Meth. A*, 504:374–378, 2003.

[73] Y.-K. Kim, K. K. Irikura, M. E. Rudd, M. A. Ali, P. M. Stone, J. Chang, J. S. Coursey, R. A. Dragoset, A. R. Kishore, K. J. Olsen, A. M. Sansonetti, G. G. Wiersma, D. S. Zucker, and M. A. Zucker. Electron-impact ionization cross-sections. URL: http://physics.nist.gov/PhysRefData/Ionization/, 1997. last update: 2005.

[74] L. Katz and A. S. Penfold. Range-energy relations for electrons and the determination of beta-ray end-point energies by absorption. *Rev. Mod. Phys.*, 24(1):28–44, Jan 1952.

[75] P. Kreuger, E. van Eijk, F. A. F. Fraga, M. M. Fraga, S. T. G. Fetal, R. W. Hollander, L. M. S. Margato, and T. L. van Vuure. Performance of high pressure Xe/TMA in GEMs for neutron and X-ray detection. In *Conf. Rec. IEEE Nucl. Sci. Symp.*, San Diego, CA, Nov. 4-10 2001.

[76] J. E. Bateman, J. F. Connolly, G. E. Derbyshire, D. M. Duxbury, J. Lipp, J. A. Mir, J. E. Simmons, E. J. Spill, and R. Stephenson. Studies of the gain properties of gas microstrip detectors relevant to their application as X-ray and electron detectors. *IEEE - Trans. Nucl. Sci.*, 49(4):1644–1650, 2002.

[77] J. F. C. A. Veloso, A. L. M. Silva, C. Oliveira, A. L. Gouvêa, H. Natal da Luz, and J.M.F. dos Santos. X-ray fluorescence imaging based on a micropattern gas detector. *Spectrochimica Acta B*, 2008. submitted.

[78] A. L. M. Silva, J. F. C. A. Veloso, C. A. B. Oliveira, A. L. Gouvêa, J. M. F. dos Santos, and M. L. Carvalho. Edxf imaging of pb depth penetration in glazed ceramics using a micropattern gas detector. *Anal. Bioanal. Chem.*, 2009. submitted.

[79] G. S. Botte, L. P. M. M. Carita, P. J. B. M. Rachinhas, T. H. V. T. Dias, R. M. Curado da Silva, F. P. Santos, J. F. C. A. Veloso, A. L. Gouvêa, L. M. N. Távora, C. A. N. Conde, and A.D. Stauffer. X-ray polarimetry in xenon gas filled detectors. 2009. MPGD2009; Crete, Greece.

[80] J. Giersch. Medical quantum X-ray imaging with 2D detectors. *NUCL. INSTR. METH. A.*, 551(1):125–138, OCT 1 2005. Symposium on Applications of Linear and Area Detectors for X-Ray and Neutron Diffraction and Spectroscopy held at the E-MRS Fall Meeting, Warsaw, POLAND, SEP 06-10, 2004.